



*Scuola Dottorale di Ingegneria
Sezione di Ingegneria dell'Elettronica Biomedica,
dell'Elettromagnetismo e delle Telecomunicazioni*

Design and Implementation of Metamaterial- Inspired Transmissive and Radiating Microwave Components

*Progetto e Realizzazione di Componenti Trasmissivi
e Radiativi a Microonde Ispirati ai Metamateriali*

Mirko Barbuto
(XXVI Ciclo della formazione Dottorale)

Docente-guida

Prof. Alessandro Toscano

This page is intentionally left blank.

Abstract

In this thesis, we present the design and the implementation of several metamaterial-inspired transmissive and radiating microwave components, which can be easily integrated in practically realizable systems.

First, we analyze the use of non-Foster active circuits to obtain a widening of the operating bandwidth of devices based on metamaterials (MTMs). In particular, the more suitable loading circuit is analytically determined and it is used to dramatically increase the operating bandwidth of an electrically small antenna consisting of a monopole loaded with a single split-ring resonator (SRR). The non-Foster circuit is designed by using only real components and the stability of the entire system is properly evaluated.

Then, we present some radiating elements based on the use of MTM-inspired resonant inclusions. As a first example, we propose a multi-functional antenna consisting of a printed monopole and two SRRs. Next, we design a compact antenna for Wi-Fi application consisting of two orthogonal parasitic meandered monopoles and a driven bow-tie.

Third, we propose a new class of horn antennas with integrated MTM-inspired filtering modules. In particular, we present some horn antennas that, depending on the used resonant inclusion, show a band-pass or band-stop filtering behavior.

Afterward, we focus our attention on non-radiative elements. In particular, by using complementary electrically small resonators, we design some compact microwave components (i.e. waveguide transition, power dividers, orthomode transducer) that, at the same time, show also a band-pass filtering behavior. Moreover, we design a novel and low-cost MTM-inspired absorber operating in X-band.

Finally, we explore the possibility to generate an electromagnetic field with a non-zero orbital angular momentum (OAM) using a single patch antenna. In particular, we report an analytical study of a circular patch antenna in order to show that a circular polarized TM_{nm} mode generates an OAM of order $n-1$. Then, we design an elliptical patch antenna that radiates a circular polarized electromagnetic field with OAM of the first order.

This page is intentionally left blank.

Acknowledgements

The completion of my dissertation has been a long journey in which many people have scientifically and humanly contributed. In the next few lines, I will try to thank all the people who supported me, without whose help I could not have made this journey.

I want to express my deeply-felt thanks to my supervisor, Prof. Alessandro Toscano, Head of the Electromagnetic Diagnostic Laboratory, for his warm encouragement and thoughtful guidance during my research activities. I sincerely thank also Prof. Filiberto Bilotti, Head of the Antennas & Special Materials Research Laboratory, who, starting from my B.S. degree, has always tried to bring me on the frontier of metamaterials science. They deserve my heartfelt gratitude for giving me the opportunity to enter the world of higher education and research, and for their valuable advice, constructive criticism and extensive discussions around my work.

My gratitude is also extended to all members of the Department of Engineering at “Roma Tre” University, for the excellent and pleasant working environment. I express my special thanks to my friends and colleagues Dr. Claudia Guattari, Dr. Alessio Monti and Dr. Davide Ramaccia, with whom I have enjoyed many useful and entertaining moments.

I would like to thank Elettronica S.p.A for the use of their near-field measurement system and for support in measurements. I am especially grateful to Dr. Fabrizio Trotta for useful discussions and for his contribution to the realization and characterization of some prototypes.

Last but not least, I want to reserve a special word of gratitude to my family, girlfriend Laura, friends and my fabulous nephews: Alessio, Ginevra, Valerio e Veronica, who have brought great joy to my life. They deserve thanks for their love and a huge variety of other reasons.

Mirko Barbuto

“Roma Tre” University

April 2015

This page is intentionally left blank.

Table of Contents

ESTESO SOMMARIO	1
INTRODUCTION	11
NON-FOSTER ACTIVELY LOADED SRR AND APPLICATION IN METAMATERIAL-INSPIRED COMPONENTS	21
1.1 ANALYTICAL DETERMINATION OF THE IDEAL LOAD	23
1.2 BROADBAND ACTIVE SRR: DESIGN PRINCIPLES	25
1.3 BROADBAND SRR-BASED MONOPOLE ANTENNA	29
1.4 IMPLEMENTATION ISSUES.....	31
1.5 STABILITY ISSUES.....	37
1.6 SUMMARY	42
1.7 REFERENCES.....	42
COMPACT AND MULTI-FUNCTIONAL ANTENNAS BASED ON MTM-INSPIRED STRUCTURES	45
2.1 MULTI-FUNCTIONAL SRR-LOADED PRINTED MONOPOLE ANTENNA.....	46
2.1.1 <i>Introduction</i>	46
2.1.2 <i>Design of the Proposed Structure</i>	47
2.1.3 <i>Numerical Results</i>	50
2.2 DESIGN OF A COMPACT ANTENNA BY USING ORTHOGONAL PARASITIC MEANDERED MONOPOLES	55
2.2.1 <i>Introduction</i>	55
2.2.2 <i>Antenna Design with Equal Meandered Monopoles</i>	56
2.2.3 <i>Antenna Design with Slightly Different Meandered Monopoles</i>	59
2.3 SUMMARY	63
2.4 REFERENCES.....	64
HORN ANTENNAS WITH INTEGRATED MTM-INSPIRED FILTERING MODULES	67
3.1 LINEAR-TO-CIRCULAR POLARIZATION TRANSFORMER	68
3.1.1 <i>Design of the Linear-To-Circular Polarization Transformer</i>	69
3.1.2 <i>Design of the Self-Filtering Circularly Polarized Horn Antenna</i>	74
3.2 A COMBINED BANDPASS FILTER AND POLARIZATION TRANSFORMER FOR HORN ANTENNAS	78
3.2.1 <i>Design of a planar Linear-To-Circular Polarization Transformer</i>	78

3.2.2	<i>Design of the Self-Filtering Circularly Polarized Horn Antenna</i>	82
3.2.3	<i>Experimental Realization and Measurements</i>	85
3.3	HORN ANTENNAS WITH INTEGRATED NOTCH FILTERS	86
3.3.1	<i>Design of a Horn Filtenna with a Single-Band-Stop Characteristic</i>	87
3.3.2	<i>Design of a Horn Filtenna with a Dual-Band-Stop Characteristic</i>	92
3.3.3	<i>Experimental Realization and Measurements</i>	94
3.4	SUMMARY	96
3.5	REFERENCES.....	98
NOVEL MTM-INSPIRED MICROWAVE COMPONENTS.....		100
4.1	NOVEL WAVEGUIDE COMPONENTS BASED ON COMPLEMENTARY ELECTRICALLY SMALL RESONATORS	101
4.1.1	<i>Design of a Rectangular-To-Circular Waveguide Transition</i>	102
4.1.2	<i>Design of Power Dividers</i>	106
4.1.3	<i>Design of an Orthomode Transducer</i>	109
4.2	LOW-COST AND BROADBAND MTM-INSPIRED ABSORBER WITHOUT A METALLIC BACKING 111	
4.2.1	<i>Design of the Metasurface</i>	112
4.2.2	<i>Design of the Resistive Sheet</i>	113
4.2.3	<i>Implementation of the Absorber</i>	118
4.2.4	<i>Experimental Realization and Measurements</i>	119
4.3	SUMMARY	121
4.4	REFERENCES.....	122
CIRCULAR POLARIZED PATCH ANTENNA GENERATING ORBITAL ANGULAR MOMENTUM.....		125
5.1	ANALYTICAL STUDY	126
5.2	VALIDATION THROUGH FULL-WAVE NUMERICAL SIMULATIONS.....	131
5.3	EXPERIMENTAL REALIZATION AND MEASUREMENTS	134
5.4	SUMMARY	135
5.5	REFERENCES.....	136
PUBLICATIONS.....		138
BIOGRAPHICAL NOTE		142

List of Figures

Fig. 1: (a) Geometry of a SRR loaded with an arbitrary impedance Z_L and (b) its lumped element equivalent circuit representation.	24
Fig. 2: Magnitude of the S_{11} parameter of the unloaded SRR case (solid line), of the SRR loaded with a LC tank circuit (dashed line), and of the SRR loaded with a LC tank circuit in series with an inductance (dot-dashed line).	26
Fig. 3: Magnitude of the S_{11} parameter of a waveguide with a SRR loaded with different test capacitances (values in the range -0.05-0.05 pF).	27
Fig. 4: Reactance of the loading capacitance as a function of the corresponding resonant frequency (triangular symbols), reactance of the LC tank non-Foster circuit (values in (5) have been used) (dashed line), and non-Foster reactance of a LC tank circuit in series with an inductor (values in (5) have been used) (solid line).	28
Fig. 5: Geometrical sketch of the SRR-based antenna proposed in [23]. Antenna dimensions in cm: $h = 3.00$, $h_1 = 31.60$, $h_2 = 29.64$, $d_1 = 1.14$, $d_2 = 1.90$. SRR dimensions in cm: $w = 3.42$, $R = 13.70$, $g = 0.76$, $s = 0.76$. Slab (FR-4): $\epsilon_r = 3.5$, $\tan\delta = 0.025$, thickness: 6.08 mm.	30
Fig. 6: Magnitude of the S_{11} parameter of the unloaded (dashed line) and loaded (solid line) antenna.	30
Fig. 7: SRR-based monopole antenna loaded with a parallel connection of two NIC circuits.	33
Fig. 8: Magnitude of the S_{11} parameter of the unloaded (solid line), ideally loaded (dashed line), NIC loaded (dotted line), and real NIC loaded (dot-dashed line) antenna.	34
Fig. 9: Input impedance of the unloaded and real NIC loaded antennas in real (solid and dotted line, respectively) and imaginary (dashed and dot-dashed line, respectively) part.	36
Fig. 10: Directivity patterns of the real NIC loaded antenna in the E-plane at 100 MHz (solid line), 96.1 MHz (dashed line) and 106.1 MHz (dot-dashed line).	36

Fig. 11: Directivity patterns of the real NIC loaded antenna in the H-plane at 100 MHz (solid line), 96.1 MHz (dashed line) and 106.1 MHz (dot-dashed line).....	37
Fig. 12: Equivalent model of the ideally loaded SRR.....	38
Fig. 13: Time-domain behavior of the current for the case of the unloaded antenna (thick black line) and for the case of an ideal 50 Ohm load (thin red line).	41
Fig. 14: Time-domain behavior of the current for the case of the loaded antenna (thick black line) and for the case of an ideal 50 Ohm load (thin red line).....	41
Fig. 15: Geometrical sketch of the single-SRR loaded printed monopole. Antenna dimensions are in mm: $W_g = 30$, $L_g = 15$, $L_m = 12$, $W_m = 5$, $L_{SRR} = 10$, $g = 0.2$, $s = 0.2$. Slab material: FR-4 ($\epsilon_r = 4.4$, $\tan \delta = 0.0085$). Slab thickness: 1.59 mm. Separation between monopole and SRR: 0.2 mm.....	47
Fig. 16: Magnitude of the scattering parameter S_{11} of the antenna reported in Fig. 1 and of a standard printed monopole antenna with the same dimensions.	48
Fig. 17: 3D directivity pattern of the single-SRR loaded printed monopole at the resonant frequency of the SRR 1.752 GHz.....	49
Fig. 18: Geometrical sketch of the multi-functional two-SRR loaded printed monopole. The numbered markers represent the switches placed in the gaps.	50
Fig. 19: Magnitude of the S_{11} parameter of the two-SRR loaded printed monopole for the eight switch status reported in Table I.	51
Fig. 20: Perspective view of the proposed antenna. The ground side is 10 cm.	56
Fig. 21: Front view (a) and back view (b) of the proposed antenna with equal meandered monopoles. Antenna dimensions are: $R_{BT} = 4.9$ mm, $H_m = 4.5$ mm, $g_m = 0.3$ mm, $w_m = 0.48$ mm, $L = 3$ mm.	57
Fig. 22: Reflection coefficient amplitude of the proposed antenna with equal meandered monopoles.	58
Fig. 23: Realized gain pattern at the resonant frequency (2.425 GHz) of the antenna with equal meandered monopoles.....	58
Fig. 24: Surface currents on the two meandered monopoles at the resonant frequency of the overall structure (2.425 GHz).	59

Fig. 25: Front view (a) and back view (b) of the proposed antenna with slightly different meandered monopoles. Antenna dimensions are: $R_{BT} = 5$ mm, $H_m = 4.5$ mm, $g_m = 0.3$ mm, $w_m = 0.48$ mm, $L = 3$ mm.	60
Fig. 26: Reflection coefficient amplitude of the proposed antenna with slightly different monopoles (red-solid line), compared to the one of the previous case (black-dashed line).....	61
Fig. 27: Surface currents on the two meandered monopoles at the lowest resonant frequency of the overall structure shown in Fig. 6.....	61
Fig. 28: Surface currents on the two meandered monopoles at the highest resonant frequency of the overall structure shown in Fig. 6.....	62
Fig. 29: Realized gain pattern at the lowest resonant frequency (2.416 GHz) of the antenna with slightly different monopoles.	62
Fig. 30: Realized gain pattern at the highest resonant frequency (2.461 GHz) of the antenna with slightly different monopoles.	63
Fig. 31: 3D view of the novel resonator (left) and of the proposed polarization transformer where we can see the two driven monopoles connected across an electrically small aperture made in a metallic screen (right).....	70
Fig. 32: Geometrical sketch of the proposed polarization transformer and its integration with a linearly polarized rectangular waveguide.	71
Fig. 33: Dimensions of the electrically small resonator used to design the polarization transformer: $R1_CLL1 = R1_CLL2 = 15$ mm, $R2_CLL1 = 11.73$ mm, $R2_CLL2 = 12.21$ mm, $H1_CLL1 = 13.04$ mm, $H1_CLL2 = 13.5$ mm, $H2_CLL1 = 13.9$ mm, $H2_CLL2 = 14$ mm, $W_CLL1 = W_CLL2 = 1.4$ mm, $G1 = 0.3$ mm, $G2 = 0.2$ mm, $G3 = 2$ mm. Metallizations are printed on the two sides of an 0.7874 mm thick Rogers Duroid 5880 dielectric slab.	72
Fig. 34: Reflection coefficient of an open ended rectangular waveguide (dash-dotted line), of the same waveguide with a sub-wavelength circular aperture (dashed line), and of the structure shown in Fig. 2.....	72
Fig. 35: Realized gain radiation patterns at 1.575 GHz of the structure shown in Fig. 2 ($\varphi = 0^\circ$).	73

Fig. 36: Realized gain radiation patterns at 1.575 GHz of the structure shown in Fig. 2 ($\varphi = 90^\circ$).....	73
Fig. 37: Axial ratio for the main beam direction of the structure shown in Fig. 2.	74
Fig. 38: Top view (left) and perspective view (right) of the self-filtering circularly polarized horn antenna.....	75
Fig. 39: Reflection coefficient of the self-filtering circularly polarized horn antenna shown in Fig. 8.....	76
Fig. 40: Axial ratio for the main beam direction of the self-filtering circularly polarized horn antenna shown in Fig. 8.....	77
Fig. 41: Realized gain radiation patterns at 1.575 GHz of the self-filtering circularly polarized horn antenna shown in Fig. 8 ($\varphi = 0^\circ$).....	77
Fig. 42: Realized gain radiation patterns at 1.575 GHz of the self-filtering circularly polarized horn antenna shown in Fig. 8 ($\varphi = 90^\circ$).....	78
Fig. 43: Geometrical sketch of the proposed polarization transformer with dimensions: $L = 5.8$ mm, $L_{a1} = 0.3$ mm, $L_{a2} = 0.9$ mm, $L_m = 0.8$ mm, $W_d = 0.4$ mm, $W_a = 0.4$ mm.	79
Fig. 44: Geometrical sketch of the proposed polarization transformer and its integration with a linearly polarized rectangular waveguide.....	80
Fig. 45: Reflection coefficient amplitude of an open ended rectangular waveguide (dashed line) and of the structure shown in Fig. 2 (solid line).	80
Fig. 46: Realized gain patterns at 15.75 GHz of the structure shown in Fig. 2: (left) $\varphi = 0^\circ$; (right) $\varphi = 90^\circ$	81
Fig. 47: Axial ratio for the main beam direction of the structure shown in Fig. 2.	81
Fig. 48: Side view (left) and perspective view (right) of the filtering circularly polarized horn antenna. Corrugated horn dimensions: $D_s = 6.3$ mm, $L_g = 33$ mm, $L_h = 25.6$ mm, $L_t = 5$ mm, $W_s = 1.3$ mm, $W_r = 1.3$ mm.	82
Fig. 49: Simulated and measured reflection coefficient amplitude of the self-filtering circularly polarized horn antenna shown in Fig. 6.....	83
Fig. 50: Simulated and measured axial ratio for the main beam direction of the self-filtering circularly polarized horn antenna shown in Fig. 6.....	84

Fig. 51: Simulated and measured realized gain patterns at 15.85 GHz of the self-filtering circularly polarized horn antenna shown in Fig. 6: (left) $\phi = 0^\circ$; (right) $\phi = 90^\circ$	84
Fig. 52: Realized gain (solid line) and directivity (dashed line) of the self-filtering circularly polarized horn antenna shown in Fig. 6.	85
Fig. 53: Photographs showing: (a) side view of the overall antenna structure consisting of a coaxial-to-waveguide transition, the proposed polarization transformer, and a corrugated conical horn; (b) front view of the overall antenna structure; (c) the realized polarization transformer; (d) the overall antenna structure in the Satimo StarLab.	86
Fig. 54: Geometrical sketch of the proposed horn antenna with the notched-band filter: (a) perspective view; (b) front view; (c) side view.	88
Fig. 55: Reflection coefficient amplitude at the input port of the structure shown in Fig. 1 for different positions of the SRR.	89
Fig. 56: Measured and simulated reflection coefficient amplitude at the input port of the structure shown in Fig. 1 for the case of $d = 15$ mm.	89
Fig. 57: Measured and simulated realized gain in the main beam direction of the proposed horn antenna with the notched-band filter and of the corresponding standard horn antenna.	90
Fig. 58: Close-up of the measured and simulated realized gain in the main beam direction of the proposed horn antenna with the notched-band filter and of the corresponding standard horn antenna.	90
Fig. 59: Simulated and measured realized gain patterns of the proposed horn antenna with and without the notched-band filter on the E-plane (left column) and H-plane (right column) at: (a) 9 GHz, (b) 10 GHz and (c) 11 GHz.	91
Fig. 60: Geometrical sketch of the proposed horn antenna with the dual-band-notch filter: (a) perspective view; (b) front view; (c) side view.	92
Fig. 61: Simulated and measured reflection coefficient amplitude at the input port of the horn filtenna with a dual band-stop characteristic.	93

Fig. 62: Simulated realized gain in the main beam direction of the horn antenna with and without a dual-band-stop filter.....	93
Fig. 63: Close-up of the simulated realized gain in the main beam direction of the horn antenna with and without a dual-band-stop filter.	94
Fig. 64: Photographs showing: top (a) and bottom (b) views of the realized filtering module; (c) the filtering module fixed in the horn antenna; (d) perspective view of the proposed self-filtering horn antenna; (e) the proposed structure placed inside the near-field measurement system.....	95
Fig. 65: Photographs showing the transmission measurement setup.....	96
Fig. 66: Power transmission between two single-band filtering horn antennas, two standard horns and between a standard horn and the single-band filtering horn antenna, in the setup shown in Fig. 11.	96
Fig. 67: Geometrical sketch of the proposed complementary resonator with dimensions: $L = 8.2$ mm, $L_{a1} = 2$ mm, $L_{a2} = 1.9$ mm, $H_{m1} = 1.8$ mm, $H_{m2} = 1.5$ mm, $W_d = 0.4$ mm, $W_a = 0.4$ mm. The resonator is drilled in a metallic sheet.	103
Fig. 68: Geometrical sketch of the proposed rectangular-to-circular waveguide transition.	103
Fig. 69: Electric field lines at the waveguide ports of the structure shown in Fig. 2: (a) TE_{10} -mode of the rectangular waveguide, (b) and (c) degenerate TE_{11} -modes of the circular waveguide.....	104
Fig. 70: Simulated magnitude of the scattering parameters of the structure shown in Fig. 2.	105
Fig. 71: Simulated phase difference between the degenerate TE_{11} -modes at port 2 of the structure shown in Fig. 2.....	105
Fig. 72: Right view (a), left view (b), perspective view (c) and top view (d) of the power divider having output ports in circular waveguides.....	106
Fig. 73: Simulated magnitude of the scattering parameters of the structure shown in Fig. 6.	107

Fig. 74: Simulated phase difference between the degenerate TE_{11} -modes at port 2 (black-solid line) and port 3 (red-dashed line) of the structure shown in Fig. 6.	107
Fig. 75: Righth view (a), left view (b), perspective view (c) and top view (d) of the power divider with output ports in rectangular waveguides. Complementary resonator dimensions are: $L = 8.2$ mm, $L_{a1} = 2$ mm, $L_{a2} = 2$ mm, $H_{m1} = 1.5$ mm, $H_{m2} = 1.5$ mm, $W_d = 0.4$ mm, $W_a = 0.4$ mm.	108
Fig. 76: Simulated magnitude of the scattering parameters of the structure shown in Fig. 9.	108
Fig. 77: Perspective view of the proposed orthomode transducer.	109
Fig. 78: Geometrical sketch of the linearly polarized complementary resonator with dimensions: $L = 8.6$ mm, $L_a = 3.5$ mm, $H_m = 2$ mm, $W_d = 0.4$ mm, $W_a = 0.4$ mm.	110
Fig. 79: Simulated magnitude of the scattering parameters of the structure shown in Fig. 11.	110
Fig. 80: Geometrical sketch describing the structure of a traditional Salisbury screen.	112
Fig. 81: Simulated amplitude of the transmission and reflection coefficients (for normal incidence) of the proposed metasurface (inset: geometrical sketch of the metasurface and dimensions of the metallic rings).	113
Fig. 82: (a) Commercial graphite powder spray produced by ATAL SrL; (b) A realized resistive sheet composed by a plastic sheet covered by a proper amount of graphite powder. The two images are not in scale.	115
Fig. 83: Application of the Van der Pauw method for the resistive sheet characterization.	115
Fig. 84: Surface resistance exhibited by the 18 realized samples compared to the relative graphite powder surface density.	117
Fig. 85: Experimental setup used to measure the reflection coefficient of the realized resistive sheets. In the inset it is shown a properly shaped resistive sheet supported by a sample holder.	118

Fig. 86: Comparison between the measured and the simulated amplitude of the S11 parameter for two resistive sheets with $41 \Omega/sq$ and $141 \Omega/sq$, respectively.	118
Fig. 87: (a) Geometrical sketch, (b) rear view and (c) front view of the proposed metamaterial-inspired absorber.....	119
Fig. 88: Photograph of the measurement system consisting of two high-gain pyramidal horn antenna and the sample holder.....	120
Fig. 89: Absorption of the metamaterial-inspired absorber shown in Fig. 3.	120
Fig. 90: Geometrical sketch of a circular patch antenna. The main geometrical parameters are the radius of the patch a and the thickness of the dielectric substrate h	127
Fig. 91: Ratio between the amplitude of the terms A and B in the case of a circular patch antenna working in a CP TM_{21} mode for different values of substrate permittivity.	129
Fig. 92: Phase patterns (in degree) of the x (left) and y (right) component of the radiated electric field in the case of: (a) RHCP TM_{11} mode; (b) RHCP TM_{21} mode; (c) RHCP TM_{31} mode.....	130
Fig. 93: Top view of the elliptical patch antenna. The inner conductor of the coaxial cable is connected to the point p ($x = 8.75$ mm; $y = 21$ mm). The origin of the reference system is at the shape centre. Antenna dimensions are: $A_1 = 75,2$ mm, $A_2 = 81.6$ mm, and $L = 100$ mm.	131
Fig. 94: Simulated (red-solid line) and measured (black-dashed line) reflection coefficient amplitude of the proposed elliptical patch antenna shown in Fig. 4.....	132
Fig. 95: Phase patterns at 2.4 GHz of the x (left) and y (right) component of the radiated electric field by the elliptical patch antenna, shown in Fig. 4, working in a RHCP TM_{21} mode.....	133
Fig. 96: Simulated Azimuth (left) and Elevation (right) radiation phase patterns at 2.4 GHz of the elliptical patch antenna, shown in Fig. 4, working in a RHCP TM_{21} mode.	133

Fig. 97: 3-D directivity pattern at 2.4 GHz of the elliptical patch antenna, shown in Fig. 4, working in a RHCP TM_{21} mode.	133
Fig. 98: Photograph showing the realized elliptical patch antenna with the dimensions given in Fig. 4.....	134
Fig. 99: Measured Azimuth (left) and Elevation (right) radiation phase patterns at 2.4 GHz of the prototype shown in Fig. 9.	135

List of Tables

Table 1: Nominal values of the real lumped elements of the circuit shown in Fig. 8.	35
Table 2: Summary of the operation frequencies and radiation properties for the different combinations of the switch status.	52

This page is intentionally left blank.

Esteso Sommario

(Italiano)

Il termine “metamateriale” (MTM) fa riferimento ad un ampio insieme di materiali artificiali, tipicamente sintetizzati inserendo delle opportunamente strutture metalliche di particolare forma e dimensione all’interno di un mezzo dielettrico ospitante [1]-[4]. I parametri geometrici ed elettromagnetici di tali inclusioni sono progettati per alterare la risposta del materiale ospitante ed ottenere proprietà anomale non riscontrabili nei materiali convenzionali alle frequenze di interesse. Soltanto per citare un esempio, sebbene alcuni materiali naturali (e.g. metalli nobili e alcuni semiconduttori) mostrano valori anomali (i.e. negativi o nulli) della permittività elettrica alle frequenze dell’infrarosso, visibili e ultraviolette [5]-[6], non sono noti materiali naturali con caratteristiche simili alle frequenze delle microonde. Allo stesso modo, le proprietà magnetiche dei materiali naturali sono limitate alle frequenze radio ed alle basse microonde [7] e, di conseguenza, valori anomali di permeabilità magnetica non sono naturalmente disponibili nel dominio visibile, infrarosso e ultravioletto. Tuttavia, quando la natura non ci fornisce i valori necessari dei parametri elettromagnetici, i MTM possono essere utilizzati con successo per ottenere i valori anomali desiderati.

Ad esempio, come anticipato teoricamente in [8] e dimostrato sperimentalmente in [9], è possibile ottenere un MTM caratterizzato da un indice di rifrazione negativo alle frequenze delle microonde combinando opportunamente sottili fili metallici [10] e split-ring resonator (SRR). Infatti, poichè in tale materiale le inclusioni e la distanza tra di esse sono inferiori rispetto alla lunghezza d’onda operativa, è possibile introdurre valori efficaci di permittività, permeabilità e indice di rifrazione, i quali possono assumere valori anomali. La loro sintesi prende spunto dall’idea introdotta da Pendry [9], secondo la quale una serie di dipoli elettrici orientati causa un comportamento risonante della permittività elettrica efficace del mezzo. In modo simile, un insieme di dipoli magnetici genera un’analogia risonanza della permeabilità magnetica efficace associata al MTM. Se le due risonanze si verificano nello stesso intervallo di frequenze, siamo in grado di

sintetizzare un materiale con un indice di rifrazione negativo in un determinato intervallo di frequenze.

L'elemento fondamentale per la realizzazione del primo MTM è stato quindi lo SRR, il quale è un risonatore miniaturizzato utile per ottenere il magnetismo artificiale alle frequenze delle microonde. Un singolo SRR è costituito da due anelli aperti concentrici di materiale metallico, le cui aperture sono poste a lati opposti della struttura. Tale configurazione permette di aumentare la capacità totale del risonatore rispetto a quella di una struttura a singolo anello, aggiungendo una capacità distribuita tra i due anelli concentrici. In questo modo, la frequenza di risonanza del risonatore può essere significativamente ridotta per raggiungere una dimensione elettrica dell'ordine di $\lambda/10$. Dopo quanto proposto in [9], sono state introdotte molte inclusioni magnetiche differenti per ottenere un maggiore grado di miniaturizzazione, rimuovere la bi-anisotropia intrinseca che caratterizza il comportamento di uno SRR [11]-[14], e ottenere una risposta isotropa [15]-[18].

Accanto a questi sforzi modellistici, sono state investigate molte proprietà innovative dei MTM. In particolare, l'effetto di super-risoluzione di un MTM con indice di rifrazione negativo ha mostrato come sia possibile superare il limite fisico della diffrazione. Una lente convenzionale, infatti, è in grado di focalizzare un dettaglio con un limite ben noto in ottica: fissata la frequenza operativa, tale dettaglio non può essere inferiore alla corrispondente lunghezza d'onda di lavoro. Una lamina opportunamente progettata di MTM può invece andare idealmente al di sotto del limite fisico della diffrazione, focalizzando dettagli con dimensioni inferiori alla lunghezza d'onda. Altre applicazioni interessanti dei MTM derivano dall'idea che, se utilizziamo insieme una coppia di materiali artificiali coniugati, possiamo progettare cavità risonanti di dimensioni trasversali molto inferiori alla lunghezza d'onda. A partire da questa idea di base, sono stati proposti numerosi componenti e dispositivi innovativi basati sulle proprietà dei MTM, come ad esempio super-lenti [19]-[20], iper-lenti [21], rivestimenti per l'invisibilità elettromagnetica [22]-[24], componenti radianti compatti [25]-[29], dispositivi per l'aumento della trasmissione da foro elettricamente piccolo [30]-[36], filtri [37], assorbitori [38], ecc. Inoltre, negli ultimi anni, sfruttando le potenzialità offerte dalla nano-fabbricazione, il range operativo in frequenza dei MTM è stato esteso

fino alle frequenze ottiche [39]-[43]. In questo caso, tuttavia, i risonatori magnetici usati alle microonde non possono essere facilmente impiegati [44] e, di conseguenza, sono stati introdotti design alternativi con un minore grado di miniaturizzazione [45]-[46], o basati su approcci concettualmente differenti [47]-[48].

Tuttavia, qualunque sia la gamma di frequenze di interesse, i materiali magnetici artificiali o più in generale i MTM presentano alcune limitazioni intrinseche. A causa di considerazioni energetiche, infatti, ogni MTM passivo deve essere necessariamente un mezzo dispersivo [49]. I valori desiderati dei parametri elettromagnetici sono quindi ottenuti soltanto in un ristretto intervallo di frequenze e, di conseguenza, la banda operativa dei componenti basati su MTM è tipicamente a sua volta limitata. Inoltre, come risulta chiaro dalle relazioni di causalità di Kramers-Kronig, il fenomeno di dispersione è sempre legato a meccanismi di perdita [49], i quali riducono ulteriormente le potenzialità dei MTM.

Il **Capitolo 1** di questa tesi è, quindi, dedicato all'impiego di elementi attivi di tipo non-Foster per aumentare la banda operativa di uno SRR per possibili applicazioni nei componenti ispirati ai MTM. Innanzitutto, determineremo la tipologia circuitale del carico attivo richiesta per compensare la reattanza intrinseca dello SRR ed ottenere un comportamento a banda larga. Successivamente, mostreremo che la stessa procedura può essere applicata con successo al caso di un'antenna a monopolo basata su SRR e, in linea di principio, a qualsiasi dispositivo ispirato ai MTM che fa uso di SRR. Infine, integrando un simulatore circuitale ed uno elettromagnetico, proporrò una possibile implementazione realistica del carico attivo, basata sull'impiego di elementi circuitali disponibili in commercio. I risultati ottenuti (ampliamento di sette volte della banda di impedenza dell'antenna in esame) dimostrano che carichi attivi di tipo non-Foster possono essere usati con successo per aumentare la larghezza di banda, altrimenti intrinsecamente ridotta, di MTM passivi basati su SRR e dei componenti ispirati ai MTM. Vedremo inoltre che i problemi realizzativi legati alla dispersione degli elementi circuitali, agli effetti parassiti e alla stabilità del circuito attivo possono essere opportunamente tenuti in considerazione in fase di progetto.

Il **Capitolo 2** di questa tesi sarà invece dedicato al progetto di nuovi elementi radianti compatti e multifunzione ispirati ai concetti dei MTM. Per prima cosa, presenteremo il

progetto di un'antenna a monopolo stampato caricata con due SRR identici. L'idea è quella di utilizzare gli SRR non solo per miniaturizzare le dimensioni dell'antenna ma anche per introdurre risonanze multiple che possono essere opportunamente selezionate utilizzando switch elettronici posti nei quattro gap dei due SRR. Combinando opportunamente gli stati ON/OFF dei quattro switch, infatti, vedremo come sia possibile cambiare la frequenza operativa e/o la forma del diagramma di radiazione dell'antenna a monopolo o aggiungere nuove frequenze operative. Successivamente, presenteremo invece un'antenna compatta costituita da due monopoli a meandro ortogonali che agiscono come elementi parassiti di un bow-tie alimentato. In particolare, mostreremo che utilizzando due monopoli con dimensioni leggermente differenti è possibile ottenere una maggiore larghezza di banda di impedenza. Utilizzando tale approccio, presenteremo un'antenna compatta operante nella banda del Wi-Fi a 2.4 GHz con dimensioni elettriche complessive pari a $\lambda_0/6 \times \lambda_0/12 \times \lambda_0/75$.

Nel **Capitolo 3**, focalizzeremo invece la nostra attenzione sul progetto di antenne ad horn con moduli filtranti integrati ispirati ai MTM. A tale scopo, proporremo innanzitutto l'utilizzo di antenne compatte per il progetto di un nuovo setup per l'aumento della trasmissione da foro elettricamente piccolo. Tale setup consiste di un disco metallico circolare con un'apertura attraverso la quale sono poste due coppie di antenne elettricamente piccole a polarizzazione circolare. Mostriamo inoltre che la struttura proposta, se posta alla fine di una guida d'onda rettangolare aperta, è in grado di cambiare la sua polarizzazione da lineare a circolare. Successivamente, integrando tale trasformatore di polarizzazione in un'antenna ad horn, mostreremo come sia possibile ottenere un'antenna ad horn filtrante a polarizzazione circolare. Tuttavia, tale modulo filtrante non è planare, è costituito da strutture differenti poste ortogonalmente tra loro, richiede l'utilizzo di materiali dielettrici comportando una riduzione di efficienza, e può operare soltanto con segnali di bassa potenza (i.e. può operare soltanto in modalità ricevente). Al fine di superare tali limiti, proporremo quindi un nuovo trasformatore di polarizzazione costituito da un risonatore complementare elettricamente piccolo intagliato su uno schermo metallico. Mostriamo prima che tale componente è in grado di trasformare la polarizzazione lineare di una guida d'onda rettangolare operante nel suo modo fondamentale in una circolare. Successivamente,

integrando tale convertitore di polarizzazione in un horn conico, mostreremo come sia possibile ottenere un'antenna ad horn filtrante in polarizzazione circolare. Il comportamento della struttura proposta sarà validato tramite simulazioni numeriche e misurazioni effettuate su un prototipo.

Si noti, tuttavia, che tale approccio prevede l'inserimento di uno schermo metallico ortogonale alla direzione di propagazione del campo elettromagnetico; di conseguenza, esso può essere utilizzato soltanto per componenti a microonde che debbano mostrare un comportamento di tipo passa-banda. Al fine di progettare antenne ad horn filtranti o componenti a microonde con una caratteristica di tipo notch (elimina banda), dobbiamo quindi rimuovere lo schermo metallico e progettare un'inclusione risonante che sia in grado di immagazzinare/dissipare energia ad una data frequenza, ottenendo così una banda proibita in uno stretto intervallo di frequenze. A tale scopo, presenteremo quindi il progetto di antenne ad horn filtranti con un comportamento elimina banda ottenuto attraverso l'utilizzo di risonatori magnetici elettricamente piccoli. In particolare, uno SRR realizzato su un substrato dielettrico Rogers Duroid™ RT5870 sarà inserito all'interno di un'antenna ad horn ad una opportuna distanza dalla sua apertura. Intorno alla frequenza di risonanza dello SRR la trasmissione sarà quindi fortemente ridotta ottenendo così un comportamento di tipo notch. Al fine di estendere tale risultato al caso di operatività dual-band, proporremo inoltre il progetto di un modulo filtrante costituito da due SRR con dimensioni differenti. Anche in questo caso, la validità dell'approccio proposto sarà verificata attraverso un opportuno set di simulazioni full-wave e esperimenti condotti su prototipi.

Mentre nei primi capitoli saranno presentate diverse tipologie di strutture radianti, nel **Capitolo 4** affronteremo il progetto di nuovi componenti a microonde. In particolare, il trasformatore di polarizzazione planare presentato nel *Capitolo 3* sarà utilizzato per progettare una nuova classe di componenti in guida d'onda. Innanzitutto, presenteremo una transizione in guida d'onda da rettangolare a circolare che permetta di collegare efficacemente guide d'onda con sezioni trasversali differenti e di trasformare il modo TE_{10} a polarizzazione lineare della guida d'onda rettangolare in un modo TE_{11} a polarizzazione circolare della guida d'onda circolare. Successivamente, utilizzando strutture simili, presenteremo il progetto di due divisori di potenza e di un trasduttore di

modi ortogonali. Tutti questi componenti, impiegando soltanto sottili fogli metallici opportunamente forati, possono essere integrati nei sistemi standard di trasmissione in guida d'onda senza aumentare la loro occupazione di spazio. Come ulteriore esempio di componenti a microonde ispirato ai concetti dei MTM, mostreremo inoltre un assorbitore innovativo a basso costo operante nella banda X. Esso consiste di un singolo foglio resistivo opportunamente spaziato da una metasuperficie a doppio ring. Il suo principio di funzionamento è simile a quello di uno schermo di Salisbury, nel quale un foglio resistivo a $377 \Omega/\text{sq}$ è posto a $\lambda/4$ da un piano metallico. Tuttavia, nella nostra configurazione, la metasuperficie sostituirà il supporto metallico riducendo la percentuale di metallo utilizzata. Ciò è molto conveniente quanto l'assorbitore è utilizzato per ridurre la sezione trasversale radar o radar cross section (RCS) di oggetti non metallici. In un simile scenario operativo, l'assenza di un piano metallico permette di ridurre notevolmente il peso della struttura complessiva e di aumentare in maniera minore la RCS dell'oggetto al di fuori della banda operativa dell'assorbitore. Le prestazioni della metasuperficie e dell'assorbitore complessivo saranno valutate attraverso simulazioni full-wave e misurazioni effettuate su un prototipo.

Tutti i componenti suddetti sono ispirati al concetto di MTM e permettono di eseguire diverse operazioni sul segnale elettromagnetico, come un filtraggio di tipo passa-banda o elimina banda o la trasformazione della polarizzazione. Poiché molti di essi sono costituiti da una singola particella ispirata ai MTM, tali componenti possono essere facilmente integrati nell'elemento radiante, eseguendo la manipolazione del segnale direttamente sul campo elettromagnetico trasmesso o ricevuto. Un'altra possibile manipolazione che può essere eseguita su un segnale elettromagnetico è la generazione del momento angolare orbitale (OAM). In particolare, la recente estensione del concetto di OAM dalle frequenze ottiche a quelle delle microonde ha portato alcuni ricercatori ad esplorare come le tecniche radiative a microonde possano essere utilizzate per irradiare un campo elettromagnetico con OAM non nullo. A tal riguardo, il **Capitolo 5** mira a presentare un nuovo approccio per generare un campo con OAM non nullo attraverso l'utilizzo di una singola antenna a patch. Utilizzando il modello a cavità, per prima cosa analizzeremo il campo irradiato da un patch circolare standard e mostreremo che un modo TM_{nm} a polarizzazione circolare eccitato mediante due cavi coassiali è in grado di

generare un campo elettromagnetico con OAM di ordine $\pm(n-1)$. Successivamente, al fine di ottenere una struttura più semplice con un singolo feed, progetteremo un'antenna a patch ellittico in grado di irradiare un modo TM_{21} a polarizzazione circolare destra. Utilizzando simulazioni full-wave ed esperimenti su un prototipo fabbricato, mostreremo che l'antenna proposta è in grado di irradiare efficacemente un campo elettromagnetico con un OAM del primo ordine.

References

- [1] G.V. Eleftheriades, and K.G. Balmain, *Negative Refraction Metamaterials: Fundamental Principles and Applications*. Hoboken, NJ: Wiley-IEEE Press, 2005.
- [2] N. Engheta, and R.W. Ziolkowski, *Electromagnetic Metamaterials: Physics and Engineering Explorations*. Hoboken, NJ: Wiley-IEEE Press, 2006.
- [3] R. Marqués, F. Martín, M. Sorolla, and F. Capolino, *Metamaterials with Negative Parameters: Theory, Design and Microwave Applications*. Hoboken, NJ: Wiley-Interscience, 2008.
- [4] S. Zouhdi, A. Sihvola, and A. P. Vinogradov, *Metamaterials and Plasmonics: Fundamentals, Modelling, Applications*. Dordrecht, NL: Springer-Verlag GmbH, 2008.
- [5] P.B. Johnson, R. W. Christy, "Optical constants of the noble metals," *Phys. Rev. B*, Vol. 6, pp. 4370-4379, 1972.
- [6] E.D. Palik, *Handbook of Optical Constants of Solids*, Boston, NE: Academic Press, 1998.
- [7] L.D. Landau, L.P. Pitaevskii, and E.M. Lifshitz, *Electrodynamics of Continuous Media, Second Edition: Volume 8*. Oxford, EN: Pergamon Press, 1984.
- [8] V.G. Veselago, "The electrodynamics of substances with simultaneously negative values of ϵ and μ ," *Sov. Phys. Uspekhi*, Vol. 10, pp. 509–514, 1968.
- [9] D.R. Smith, W.J. Padilla, D.C. Vier, S.C. Nemat-Nasser, and S. Schultz, "Composite medium with simultaneously negative permeability and permittivity," *Phys. Rev. Lett.*, Vol. 84, pp. 4184-4187, 2000.
- [10] W. Rotman, "Plasma simulation by artificial dielectrics and parallel-plate media," *IRE Trans. Antennas Propagat.*, Vol. 10, pp. 82-25, 1962.
- [11] R. Marqués, F. Medinaand, and R. Rafii-El-Idrissi, "Role of bi-anisotropy in negative permeability and left handed metamaterials," *Phys. Rev. B*, Vol. 65, 144441, 2002.
- [12] R. Marqués, F. Mesa, J. Martel, and F. Medina, "Comparative analysis of edge and broadside coupled split ring resonators for metamaterial design. Theory and experiment," *IEEE Trans. Antennas Propagat.*, Vol. 51, pp. 2572–2581, 2003.

- [13] R. Marqués, J. D. Baena, J. Martel, F. Medina, F. Falcone, M. Sorolla, and F. Martin, "Novel small resonant electromagnetic particles for metamaterial and filter design," *Proc. ICEAA '03*, pp. 439–442, Torino, Italy, 2003.
- [14] J. D. Baena, R. Marqués, F. Medina, and J. Martel, "Artificial magnetic metamaterial design by using spiral resonators," *Phys. Rev. B*, Vol. 69, 014402, 2004.
- [15] Ph. Gay-Balmaz, and O. J. F. Martin, "Efficient isotropic magnetic resonator," *Appl. Phys. Lett.*, Vol. 81, pp. 939–941, 2002.
- [16] C. R. Simovski, and B. Sauviac, "Towards creating isotropic microwave composites with negative refraction," *Radio Sci.*, Vol. 39, RS2014, 2004.
- [17] C. R. Simovski, and S. He, "Frequency range and explicit expressions for negative permittivity and permeability for an isotropic medium formed by a lattice of perfectly conducting Ω particles," *Phys. Lett. A*, Vol. 311, pp. 254–263, 2003.
- [18] M.M. I. Saadoun, and N. Engheta "A reciprocal phase shifter using a novel pseudo-chiral or Ω medium," *Microwave Opt. Tech. Lett.*, Vol. 5, pp. 184–188, April 1992.
- [19] J.B. Pendry, "Negative refraction makes a perfect lens," *Phys. Rev. Lett.*, Vol. 85, pp. 3966–3969, 2000.
- [20] P. Belov, R. Marques, S. Maslovski, I. Nefedov, M. Silverinha, C. Simovski, and S. Tretyakov, "Experimental study of the subwavelength imaging by a wire medium slab," *Phys. Rev. B*, Vol. 67, 113103, 2003.
- [21] W. Zhang, H. Chen, and H.O. Moser, "Subwavelength imaging in a cylindrical hyperlens based on S-string resonators," *Appl. Phys. Lett.*, Vol. 98, 073501, 2011.
- [22] A. Alù and N. Engheta, "Achieving transparency with plasmonic and metamaterial coatings," *Phys. Rev. E*, Vol. 72, 016623, 2005.
- [23] M. G. Silveirinha, A. Alu, and N. Engheta, "Parallel-plate metamaterials for cloaking structures," *Phys. Rev. E*, Vol. 75, 036603, 2007.
- [24] B. Edwards, A. Alu, M. Silveirinha, and N. Engheta, "Experimental verification of plasmonic cloaking at microwave frequencies with metamaterials," *Phys. Rev. Lett.*, Vol. 103, 153901, 2009.
- [25] R.W. Ziolkowski and A.D. Kipple, "Application of double negative materials to increase the power radiated by electrically small antennas," *IEEE Trans. Antennas Propagat.*, Vol. 52, pp. 2626–2640, 2003.
- [26] F. Qureshi, M.A. Antoniades, and G. V. Eleftheriades, "A compact and low-profile metamaterial ring antenna with vertical polarization," *IEEE Antennas Wireless Propag. Lett.*, Vol. 4, pp. 333–336, 2005.
- [27] A. Alù, F. Bilotti, N. Engheta, and L. Vegni, "Sub-wavelength planar leaky-wave components with metamaterial bilayers," *IEEE Trans. Antennas Propagat.*, Vol. 55, pp. 882–891, 2007.

- [28] A. Alù, F. Bilotti, N. Engheta, and L. Vegni, "Subwavelength, Compact, Resonant Patch Antennas Loaded With Metamaterials," *IEEE Trans. Antennas Propagat.*, Vol. 55, pp. 13-15, 2007.
- [29] F. Bilotti, A. Alù, and L. Vegni, "Design of miniaturized metamaterial patch antennas with μ -negative loading," *IEEE Trans. Antennas Propagat.*, Vol. 56, pp. 1640-1647, 2008.
- [30] D. E. Grupp, H. J. Lezec, T. Thio, and T. W. Ebbesen, "Beyond the Bethe limit: tunable enhanced light transmission through a single sub-wavelength aperture," *Adv. Mat.*, Vol. 11, pp. 860-862, 1999.
- [31] A. Alù, F. Bilotti, N. Engheta, and L. Vegni, "Metamaterial covers over a small aperture," *IEEE Trans. Antennas Propagat.*, Vol. 54, pp. 1632-1643, 2006.
- [32] A. Alù, F. Bilotti, N. Engheta, and L. Vegni, "A review on the potential use of metamaterial layers for increasing the transmission through a single sub-wavelength aperture in a flat opaque screen," in *Periodic Structures*, ed. by M. Bozzi and L. Perregrini, Kerala, India, 2006, ch. 10, pp. 271-291.
- [33] F. Bilotti, L. Scorrano, E. Ozbay, and L. Vegni, "Enhanced transmission through a sub-wavelength aperture: Resonant approaches employing metamaterials," *J. Opt. A*, Vol. 11, 114029, 2009
- [34] K. Aydin, A.O. Cakmak, L. Sahin, Z. Li, F. Bilotti, L. Vegni, and E. Ozbay, "Split-ring-resonator-coupled enhanced transmission through a single subwavelength aperture," *Phys. Rev. Lett.*, Vol. 102, pp. 013904, 2009.
- [35] K.B. Alici, F. Bilotti, L. Vegni, and E. Ozbay, "Optimization and tunability of deep subwavelength resonators for metamaterial applications: complete enhanced transmission through a subwavelength aperture," *Opt. Expr.*, Vol. 17, pp. 5933-5943, 2009.
- [36] A.O. Cakmak, K. Aydin, E. Colak, Z. Li, F. Bilotti, L. Vegni, and E. Ozbay, "Enhanced transmission through a sub-wavelength aperture using metamaterials," *Appl. Phys. Lett.*, Vol. 95, 052103, 2009.
- [37] J. Martel, R. Marques, F. Falcone, J.D. Baena, F. Medina, F. Martin, and M. Sorolla, "A new LC series element for compact bandpass filter design," *IEEE Microwave Wireless Compon. Lett.*, Vol. 14, pp. 210-212, 2004.
- [38] F. Bilotti, L. Nucci, and L. Vegni, "An SRR based microwave absorber," *Microw. Opt. Technol. Lett.*, Vol. 48, pp. 2171-2175, 2006.
- [39] N. Fang, H. Lee, C. Sun, and X. Zhang, "Sub-diffraction-limited optical imaging with a silver superlens," *Sci.*, Vol. 308, pp. 534-537, 2005.
- [40] A. Salandrino, and N. Engheta, "Far-field subdiffraction optical microscopy using metamaterial crystals: Theory and simulations," *Phys. Rev. B*, Vol. 74, 075103, 2006.
- [41] Z. Liu, H. Lee, Y. Xiong, C. Sun, and X. Zhang, "Far-field optical hyperlens magnifying sub-diffraction-limited objects," *Sci.*, Vol. 315, pp. 1686, 2007.

-
- [42] M. Silveirinha, A. Alu and N. Engheta, "Infrared and optical invisibility cloak with plasmonic implants based on scattering cancellation," *Phys. Rev. B*, 78, 075107, 2008.
- [43] N. Engheta, "Circuits with light at nanoscales: Optical nanocircuits inspired by metamaterials," *Sci.*, Vol. 317, pp. 1698-1702, 2007.
- [44] J. Zhou, T. Koschny, M. Kafesaki, E.N. Economou, J.B. Pendry, and C.M. Soukoulis, "Saturation of the magnetic response of split-ring resonators at optical frequencies," *Phys. Rev. Lett.*, Vol. 95, 223902, 2005.
- [45] G. Dolling, C. Enkrich, M. Wegener, J. F. Zhou, C. M. Soukoulis, and S. Linden, "Cut-wire pairs and plate pairs as magnetic atoms for optical metamaterials," *Opt. Expr.*, Vol. 30, pp. 3198-3200, 2005.
- [46] M. Kafesaki, I. Tsiapa, N. Katsarakis, Th. Koschny, C. M. Soukoulis, and E. N. Economou, "Left-handed metamaterials: The fishnet structure and its variations," *Phys. Rev. B*, Vol. 75, 235114, 2007.
- [47] A.N. Grigorenko, A.K. Geim, H.F. Gleeson, Y. Zhang, A.A. Firsov, I.Y. Khrushchev, J. Petrovic, "Nanofabricated media with negative permeability at visible frequencies," *Nat.*, Vol. 438, pp. 335-338, 2005.
- [48] A. Alù, and N. Engheta, "The quest for magnetic plasmons at optical frequencies," *Opt. Expr.*, Vol. 17, pp. 5723-5730, 2009.
- [49] S.A. Tretyakov, and S.I. Maslovski, "Veselago materials: What is possible and impossible about the dispersion of the constitutive parameters," *IEEE Antennas Propag. Mag.*, Vol. 49, pp. 37-43, 2007. *This page is intentionally left blank.*

Introduction

The term “metamaterial” (MTM) refers to the wide range of artificially engineered materials, typically synthesized by arranging conductive structures of particular shape and size in a host dielectric medium [1]-[4]. The electromagnetic parameters and geometry of such inclusions are designed to change the response of the host material and obtain special properties that are not achievable by conventional materials at the frequencies of interest. Just to cite an example, though some natural materials (e.g. noble metals and some semiconductors) exhibit unconventional values (i.e. negative or near zero) of the electric permittivity at IR, visible, and UV frequencies [5]-[6], a natural material with similar characteristics in the microwave regime was not known. In the same way, magnetism of natural materials is limited to radio and low-microwave frequencies [7] and, consequently, anomalous permeability values are not naturally available in the IR, visible, and UV domains. When nature does not provide us with the needed values of the material parameters, MTMs can be successfully used to obtain such anomalous values.

For instance, as anticipated in [8] and experimentally demonstrated in [9], it is possible to obtain a MTM characterized by a negative index of refraction at microwave frequencies combining metal thin wires [10] and split-ring resonators (SRRs). In fact, since in such material the inclusions and the distance between them are reduced in size when compared with the operating wavelength, it is possible to introduce effective permittivity, permeability and refractive index of the medium, which can assume anomalous values. Its synthesis starts from the idea introduced by Pendry [9], that a series of electric dipoles properly oriented causes a resonant behavior for the effective electrical permittivity of the medium. Similarly, a set of magnetic dipoles causes a similar resonance of the effective magnetic permeability associated with the MTM. If the two resonances occur at the same frequency range, we are able to synthesize a material with negative refractive index in a specific frequency range.

The key element to the realization of the first MTM was then the SRR, which is a miniaturized resonator useful to obtain artificial magnetism at microwave frequencies.

A single SRR consists of two concentric metallic broken rings with the two gaps placed at the opposite sides of the structure. This ingenious design permits to increase the overall capacitance of the resonator with respect to a single ring structure, by adding a distributed capacitance between the two concentric rings. In this way, the resonant frequency can be significantly lowered to reach an electrical size of the order of $\lambda/10$. After the work [9], several different magnetic inclusions have been introduced to achieve a higher degree of miniaturization, remove the inherent bi-anisotropy characterizing the electromagnetic behavior of the SRR [11]-[14], and obtain an isotropic response [15]-[18].

Besides these modeling efforts, several innovative properties of MTMs have been investigated. In particular, the effect of super-resolution of a MTM with a negative index of refraction has shown how one can overcome the physical limit of diffraction. A conventional lens, in fact, is able to focus on a detail with a well-known limit in optics: fixed the working frequency, this detail can not be less than the corresponding operating wavelength. A flat plate of properly designed MTM can instead ideally go below the physical limit of diffraction, focusing details with dimensions smaller than the wavelength. Other interesting applications of MTMs result from the idea that, if we couple together a pairs of conjugated artificial materials, we can design resonant cavities of transverse dimensions much smaller than the wavelength. Starting from these ideas, several innovative components and devices based on MTMs properties have been proposed, such as super-lenses [19]-[20], hyper-lenses [21], cloaking covers [22]-[24], compact radiating components [25]-[29], enhanced transmission devices [30]-[36], filters [37], absorbers [38], etc. Moreover, in the last years, exploiting the potentials offered by nano-fabrication, the operation frequency range of MTMs has been extended up to optical frequencies [39]-[43]. In this case, however, the magnetic resonators used at microwave frequencies cannot be straightforwardly applied [44], and alternative designs with a lower rate of miniaturization [45]-[46], or based on conceptually different approaches [47]-[48] have been introduced.

Whatever the frequency range of interest is, however, artificial magnetic materials exhibit some intrinsic limitations. Due to energy considerations, in fact, any passive MTM is necessarily a dispersive medium [49], meaning that the desired values of the

electromagnetic parameters are typically reached only in a narrow frequency range and, consequently, the operation bandwidth of MTM-based components is limited. Moreover, as it is clear from Kramers-Kronig causality relationships, the dispersion phenomenon is always related to loss mechanisms [49] that further reduce the potentials of the designed MTMs.

Chapter 1 of this thesis is, thus, dedicated to the investigation on the use of non-Foster active elements to increase the operation bandwidth of a SRR for possible application in MTM-inspired components. First, we design the circuit topology of the active load required to compensate the intrinsic reactance of the SRR and get a broadband response. Then, we show that the same procedure can be successfully applied to the case of a SRR-based monopole antenna and, in principle, to any MTM-inspired device employing SRRs. Finally, integrating an electromagnetic and a circuit simulator, we propose a possible realistic implementation of the active load, based on the employment of commercially available circuit elements. The obtained results (seven times improvement of the impedance bandwidth of the SRR-based monopole antenna) prove that non-Foster active loads can be successfully used to overcome the inherent narrow-band operation of SRR-based passive MTM and MTM-inspired components. The implementation issues related to circuit element dispersion, parasitic effects, and stability of the active circuit are fully considered in the proposed design.

Chapter 2 of this thesis will be devoted, instead, to the design of new compact and multi-functional radiating elements inspired by the concepts of MTMs. First, we present the design and the operation principles of a printed monopole antenna loaded with two identical SRRs. The idea is to use the SRRs not only to miniaturize the antenna dimensions but also to introduce multiple resonances that can be properly selected by using electronic switches placed across the four gaps of the two SRRs. In fact, by properly combining the ON/OFF status of the four switches, it is possible to either change the operation frequency and/or the shape of the radiation pattern of the printed monopole or even add new operation frequencies. Then, we present a compact antenna consisting of two orthogonal meandered monopoles that act as parasitic elements of a driven bow-tie. In particular, we show that by using two monopoles with slightly different dimensions, a greater impedance bandwidth can be obtained. Using this

approach, we present a compact antenna operating in the 2.4 GHz Wi-Fi band with overall dimensions of $\lambda_0/6 \times \lambda_0/12 \times \lambda_0/75$.

In **Chapter 3**, we focus our attention on the design of horn antennas with integrated MTM-inspired filtering module. For this purpose, we first propose the use of electrically small antennas for the design of a new setup to increase power transmission through a sub-wavelength aperture. The proposed setup consists of a circular metallic disk with a sub-wavelength aperture through which two sets of connected circularly polarized electrically small antennas are placed. A linear-to-circular polarization transformer based on this concept is also presented. We show that the proposed structure placed at the end of an open-ended rectangular waveguide is able to change its linear polarization to a circular one. Then, integrating this polarization transformer in a conical horn, we show how it is possible to obtain a circularly polarized filtering horn antenna (horn filtenna). However, this setup is not planar, consists of different and geometrically orthogonal structures, involves the use of dielectric materials leading to an efficiency reduction, and can handle only low-power signals (i.e. the operation is limited to the receiving mode only). In order to overcome these issues, we then propose a new linear-to-circular polarization transformer that consists of a complementary electrically small resonator etched on a metallic screen. We first show that this component is able to transform the linear polarization of a regular rectangular waveguide working on the fundamental mode into a circular one. Then, integrating this polarization transformer in a conical horn, we show how it is possible to obtain a filtering horn antenna working for circularly polarized signals. The numerical simulations and the measurements performed on a prototype prove the effectiveness of the proposed structure.

Please note, however, that this approach involves the insertion of a metallic screen orthogonal to the propagation direction of the electromagnetic field; therefore, it can be used only for microwave components exhibiting a band-pass behavior. In order to design horn filtennas or microwave components with band-stop characteristic, thus, we need to remove the metallic screen and design a proper resonant inclusion that stores/dissipates energy at a given frequency, leading to a band-notch in a narrow frequency range. For this purpose, we then present the design of filtering horn antennas with band-stop characteristics obtained through the use of electrically small magnetic

resonators. In particular, a SRR etched on a Rogers DuroidTM RT5870 dielectric substrate is inserted within the metallic flare of the horn at a proper distance from the throat. At around the resonant frequency of the SRR transmission is highly reduced and a single notched-band is obtained. In order to extend the result to dual-band operation, we also present the design of the filtering module made by two SRRs with different dimensions. The validity of the proposed approach is verified through proper sets of full-wave simulations and experiments on fabricated prototypes.

In the previous chapters we have considered all radiating structures; on the contrary, in **Chapter 4** we deal with the project of novel microwave components. In particular, the planar polarization transformer presented in the previous chapter will be used for designing a new class of waveguide components. We first show a rectangular-to-circular waveguide transition that allows to effectively match waveguides with different cross-sections and to transform the linearly polarized TE₁₀-mode of a rectangular waveguide into a circularly polarized TE₁₁-mode of a circular waveguide. Next, using similar structures, we present the design and the numerical results of two power dividers and of an orthomode transducer. All these components, employing only thin metallic sheets with properly shaped slits, can be integrated in waveguide transmission systems without increasing their space occupancy. As another example of microwave component inspired to the concept of MTM, we then propose a novel and low-cost MTM-inspired absorber operating in X-band. It consists of a single resistive sheet properly spaced from a double-ring based metasurface. Its operation principle is similar to the one of a Salisbury screen, in which a 377 Ω/sq resistive sheet is placed $\lambda/4$ apart from a metal plate. In our configuration, however, the metasurface replaces the metallic backing significantly reducing the used percentage of metal. This is very convenient when the absorber is used to reduce the radar cross section (RCS) of non-metallic objects. In this scenario, the absence of a metal ground plane allows a significant weight reduction and a smaller increase of the object RCS outside the operating band of the absorber. The performances of both the metasurface and the absorber have been evaluated through numerical full-wave simulations and measurements on a fabricated prototype. These results confirm the effectiveness of the proposed configuration, which properly work within the entire X-band.

All the aforementioned components are inspired to the concept of MTM and allow performing different operations on the electromagnetic signal such as band-pass or notch filtering and polarization transformation. Since most of them are made of a single MTM-inspired particle, these components can be easily integrated into the radiating element, performing the signal manipulation directly on the transmitted or received electromagnetic signal. Another possible manipulation that may be performed on an electromagnetic signal is the generation of orbital angular momentum (OAM). In particular, the recent extension of the OAM concept from optical to microwave frequencies has led some researchers to explore how well established antenna techniques can be used to radiate a non-zero OAM electromagnetic field. In this frame, **Chapter 5** is aimed to present a new approach to generate a non-zero OAM field through a single patch antenna. Using the cavity model, we first analyze the radiated field by a standard circular patch and show that a circular polarized (CP) TM_{nm} mode excited by using two coaxial cables generates an electromagnetic field with an OAM of order $\pm(n-1)$. Then, in order to obtain a simpler structure with a single feed, we design an elliptical patch antenna working on the right-handed CP TM_{21} mode. Using full-wave simulations and experiments on a fabricated prototype, we show that the proposed antenna effectively radiates an electromagnetic field with a first order OAM. Such results prove that properly designed patch antennas can be used as compact and low-cost generators of electromagnetic fields carrying OAM.

References

- [50] G.V. Eleftheriades, and K.G. Balmain, *Negative Refraction Metamaterials: Fundamental Principles and Applications*. Hoboken, NJ: Wiley-IEEE Press, 2005.
- [51] N. Engheta, and R.W. Ziolkowski, *Electromagnetic Metamaterials: Physics and Engineering Explorations*. Hoboken, NJ: Wiley-IEEE Press, 2006.
- [52] R. Marqués, F. Martín, M. Sorolla, and F. Capolino, *Metamaterials with Negative Parameters: Theory, Design and Microwave Applications*. Hoboken, NJ: Wiley-Interscience, 2008.
- [53] S. Zouhdi, A. Sihvola, and A. P. Vinogradov, *Metamaterials and Plasmonics: Fundamentals, Modelling, Applications*. Dordrecht, NL: Springer-Verlag GmbH, 2008.

- [54] P.B. Johnson, R. W. Christy, "Optical constants of the noble metals," *Phys. Rev. B*, Vol. 6, pp. 4370-4379, 1972.
- [55] E.D. Palik, *Handbook of Optical Constants of Solids*, Boston, NE: Academic Press, 1998.
- [56] L.D. Landau, L.P. Pitaevskii, and E.M. Lifshitz, *Electrodynamics of Continuous Media, Second Edition: Volume 8*. Oxford, EN: Pergamon Press, 1984.
- [57] V.G. Veselago, "The electrodynamics of substances with simultaneously negative values of ϵ and μ ," *Sov. Phys. Uspekhi*, Vol. 10, pp. 509–514, 1968.
- [58] D.R. Smith, W.J. Padilla, D.C. Vier, S.C. Nemat-Nasser, and S. Schultz, "Composite medium with simultaneously negative permeability and permittivity," *Phys. Rev. Lett.*, Vol. 84, pp. 4184-4187, 2000.
- [59] W. Rotman, "Plasma simulation by artificial dielectrics and parallel-plate media," *IRE Trans. Antennas Propagat.*, Vol. 10, pp. 82-25, 1962.
- [60] R. Marqués, F. Medinaand, and R. Rafii-El-Idrissi, "Role of bi-anisotropy in negative permeability and left handed metamaterials," *Phys. Rev. B*, Vol. 65, 144441, 2002.
- [61] R. Marqués, F. Mesa, J. Martel, and F. Medina, "Comparative analysis of edge and broadside coupled split ring resonators for metamaterial design. Theory and experiment," *IEEE Trans. Antennas Propagat.*, Vol. 51, pp. 2572–2581, 2003.
- [62] R. Marqués, J. D. Baena, J. Martel, F. Medina, F. Falcone, M. Sorolla, and F. Martin, "Novel small resonant electromagnetic particles for metamaterial and filter design," *Proc. ICEAA '03*, pp. 439–442, Torino, Italy, 2003.
- [63] J. D. Baena. R. Marqués, F. Medina, and J. Martel, "Artificial magnetic metamaterial design by using spiral resonators," *Phys. Rev. B*, Vol. 69, 014402, 2004.
- [64] Ph. Gay-Balmaz, and O. J. F. Martin, "Efficient isotropic magnetic resonator," *Appl. Phys. Lett.*, Vol. 81, pp. 939–941, 2002.
- [65] C. R. Simovski, and B. Sauviac, "Towards creating isotropic microwave composites with negative refraction," *Radio Sci.*, Vol. 39, RS2014, 2004.
- [66] C. R. Simovski, and S. He, "Frequency range and explicit expressions for negative permittivity and permeability for an isotropic medium formed by a lattice of perfectly conducting Ω particles," *Phys. Lett. A*, Vol. 311, pp. 254–263, 2003.
- [67] M.M. I. Saadoun, and N. Engheta "A reciprocal phase shifter using a novel pseudochiral or Ω medium," *Microwave Opt. Tech. Lett.*, Vol. 5, pp. 184–188, April 1992.
- [68] J.B. Pendry, "Negative refraction makes a perfect lens," *Phys. Rev. Lett.*, Vol. 85, pp. 3966-3969, 2000.
- [69] P. Belov, R. Marques, S. Maslovski, I. Nefedov, M. Silverinha, C. Simovski, and S. Tretyakov, "Experimental study of the subwavelength imaging by a wire medium slab," *Phys. Rev. B*, Vol. 67, 113103, 2003.

- [70] W. Zhang, H. Chen, and H.O. Moser, "Subwavelength imaging in a cylindrical hyperlens based on S-string resonators," *Appl. Phys. Lett.*, Vol. 98, 073501, 2011.
- [71] A. Alù and N. Engheta, "Achieving transparency with plasmonic and metamaterial coatings," *Phys. Rev. E*, Vol. 72, 016623, 2005.
- [72] M. G. Silveirinha, A. Alu, and N. Engheta, "Parallel-plate metamaterials for cloaking structures," *Phys. Rev. E*, Vol. 75, 036603, 2007.
- [73] B. Edwards, A. Alu, M. Silveirinha, and N. Engheta, "Experimental verification of plasmonic cloaking at microwave frequencies with metamaterials," *Phys. Rev. Lett.*, Vol. 103, 153901, 2009.
- [74] R.W. Ziolkowski and A.D. Kipple, "Application of double negative materials to increase the power radiated by electrically small antennas," *IEEE Trans. Antennas Propagat.*, Vol. 52, pp. 2626-2640, 2003.
- [75] F. Qureshi, M.A. Antoniades, and G. V. Eleftheriades, "A compact and low-profile metamaterial ring antenna with vertical polarization," *IEEE Antennas Wireless Propag. Lett.*, Vol. 4, pp. 333-336, 2005.
- [76] A. Alù, F. Bilotti, N. Engheta, and L. Vegni, "Sub-wavelength planar leaky-wave components with metamaterial bilayers," *IEEE Trans. Antennas Propagat.*, Vol. 55, pp. 882-891, 2007.
- [77] A. Alù, F. Bilotti, N. Engheta, and L. Vegni, "Subwavelength, Compact, Resonant Patch Antennas Loaded With Metamaterials," *IEEE Trans. Antennas Propagat.*, Vol. 55, pp. 13-15, 2007.
- [78] F. Bilotti, A. Alù, and L. Vegni, "Design of miniaturized metamaterial patch antennas with μ -negative loading," *IEEE Trans. Antennas Propagat.*, Vol. 56, pp. 1640-1647, 2008.
- [79] D. E. Grupp, H. J. Lezec, T. Thio, and T. W. Ebbesen, "Beyond the Bethe limit: tunable enhanced light transmission through a single sub-wavelength aperture," *Adv. Mat.*, Vol. 11, pp. 860-862, 1999.
- [80] A. Alù, F. Bilotti, N. Engheta, and L. Vegni, "Metamaterial covers over a small aperture," *IEEE Trans. Antennas Propagat.*, Vol. 54, pp. 1632-1643, 2006.
- [81] A. Alù, F. Bilotti, N. Engheta, and L. Vegni, "A review on the potential use of metamaterial layers for increasing the transmission through a single sub-wavelength aperture in a flat opaque screen," in *Periodic Structures*, ed. by M. Bozzi and L. Perregrini, Kerala, India, 2006, ch. 10, pp. 271-291.
- [82] F. Bilotti, L. Scorrano, E. Ozbay, and L. Vegni, "Enhanced transmission through a sub-wavelength aperture: Resonant approaches employing metamaterials," *J. Opt. A*, Vol.11, 114029, 2009
- [83] K. Aydin, A.O. Cakmak, L. Sahin, Z. Li, F. Bilotti, L. Vegni, and E. Ozbay, "Split-ring-resonator-coupled enhanced transmission through a single subwavelength aperture," *Phys. Rev. Lett.*, Vol. 102, pp. 013904, 2009.

- [84] K.B. Alici, F. Bilotti, L. Vegni, and E. Ozbay, "Optimization and tunability of deep subwavelength resonators for metamaterial applications: complete enhanced transmission through a subwavelength aperture," *Opt. Expr.*, Vol. 17, pp. 5933-5943, 2009.
- [85] A.O. Cakmak, K. Aydin, E. Colak, Z. Li, F. Bilotti, L. Vegni, and E. Ozbay, "Enhanced transmission through a sub-wavelength aperture using metamaterials," *Appl. Phys. Lett.*, Vol. 95, 052103, 2009.
- [86] J. Martel, R. Marques, F. Falcone, J.D. Baena, F. Medina, F. Martin, and M. Sorolla, "A new LC series element for compact bandpass filter design," *IEEE Microwave Wireless Compon. Lett.*, Vol. 14, pp. 210-212, 2004.
- [87] F. Bilotti, L. Nucci, and L. Vegni, "An SRR based microwave absorber," *Microw. Opt. Technol. Lett.*, Vol. 48, pp. 2171-2175, 2006.
- [88] N. Fang, H. Lee, C. Sun, and X. Zhang, "Sub-diffraction-limited optical imaging with a silver superlens," *Sci.*, Vol. 308, pp. 534-537, 2005.
- [89] A. Salandrino, and N. Engheta, "Far-field subdiffraction optical microscopy using metamaterial crystals: Theory and simulations," *Phys. Rev. B*, Vol. 74, 075103, 2006.
- [90] Z. Liu, H. Lee, Y. Xiong, C. Sun, and X. Zhang, "Far-field optical hyperlens magnify-ing sub-diffraction-limited objects," *Sci.*, Vol. 315, pp. 1686, 2007.
- [91] M. Silveirinha, A. Alu and N. Engheta, "Infrared and optical invisibility cloak with plasmonic implants based on scattering cancellation," *Phys. Rev. B*, 78, 075107, 2008.
- [92] N. Engheta, "Circuits with light at nanoscales: Optical nanocircuits inspired by metamaterials," *Sci.*, Vol. 317, pp. 1698-1702, 2007.
- [93] J. Zhou, T. Koschny, M. Kafesaki, E.N. Economou, J.B. Pendry, and C.M. Soukoulis, "Saturation of the magnetic response of split-ring resonators at optical frequencies," *Phys. Rev. Lett.*, Vol. 95, 223902, 2005.
- [94] G. Dolling, C. Enkrich, M. Wegener, J. F. Zhou, C. M. Soukoulis, and S. Linden, "Cut-wire pairs and plate pairs as magnetic atoms for optical metamaterials," *Opt. Expr.*, Vol. 30, pp. 3198-3200, 2005.
- [95] M. Kafesaki, I. Tsiapa, N. Katsarakis, Th. Koschny, C. M. Soukoulis, and E. N. Economou, "Left-handed metamaterials: The fishnet structure and its variations," *Phys. Rev. B*, Vol. 75, 235114, 2007.
- [96] A.N. Grigorenko, A.K. Geim, H.F. Gleeson, Y. Zhang, A.A. Firsov, I.Y. Khrushchev, J. Petrovic, "Nanofabricated media with negative permeability at visible frequencies," *Nat.*, Vol. 438, pp. 335-338, 2005.
- [97] A. Alù, and N. Engheta, "The quest for magnetic plasmons at optical frequencies," *Opt. Expr.*, Vol. 17, pp. 5723-5730, 2009.

- [98] S.A. Tretyakov, and S.I. Maslovski, "Veselago materials: What is possible and impossible about the dispersion of the constitutive parameters," *IEEE Antennas Propag. Mag.*, Vol. 49, pp. 37-43, 2007.

Chapter 1

Non-Foster actively loaded SRR and application in metamaterial-inspired components

As shown in [1], it is in principle possible to widen the operation bandwidth of a passive MTM by loading it with an active circuit. In particular, in [1] a short dipole (or a small loop) antenna loaded with an ideal two-port electronic circuit has been considered and it has been shown that, in order to get negative and frequency-independent values of the permittivity (or permeability), it is necessary to use a negative capacitance (or inductance). In [1] it has been also suggested that this kind of reactive elements can be obtained using negative impedance converters (NICs), i.e. two-port devices exhibiting at the input port an impedance that is the opposite of the load one [2].

This class of active circuits, violating Foster's theorem [3], has been introduced in the last century to compensate resistive losses [4] and their first transistor-based implementations are due to Linvill [5]. Recently, due to their unique and interesting properties, NIC circuits have been extensively applied to widen the operational bandwidth of electromagnetic components. For instance, as far as antennas are concerned, NICs have been used to design active external matching networks for both microstrip [6] and electrically small dipole/monopole/loop antennas [7]-[9] able to overcome Bode-Fano criterion, while a different conceptual approach, based on internal non-Foster matching circuits, has been proposed in [10]-[11]. Moreover, NICs have been used to synthesize ultra-wideband artificial magnetic conductors (AMCs) and electromagnetic band gap structures [12] and superluminal waveguides for broadband leaky-wave antennas [13]-[14].

In the last few years, some groups have focused their efforts to investigate the possibility of using NICs to overcome the limitations of passive MTMs. In particular, non-Foster elements have been used to increase the bandwidth of several types of broadband and electrically small MTM-inspired antennas [15]-[18] and to obtain an almost dispersionless epsilon-near-zero MTM, useful for cloaking applications [19]-[20]. Finally, in [21] an active broadband effective MTM has been proposed.

It is important to observe that, despite the potentials of such NIC circuits, their practical use is still limited, due to the fact that the design and the proper use of a NIC is not a trivial task. One of the main issues concerns the theoretical evaluation of the NIC stability and the related technological aspects. As clarified in [22], where several circuits including negative lumped elements have been investigated, in fact, the correct evaluation of the stability depends also on the used evaluation approach and the uncritical use of classical stability methods may result in assessment mistakes.

In this Chapter, inspired by the aforementioned papers, we propose to load a SRR with a proper NIC-based active circuit, in order to increase its operation bandwidth and make it useful for the application in broadband MTM-inspired components. In order to show the potentials of the proposed broadband SRR, we analyze the performance improvement of the SRR-based antenna presented in [23], suitably scaled to work within the RF band, where NIC implementation is not critical by using discrete circuit elements.

The Chapter is organized as follows: in Section 1, we analytically determine the ideal load topology required to widen the bandwidth of an individual SRR. In Section 2, we describe a numerical full-wave procedure to determine the negative ideal values of the load circuit elements required to achieve the broadband effects. In Section 3, we apply the described procedure to the design of the SRR-based antenna proposed in [23], whose performance is strongly limited by the narrowband operation. In Section 4, we propose a possible realistic circuit implementation of the required active load for the SRR-based antenna using a proper transistorized network, including only commercially available elements. Finally, in Section 5, we deal with the stability issues of the overall system. In particular, we first develop an analytical study of the stability conditions in the idealized case and, then, show a transient simulation of the signal in the actual

designed antenna system, in order to show that it remains bounded for a bounded excitation signal (i.e. the system is stable).

1.1 Analytical Determination of the Ideal Load

Magnetic MTMs at microwave frequencies are typically realized with metallic resonant inclusions embedded in a host material. The most common inclusion used to obtain a magnetic response is the SRR. A squared SRR consists of two concentric metallic rings with gaps at two opposite sides (Fig. 1(a)). Due to the electrically small dimensions of the structure, it is possible to study its electromagnetic behaviour using a quasi-static approach. Following this concept, a possible and quite accurate model of the SRR is given by an equivalent LC lumped circuit. The angular resonant frequency of the SRR, thus, can be expressed as:

$$\omega_0 = \frac{1}{\sqrt{LC}}, \quad (1)$$

where L and C are related to the geometrical dimensions of the SRR [24]. By definition, at the resonant frequency of the LC parallel circuit susceptance is zero. However, due to the high electromagnetic energy storage in proximity of the resonator, susceptance remains close to zero only in a very narrow frequency range around ω_0 . The consequence of this phenomenon is the strong dispersive behaviour of the SRR, resulting in its narrow operation bandwidth.

On the basis of this consideration, it is easy to understand that a simple way to broaden the bandwidth of the SRR is to compensate its intrinsic susceptance by loading the inclusion with a proper circuit, whose susceptance is, for each frequency, the opposite of the SRR one. In this way, the overall susceptance of the loaded SRR becomes zero in a large frequency range around the resonant frequency.

In order to determine the load impedance required to satisfy the previous condition, we have theoretically loaded the SRR with an ideal impedance Z_L . Clearly, the circuit design depends on where the non-Foster load is placed. For the sake of simplicity, we have decided to place it across the gap of the external ring (see Fig. 1(a)). In circuitual

terms, such physical connection corresponds to connect the ideal load in parallel to the LC equivalent circuit modeling the SRR (Fig. 1(b)). Under these assumptions, the overall admittance of the loaded resonator can be written as:

$$Y_{tot} = -j \frac{Z_L + j\omega L - \omega^2 LC Z_L}{\omega L Z_L}. \quad (2)$$

Imposing the cancellation of Y_{tot} , from (2) we obtain:

$$Z_L = j \frac{\omega L}{\omega^2 LC - 1}, \quad (3)$$

that can be expressed in admittance form as:

$$Y_L = -j \frac{\omega^2 LC - 1}{\omega L} = -j\omega C + j \frac{1}{\omega L}. \quad (4)$$

Thus, the ideal load to be used to compensate the SRR reactance is a parallel combination of a negative inductance and a negative capacitance, whose values are equal, but opposite, to those of the lumped equivalent circuit of the SRR.

Unfortunately, a circuit with such features cannot be a passive one [1]. In fact, negative reactive elements exhibit a negative slope of the reactance versus frequency, violating Foster's theorem [3].

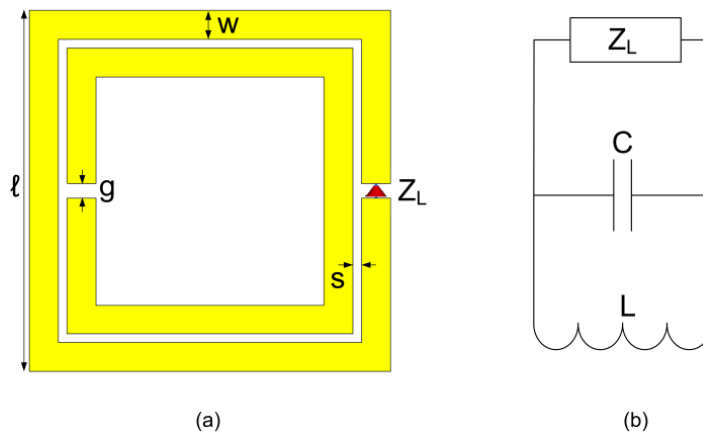


Fig. 1: (a) Geometry of a SRR loaded with an arbitrary impedance Z_L and (b) its lumped element equivalent circuit representation.

1.2 Broadband Active SRR: Design Principles

As a first approximation, one can estimate the values of L and C from the geometry of the SRR. In the open technical literature, there are several analytical expressions (see, for instance, [24]-[25]) that allow deriving the values of L and C (and, then, of the resonant frequency of the resonator) from the SRR geometry. However, after a first set of simulations, we noticed that the desired bandwidth enhancement effect is rather sensitive to the circuitual values of the load, and that better results can be obtained determining the required L and C values through full-wave numerical simulations.

For this purpose, we have simulated the behaviour of a rectangular SRR employing CST Microwave Studio [26], a full-wave commercial software based on the finite integration technique. The simulated structure consists of a two-port ideal waveguide with a SRR placed in its centre. The waveguide walls have been realized using perfect electric conductor (PEC) and perfect magnetic conductor (PMC) boundary conditions, so that the SRR is excited by a TEM mode, whose magnetic field is parallel to the axis of the SRR. Since the simulation setup allows the propagation of a TEM mode with a zero cut-off frequency, the waveguide sizes can be chosen very large compared to the operational wavelength. In this way, it is possible to neglect the mutual coupling between adjacent SRRs arising from the mirror symmetry of the simulated structure. The magnitude of the S_{11} parameter in the case of an unloaded SRR with geometric dimensions (in mm) $\ell = 5$, $g = 0.2$, $w = 0.4$, $s = 0.12$, is shown in Fig. 2 (solid line). As expected, in a narrow frequency band around the resonant frequency of the SRR most of the incoming signal is reflected back at the input port.

In order to obtain the loading element values to compensate the intrinsic reactance of the SRR and improve the bandwidth performance, we have followed the procedure described in [10] and [15]. In CST Microwave Studio, the SRR has been loaded with a discrete port placed in the gap of its external ring. The gap can be replaced by an arbitrary circuit (in our case a simple test capacitance C_{test}) designed in CST Design Studio, that is a schematic design tool directly interfaced to CST Microwave Studio. By changing the test capacitance value, the SRR resonates at different frequencies, as shown in Fig. 3. Please note that the same plot could be obtained by adding a lumped

element in the gap of the SRR and performing a parametric sweep in CST Microwave Studio with respect to the capacitance value. With our method, however, after the first full-wave microwave analysis, it is possible to realize the same sweep directly in CST Design Studio that, being a circuital tool, allows a dramatic simulation time saving.

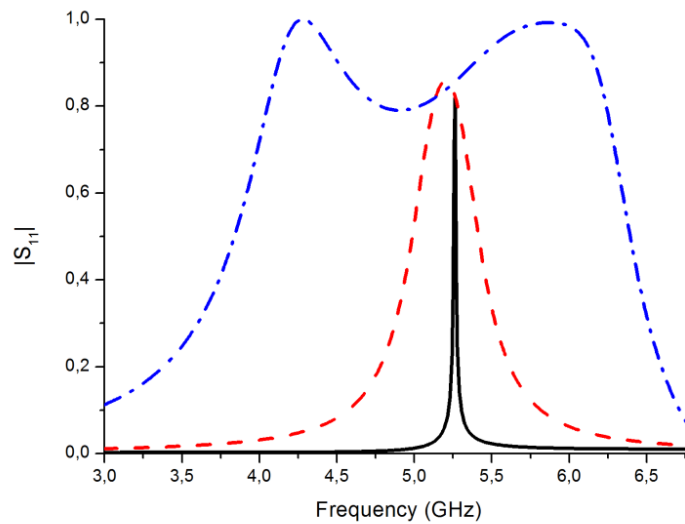


Fig. 2: Magnitude of the S_{11} parameter of the unloaded SRR case (solid line), of the SRR loaded with a LC tank circuit (dashed line), and of the SRR loaded with a LC tank circuit in series with an inductance (dot-dashed line).

If we plot the values of the loading reactance as a function of the corresponding resonant frequencies (triangular symbols in Fig. 4), it is possible to retrieve point-by-point the non-Foster reactance compensating the intrinsic reactance of the SRR. In fact, if the reactance curve of the loading circuit passes through the points that describe the relationship between the SRR resonant frequency and the corresponding test loading capacitance, the SRR resonates over a wide frequency band. Assuming to load the SRR with a LC tank circuit (see the conclusions of the analytical analysis reported in the previous Section) and imposing that the analytical reactance of the loading circuit fits the required one in two points symmetric with respect to the resonant frequency of the unloaded SRR ($f_1 = 5.24$ GHz and $f_2 = 5.28$ GHz), the values of the non-Foster elements, L_t and C_t , can be easily derived solving a 2×2 algebraic linear system. In particular, we have obtained:

$$\begin{aligned} L_t &= -7.3 \text{ nH} \\ C_t &= -0.125 \text{ pF} \end{aligned} \quad (5)$$

Using these values, the curve of the reactive load well approximates the desired shape, as shown in Fig. 4 (dashed line). Moreover, as expected, the loaded SRR exhibits a wider bandwidth than the one of the unloaded SRR (see Fig. 2 - dashed line). Please note that the two frequency points used to determine (5) are chosen in close proximity of the resonance frequency in order to maximize the bandwidth enhancement effect. The simulations conducted revealed, in fact, that, when f_1 and f_2 are more far apart, a better overlap between the realized and the desired reactance curves is obtained around the selected points, resulting in a worse approximation around the resonant frequency. The described effect resulted in an unwanted split of the widened -10 dB bandwidth of the SRR in two narrower symmetric bands. Please note that the obtained bandwidth is, however, significantly larger than the range $f_2 - f_1$, as it is clear from Fig. 2.

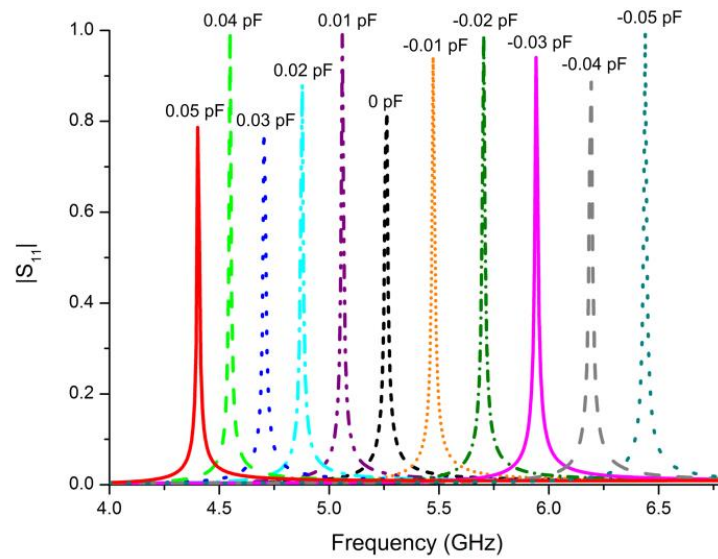


Fig. 3: Magnitude of the S_{11} parameter of a waveguide with a SRR loaded with different test capacitances (values in the range -0.05 - 0.05 pF).

Using a more complex load circuit consisting of a LC tank circuit in series with an inductor, it is possible to obtain a better approximation of the desired reactive curve in a

wider range of frequencies, without worsening the approximation around the resonance frequency, as shown in Fig. 4 (solid line). In particular, we have further increased the SRR bandwidth (Fig. 2, dot-dashed line) using the following values:

$$\begin{aligned} L_t &= -7.18nH \\ C_t &= -0.127pF \\ L_s &= -2.12nH \end{aligned} \quad (6)$$

Moreover, better and better approximations could be obtained by using rigorous impedance synthesis methods, based on cascades of reactive loads.

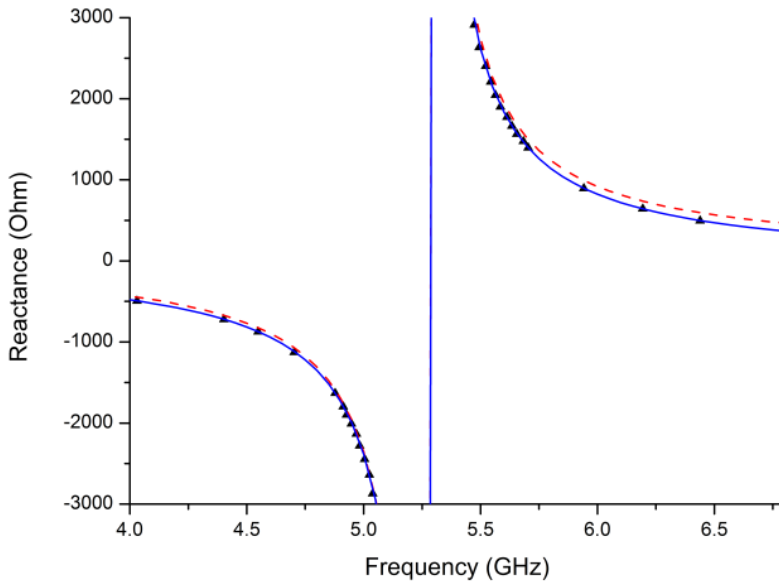


Fig. 4: Reactance of the loading capacitance as a function of the corresponding resonant frequency (triangular symbols), reactance of the LC tank non-Foster circuit (values in (5) have been used) (dashed line), and non-Foster reactance of a LC tank circuit in series with an inductor (values in (5) have been used) (solid line).

This result suggests that the equivalent circuit of the SRR, commonly used to predict its resonant frequency, might not be able to describe with the required accuracy the behaviour of the SRR in a wide range of frequencies. Therefore, as far as non-Foster broadband MTM applications are concerned, a SRR model that is accurate in a wider range of frequency, would be desirable to derive alternative active circuit topologies

able to further increase the loaded SRR bandwidth. However, the derivation of such a more accurate equivalent circuit is out of our scope and, in order to prove the concept of demonstrating a SRR operating over a broad frequency range, we will make use in the following of the regular LC tank circuit representation.

1.3 Broadband SRR-Based Monopole Antenna

The design principles exposed in the previous Sections can be used in any MTM-based application involving a magnetic resonator. In fact, once the equivalent circuit model of the chosen resonator is known, the extension of the aforementioned design principles to the specific application is a straightforward task.

As an example, we consider here the MTM-inspired SRR-based monopole antenna proposed in [23] and shown in Fig. 5. Please note that, due to the implementation issues discussed in the next Section, the structure reported here is scaled compared to the original one, in order to operate within the VHF band. This antenna consists of an electrically short monopole placed in close proximity of a SRR. The SRR is designed to resonate at a much lower frequency compared to the resonant frequency of the monopole and is excited through the near-field coupling with the monopole antenna. As shown in [23], thus, such an antenna operates at the resonant frequency of the SRR, radiating with a reasonable efficiency.

Since, as expected [23], the operation of this antenna is limited by the narrowband behavior of the SRR, it represents a proper example to demonstrate the usefulness of the approach proposed in this Chapter to improve the bandwidth performance.

Following step-by-step the design procedure outlined in the previous Sections, we have determined the required circuitual values of the non-Foster LC load circuit necessary to obtain a broadband antenna behaviour: $L_t = 284.3$ nH, $C_t = -8.93$ pF.

The magnitudes of the S_{11} parameter of the antenna in the unloaded and loaded cases are reported in Fig. 6. Such numerical results confirm the effectiveness of the design, leading to a magnitude of the S_{11} parameter better than -10 dB within the frequency range 90-113.5 MHz and resulting in a bandwidth of operation more than 17 times larger than the one of the scaled SRR-based antenna (99.25-100.57 MHz).

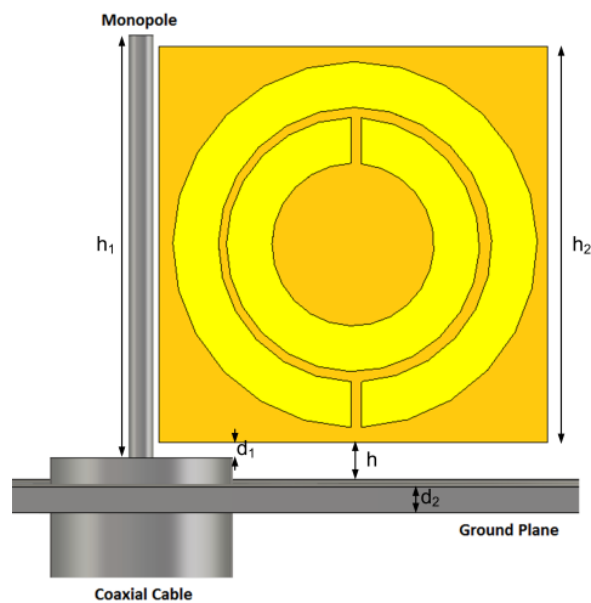


Fig. 5: Geometrical sketch of the SRR-based antenna proposed in [23]. Antenna dimensions in cm: $h = 3.00$, $h_1 = 31.60$, $h_2 = 29.64$, $d_1 = 1.14$, $d_2 = 1.90$. SRR dimensions in cm: $w = 3.42$, $R = 13.70$, $g = 0.76$, $s = 0.76$. Slab (FR-4): $\epsilon_r = 3.5$, $\tan\delta = 0.025$, thickness: 6.08 mm.

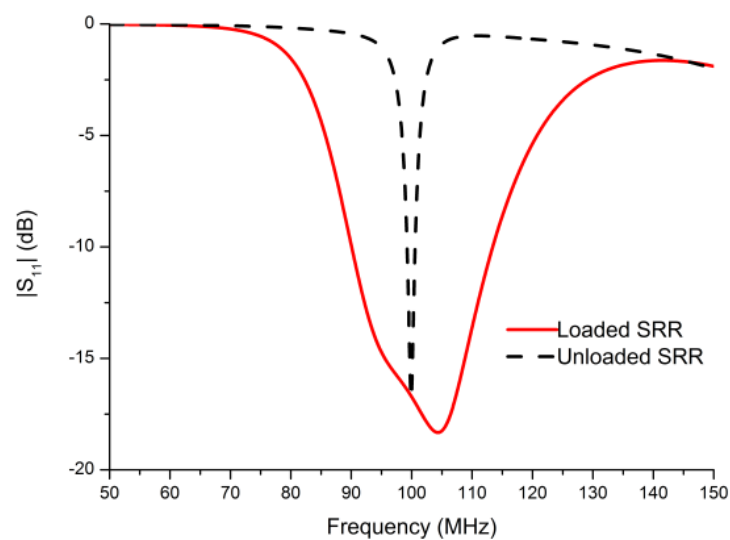


Fig. 6: Magnitude of the S_{11} parameter of the unloaded (dashed line) and loaded (solid line) antenna.

1.4 Implementation Issues

As shown in the previous Section, the ideal non-Foster circuit designed to broaden the operation bandwidth consists of a parallel combination of a negative capacitance and a negative inductance. As previously anticipated, such negative lumped elements can be implemented with the aid of NICs [2]. A NIC is a four-pole active circuit exhibiting a 180° phase shift between its input and output ports: this peculiar behaviour allows obtaining at the input port an impedance (admittance) that is the opposite to the one used to load the output port.

NICs can be realized using different active devices, such as operational amplifiers or transistors [9]. Though a straightforward choice would involve the use of op-amps, we should consider that the highest operation frequency is limited by the transit frequency of the used active elements [19] and, thus, proper operation of the circuit at VHF or higher frequencies is typically achieved by using transistors.

The design of a transistor-based NIC is not a straightforward task and special care to some critical aspects is needed. First of all, transistor technology (BJT, FET, etc.) and complexity of the polarization network represent key elements to determine appropriateness, performance, implementation easiness, and costs of the active circuit. Then, the response of the impedance converter must be checked against the sensitivity to the variation of the nominal values of the lumped elements used in the polarization networks and as loads, due to both frequency dispersion and parasitic effects. Finally, the potential instability of the whole circuit (i.e. the combination of the loaded SRR and the antenna in our case) is a crucial issue, which should be properly considered at the design stage.

Before considering the cited issues one by one, we need first to choose the most appropriate NIC configuration. In the open technical literature, different circuit topologies have been proposed to obtain the required phase inversion (see [27] for some examples). In order to test their performances, we have used a circuitual software (Advanced Design System – ADS), equipped with an extensive library of commercial elements. After having performed a number of simulations and comparisons, we have decided to adopt the circuit topology presented in [28], originally proposed to realize a

negative capacitance and increase the tuning range of a varactor diode. In this configuration (see either of the circuits reported in Fig. 7), the two common-gate transistors of the ideal NIC scheme are powered by two current generators in cascode configuration. The reason of this choice resides in the high performance in terms of stability compared to the other configurations. The proposed topology, in fact, allows separating the input port from the output one, giving, thus, better performance in terms of Miller effect reduction and stability. On the other hand, this choice involves the use of more transistors (additional noise and higher costs are expected) and requires a higher DC voltage compared to regular configurations not involving cascode feeding.

In the following, we describe the design procedure we have adopted to optimize the performance of the circuit to properly work in the case of the SRR-based monopole antenna described in the previous Section. However, we remark here that the design procedure can be easily applied to any other device involving similar actively loaded SRRs.

First of all, we have exported into an s2p file the simulated (CST Microwave Studio has been used) S-parameters of a two-port dummy box placed across the gap of the external ring of the SRR excited by the monopole antenna. This file has been used to characterize the behaviour of the antenna within the circuital software. Basically, we replaced the discrete port located in the external gap of the SRR with the parallel connection of the NIC circuits giving the negative capacitance and the negative inductance. Please note that the circuit implementing the negative capacitance has been used in the form proposed in [28], while the negative inductance implementation required slight modifications, as reported in Fig. 7.

The first step to implement the NIC was the choice of a proper transistor. In the end, we have adopted the TSB JS8910AS, whose data sheets are present in the software library. Then, we have designed the polarization networks for the two branches of the circuit and optimized the overall circuit to produce the best bandwidth performance in terms of the antenna S_{11} parameter. The results, reported in Fig. 8 (dotted line), show a considerable widening of the -10 dB bandwidth, that is only slightly reduced if compared to the one obtained in the ideal case (i.e. ideal negative lumped load).

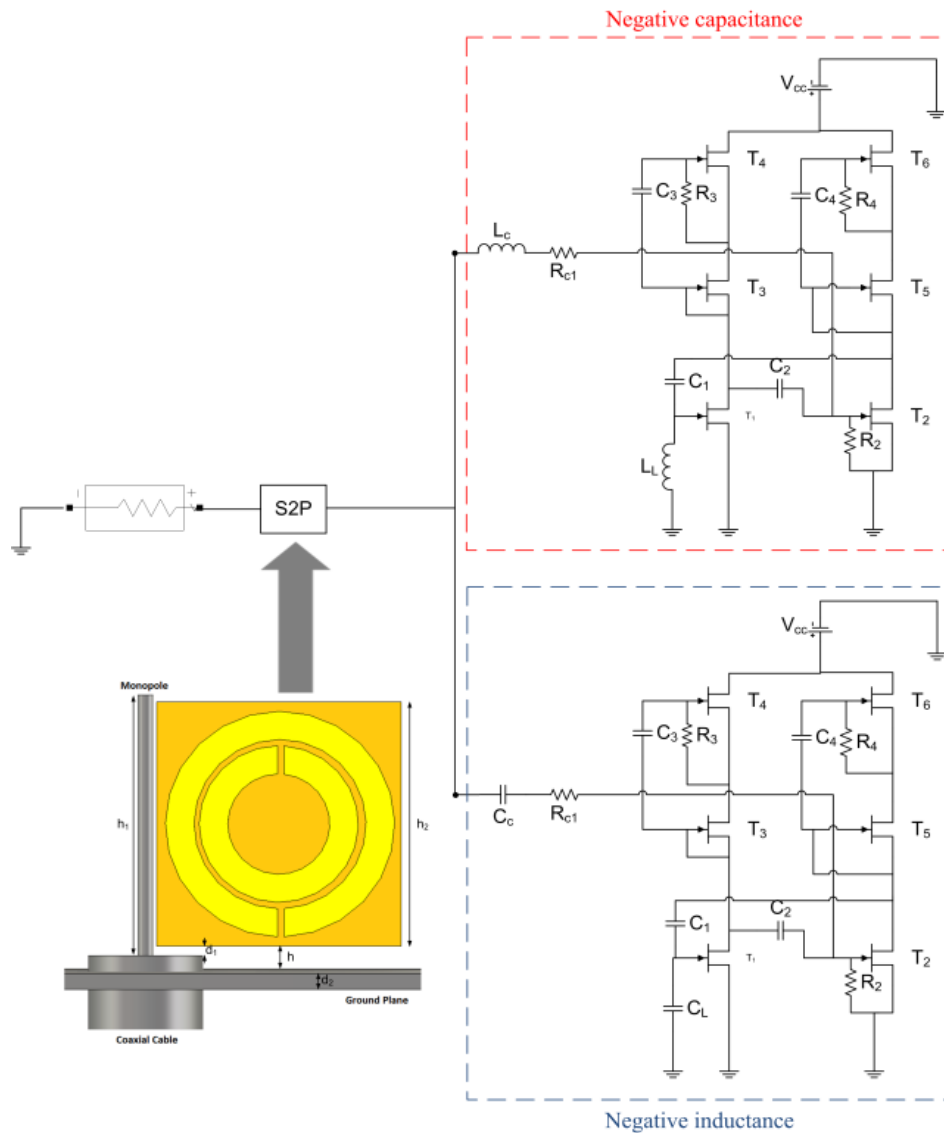


Fig. 7: SRR-based monopole antenna loaded with a parallel connection of two NIC circuits.

In this design step we have used real circuitual transistor models but ideal lumped elements (i.e. resistances, capacitances, and inductances). However, to consider a more realistic implementation, it is necessary to replace ideal elements with the corresponding real ones available in the software library with the same nominal values. Unfortunately, this procedure produces a dramatic deterioration of the antenna performance, because of the circuit sensitivity to the parasitic and frequency dispersive effects that always afflict real lumped elements.

In order to overcome this issue, as a second approach, we have performed a discrete optimization in which the whole set of ideal lumped elements has been replaced by the commercial ones contained in the software library. After this optimization, the results are the ones shown in Fig. 8 (dot-dashed line), exhibiting a significant reduction of the performance with respect to the ideal load case. Nevertheless, we have obtained a significant widening of the bandwidth of about 7 times with respect to the unloaded antenna. The corresponding nominal values of all the real lumped elements are reported in Table I.

Please note that, in the circuit simulator, all the components are modeled with a very accurate equivalent circuit (depending on the manufacturers and on the series) that take into account the parasitic effects and the frequency dispersion of the lumped values. Moreover, a probability density function is associated to each component to take into consideration the corresponding tolerance available from the manufacturer. In all cases, the chosen density function is the uniform one that is conservative compared to the true Gaussian distribution of the manufacturing process. For these reasons, the simulated results can be considered robust against all the critical issues that arise in the realization of a real circuit.

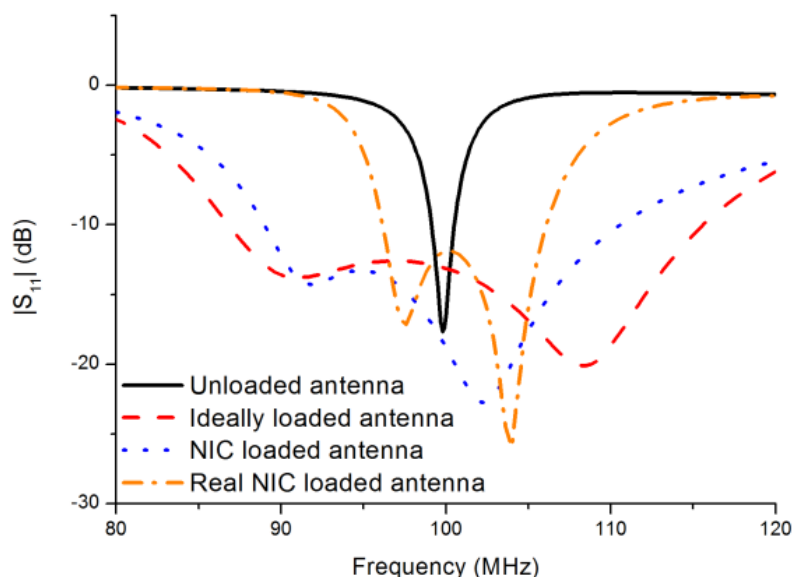


Fig. 8: Magnitude of the S_{11} parameter of the unloaded (solid line), ideally loaded (dashed line), NIC loaded (dotted line), and real NIC loaded (dot-dashed line) antenna.

Table 1: Nominal values of the real lumped elements of the circuit shown in Fig. 8.

Element	Nominal Value (Negative Capacitance Circuit)	Nominal Value (Negative Inductance Circuit)
R_{c1}		787 Ω
R_2	3.16 k Ω	453 Ω
R_3	309 Ω	71.5 Ω
R_4	3.4 k Ω	2.37 k Ω
C_1	13 pF	0.5 pF
C_2	24 pF	1.6 pF
C_3	270 pF	1.2 pF
C_4	24 pF	27 pF
C_c		6.2 pF
C_L		130 pF
L_c	1.8 nH	
L_L	2 nH	

For the sake of completeness, in Fig. 9 we show the input impedances of the unloaded and realistic loaded antennas, and, in Fig. 10 and Fig. 11, the directivity patterns of the loaded electrically small SRR antenna at 100 MHz and at the edge frequencies of the impedance bandwidth. The reference patterns of the unloaded SRR monopole antenna working at 100 MHz are not reported here, being almost the same as the ones of the loaded SRR antenna at the same frequency. Please note that the efficiency of the realistic loaded SRR antenna is, within the operation bandwidth, comparable to the one of the unloaded SRR-based antenna at 100 MHz (about 40%).

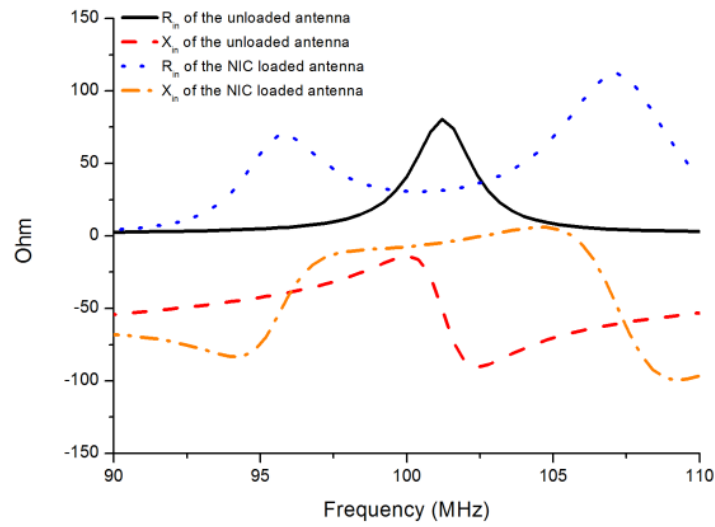


Fig. 9: Input impedance of the unloaded and real NIC loaded antennas in real (solid and dotted line, respectively) and imaginary (dashed and dot-dashed line, respectively) part.

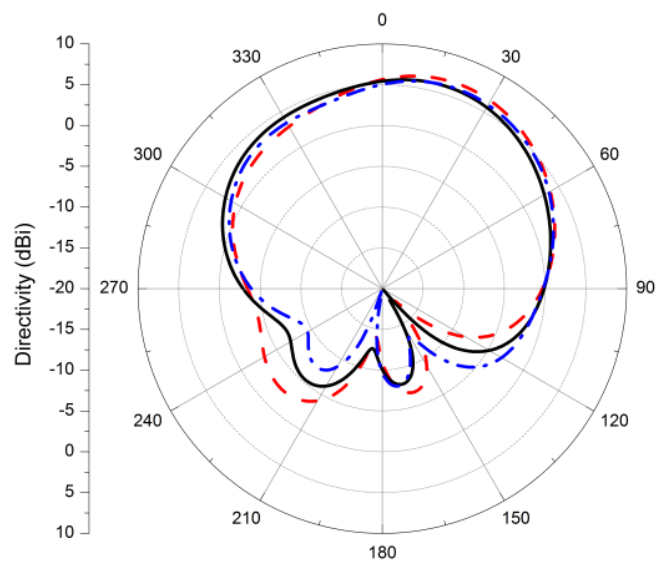


Fig. 10: Directivity patterns of the real NIC loaded antenna in the E-plane at 100 MHz (solid line), 96.1 MHz (dashed line) and 106.1 MHz (dot-dashed line).

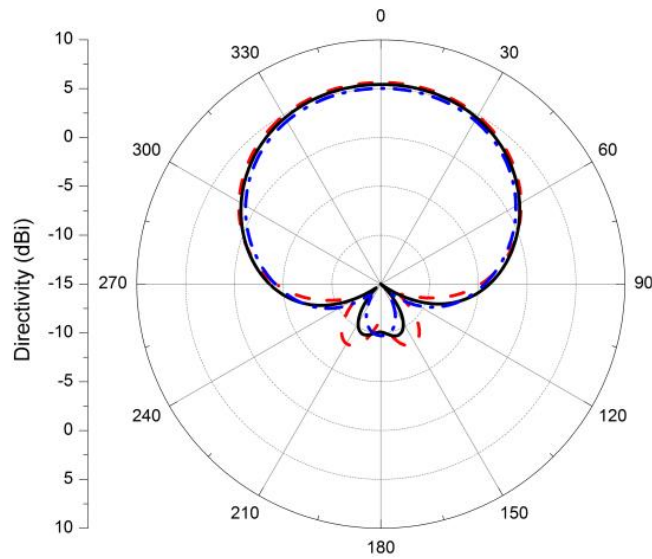


Fig. 11: Directivity patterns of the real NIC loaded antenna in the H-plane at 100 MHz (solid line), 96.1 MHz (dashed line) and 106.1 MHz (dot-dashed line).

1.5 Stability Issues

As mentioned before, when we design a device involving active circuits with positive feedback as NICs are, it is essential to perform a proper analysis to verify the stability of the overall system. This analysis, however, requires a special care. In fact, as exhaustively discussed in [19], the frequency domain methods typically employed in the field of RF and microwave active devices cannot be used for NIC components since they assume implicitly that Nyquist's criterion is fulfilled, which may not be the case. Alternative methods, as the one presented in [29] providing the evaluation of the system stability by using an ideal circulator, cannot be used, as well. In fact, as clarified in [30], this method is applicable in all the cases in which the circuit can become unstable only after its connection to the resonator. In our case, however, we cannot ensure the inherent stability of the circuit before we connect it to the antenna. For these reasons, only a time domain analysis, or a frequency one based on Nyquist's criterion, allows evaluating in an unambiguous way if the system is stable or not [19], [22].

At first, we concentrate our attention to the isolated actively loaded SRR described in section 1-2. In particular, we study the stability in the idealized case in which both the

SRR and the load are modeled as two LC tank circuits (see Fig. 12). Following the procedure presented in [22], deriving the stability condition is a straightforward task. Being, in fact, the transfer function (i.e. total impedance) of the system in Fig. 12:

$$Z(s) = \frac{L_t L s}{L + L_t + L(L_t C + L_t C_t) s^2}, \quad (7)$$

and the relative poles:

$$s_{1,2} = \pm \frac{\sqrt{-(L + L_t) / L_t L}}{\sqrt{C + C_t}}, \quad (8)$$

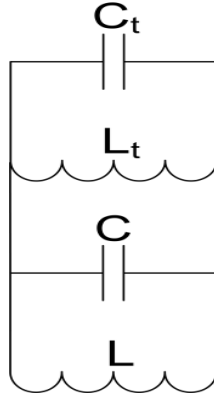


Fig. 12: Equivalent model of the ideally loaded SRR.

In order to ensure the stability of the overall circuit, the real parts of the poles must be non-positive quantities. Assuming negative values for C_t and L_t , as required for the reactance compensation, and a positive value for C and L , it is easy to derive the marginally stable condition as:

$$L_t \leq -L \text{ and } C_t > -C \rightarrow L_{tot} \geq 0, \quad C_{tot} > 0 \quad (9)$$

where:

$$\begin{aligned} C_{tot} &= C + C_t, \\ L_{tot} &= \frac{L_t L}{L + L_t}. \end{aligned} \quad (10)$$

Conditions (9) state that the total capacitance and inductance of the system must be both positive in order to grant the stability of the system. $L_{tot} = 0$ clearly represents a limit case for which the system is marginally stable regardless of the value of C_{tot} . Before continuing, it is worth remarking that non-positive real parts of the poles are obtained also when the total capacitance and inductance of the system are both negative. Clearly, this solution should be discarded, due to the intrinsic instability of the negative capacitance and the negative inductance. In addition, we remark also that (9) are only marginally conditions since we have neglected all the resistances in the equivalent circuit models.

Conditions (9) introduce a limitation in the ideal reactance cancellation condition for the capacitance ($C_t = -C$ and, therefore, $C_{tot} = 0$) that must be taken into account when designing the load. However, this aspect does not significantly affect the performance of the broadband SRR. We observe, in fact, that the bandwidth enhancement effect of the active load can be explained in terms of the Q -factor of the overall structure that, being a LC equivalent parallel circuit, is proportional to $\sqrt{C_{tot} / L_{tot}}$. It is well known that the bandwidth of a resonant circuit is inversely proportional to the quality factor, so its reduction results in a widening of the operation bandwidth. The ideal reactance cancellation condition (4) corresponds to a zero value of the Q -factor, being the overall capacitance equal to zero. The stability conditions (9), thus, force a bound for the Q -factor reduction ($C_{tot} \neq 0$ and, therefore, $Q > 0$) that is possible to achieve with a stable system. Typically, the described clash between the two conditions leads to a moderate reduction of the obtainable operation bandwidth.

The previous study, while theoretically useful, is still rather idealized. In fact, there are at least three elements that have been neglected: 1. the actual circuit load designed in Section III behaves as a LC tank circuit but the presence of parasitic elements in both branches of the structure results in a variation of the effective L and C values with the frequency; 2. the real parts of both the SRR and the load impedances have been neglected; 3. as discussed in Section 2, the LC model of the SRR represents an accurate model only in a narrow frequency range around the resonant frequency. The generalization of the stability analysis to include the neglected aspects, although

theoretically possible, is not trivial nor particularly useful. Moreover, when we turn to the stability study of the actively loaded SRR-antenna, the equivalent circuit of the overall structure became further complicated due to the electromagnetic coupling between the monopole antenna and the SRR.

Based on the previous discussion on the correct approaches used to check stability, in order to analyze the behaviour of the actively loaded antenna, we have decided to adopt a time-domain analysis using the tools offered by the circuit simulator. In particular, we have fed the realistic NIC loaded antenna with several time domain sources (e.g. sine wave, square wave, two sided exponential decay, Gaussian, etc.) and monitored the time-behaviour of the current at the ends of the coaxial cable feeding the antenna system. In all the tested cases the overall system was stable. Just as an example, in Fig. 13 and Fig. 14, we show the responses of the unloaded and loaded antennas, respectively, in the case of a source signal with a Gaussian spectrum in the range 96-106 MHz (slightly wider than the -10 dB bandwidth of the loaded antenna). For comparison, in these figures we report also the current signal obtained closing the source on an ideal 50 Ohm load. From Fig. 14, we see that current in the loaded antenna remains bounded and maintains the same envelope of the signal in the ideal 50 Ohm load.

Please note that, in light of the considerations made in section 4 about the circuit model of the lumped components, the stability of the system is guaranteed against all the parasitic effects and the variation of the lumped values (frequency dispersion and tolerances). Moreover, from all the set of our simulations, we have noticed that the system is not at the edge of stability, so further eventual variations of the component values should not prejudice the stability.

Moreover, as expected, in Fig. 13 it is possible to note a signal distortion, caused by the narrowband operation of the unloaded antenna. On the contrary, the signal in Fig. 14 is not affected by distortion and shows a smaller reduction of the signal amplitude, since the impedance bandwidth of the loaded antenna is approximately the same as the source signal. So, the comparison between the two plots provides further confirmation of the widening of the bandwidth in the actively loaded case.

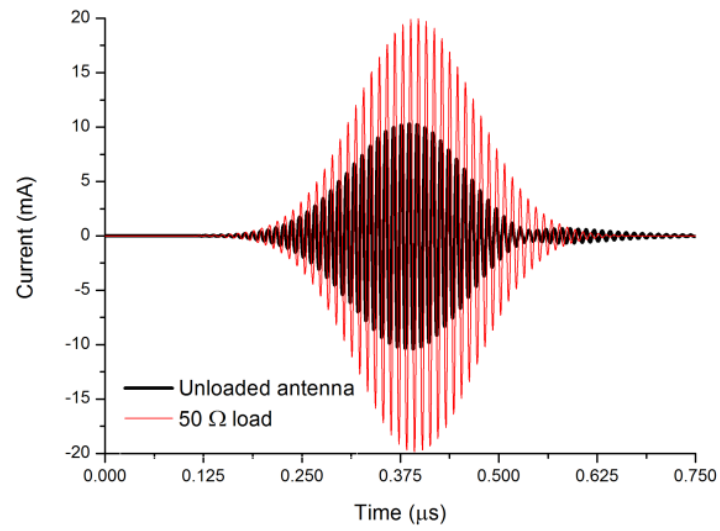


Fig. 13: Time-domain behavior of the current for the case of the unloaded antenna (thick black line) and for the case of an ideal 50 Ohm load (thin red line).

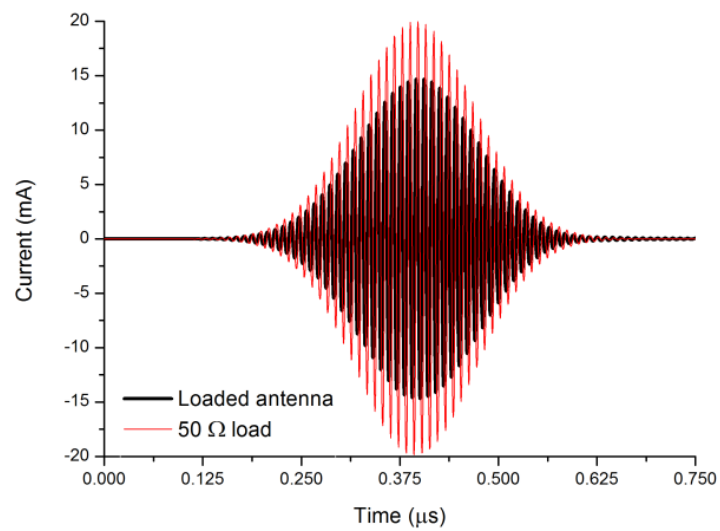


Fig. 14: Time-domain behavior of the current for the case of the loaded antenna (thick black line) and for the case of an ideal 50 Ohm load (thin red line).

1.6 Summary

In this Chapter, we have shown that the bandwidth of SRR-based devices can be considerably widened by using proper non-Foster circuit loads. At first, we have analytically and numerically determined the circuit topology and the relative lumped element values required to compensate the intrinsic reactance of an individual SRR and obtain a broadband response. Specifically, the simplest required load consists of a LC tank circuit, whose lumped element values are the opposite of the ones characterizing the behaviour of the SRR. Then, we have shown that the same procedure can be successfully applied to the case of a SRR-based monopole antenna and, following the same concept, to any metamaterial-inspired device based on the employment of SRRs. Properly integrating an electromagnetic and a circuit simulator, we have proposed a possible realistic implementation of the load, constituted by only commercially available active and passive elements. By using the designed circuit, we have numerically demonstrated a 7-times bandwidth improvement for a SRR-based monopole antenna already proposed in literature and scaled to work at VHF frequencies. Finally, we have theoretically and numerically investigated the stability of the overall system (monopole antenna + SRR + active load). In particular, considering the issues related to the classical stability assessment approaches, we have first developed a rigorous study for an idealized case and performed a time-domain analysis, revealing the stability of the proposed SRR-based antenna. The obtained results prove that non-Foster active loads can be successfully used to overcome the narrowband operation of SRRs, which is one of the major limitations of passive SRR-based components.

1.7 References

- [1] S.A. Tretyakov, "Meta-materials with wideband negative permittivity and permeability," *Microw. Opt. Technol. Lett.*, vol. 31, no. 3, pp. 163-165, 2001.
- [2] W. K. Chen, *The Circuit and Filters Handbook*. Boca Raton, FL: CRC Press, 2005.
- [3] R.M. Foster, "A reactance theorem," *Bell Syst. Tech. J.*, Vol. 3, pp. 259–267, 1924.
- [4] J. L. Merrill, "Theory of the negative impedance converter," *Bell Syst. Tech. J.*, Vol. 30, pp. 88–109, 1951.

- [5] J. G. Linvill, "Transistor negative impedance converters," *Proc. IRE*, Vol. 41, pp. 725–729, 1953.
- [6] A. Kaya, and E.Y. Yuksel, "Investigation of a compensated rectangular microstrip antenna with negative capacitor and negative inductor for bandwidth enhancement," *IEEE Trans. Antennas Propagat.*, Vol. 55, pp. 1275-1282, 2007.
- [7] G. Skahill, R.M. Rudich, and J. Piero, "Electrically small, efficient, wide-band, low-noise antenna elements," *1998 Antenna Application Symposium*, pp. 214-231.
- [8] S.E. Sussman-Fort, and R.M. Rudish, "Non-Foster Impedance Matching of Electrically-Small Antennas," *IEEE Trans. Antennas Propagat.*, Vol. 57, pp. 2230-2241, 2009.
- [9] J.T. Aberle and R. Loepsinger-Romak, *Active Antennas with Non-Foster Matching Networks*. San Rafael, CA: Morgan and Claypool Publishers, 2007.
- [10] C. Di Nallo, G. Bit-Babik, and A. Faraone, "Wideband antenna using non-foster loading elements," *2007 IEEE AP-S Int. Symp.*, pp. 4501-4504.
- [11] G. Bit-Babik, C. Di Nallo, J. Svirgelj, A. Faraone, "Small wideband antenna with non-Foster loading elements," *2007 ICEAA*, pp. 105-107.
- [12] J. Kern, D. H. Werner, and M. J. Wilhelm, "Active negative impedance loaded EBG structures for the realization of ultra-wide band artificial magnetic conductors," *2003 IEEE AP-S Int. Symp.*, Vol. 2, pp. 427-430.
- [13] D. F. Sievenpiper, "Superluminal Waveguides Based on Non-Foster Circuits for Broadband Leaky-Wave Antennas," *IEEE Antennas Wireless Propag. Lett.*, Vol. 10, pp. 231 - 234, 2011.
- [14] D. Sievenpiper, M. Jacob, and J. Long, "Active electromagnetic structures, metamaterials, and antennas," *2012 IEEE iWAT*, pp. 289-292.
- [15] P. Jin, and R.W. Ziolkowski, "Broadband, efficient, electrically small metamaterial-inspired antennas facilitated by active near-field resonant parasitic elements," *IEEE Trans. Antennas Propagat.*, Vol. 58, pp. 318-327, 2010.
- [16] R.W. Ziolkowski, and P. Jin, "Introduction of internal matching circuit to increase the bandwidth of a metamaterial-inspired efficient electrically small antenna," *2008 IEEE AP-S Int. Symp.*, pp. 1-4.
- [17] H. Mirzaei, and G.V. Eleftheriades, "A wideband metamaterial-inspired compact antenna using embedded non-Foster matching," *2011 IEEE APS-URSI Int. Sym.*, pp. 1950-1953.
- [18] H. Mirzaei, and G.V. Eleftheriades, "Antenna applications of non-Foster elements," *2012 IEEE iWAT*, pp. 281-284.
- [19] S. Hrubar, I. Krois, and A. Kiricenko, "Towards active dispersionless ENZ metamaterial for cloaking applications," *Metamaterials*, Vol. 4, pp. 89-97, 2010.

- [20] S. Hrabar, I. Krois, I. Bonic, and A. Kirichenko, "Negative capacitor paves the way to ultra-broadband metamaterials," *Appl. Phys. Lett.*, Vol. 99, 254103, 2011.
- [21] K. Z. Rajab, Y. Hao, D. Bao, C. G. Parini, J. Vazquez, and M. Philippakis, "Stability of active magnetoinductive metamaterials," *J. Appl. Phys.*, Vol. 108, 054904, 2010.
- [22] E. Ugarte-Muñoz, S. Hrabar, D. Segovia-Vargas, and A. Kirichenko, "Stability of non-Foster reactive elements for use in active metamaterials and antennas," *IEEE Trans. Antennas Propagat.*, to be published.
- [23] K.B. Alici and E. Ozbay "Electrically small split ring resonator antennas," *J. Appl. Phys.*, Vol. 101, pp. 08314, 2007.
- [24] F. Bilotti, A. Toscano, and L. Vegni, "Design of spiral and multiple split ring resonator for the realization of miniaturized metamaterial samples," *IEEE Trans. Antennas Propagat.*, Vol. 55, pp. 2258-2267, 2007.
- [25] F. Bilotti, A. Toscano, L. Vegni, K. Aydin, K.B. Alici and E. Ozbay, "Equivalent-circuit models for the design of metamaterials based on artificial magnetic inclusions," *IEEE Trans. Microwave Theory Tech.*, Vol. 55, pp. 2865-2873, 2007.
- [26] Computer Simulation Technology, CST Studio Suite 2011, <http://www.cst.com>.
- [27] S.E. Sussman-Fort, "Gyrator-based biquad filters and negative impedance converters for microwaves," *Int. J. RF Microw. CAE*, Vol. 8, pp. 86-101, 1998.
- [28] S. Kolev, B. Delacressonnière, and J.L. Gautier, "Using a negative capacitance to increase the tuning range of a varactor diode in MMIC technology," *IEEE Trans. Microw. Theory Tech.*, Vol. 49, pp. 2425-2430, 2001.
- [29] R.W. Jackson, "Criteria for the onset of oscillation in microwave circuits," *IEEE Trans. Microw. Theory Tech.*, Vol. 40, pp. 566-569, 1992.
- [30] R. W. Jackson, Comments on "Criteria for the onset of oscillation in microwave circuits," *IEEE Trans. Microw. Theory Tech.*, Vol. 40, pp. 1850-1851, 1992.

Chapter 2

Compact and multi-functional antennas based on MTM-inspired structures

The rapid development of wireless technologies, and their impact on the daily life, has increased the demand for communication devices that can operate using different communication standards. In antenna community, this trend results in an increased interest in compact and multi-functional antennas. In this regard, the recent introduction of MTM has allowed the design of numerous novel antennas characterized by enhanced performances and smaller dimensions with respect to the existing counterparts [1]-[14].

In this Chapter, we present two different solutions for designing compact antennas based on the use of MTM concepts. In particular, we first present the design and the operation principles of a printed monopole antenna loaded with two identical SRRs. In this case, the SRRs is used not only to miniaturize the antenna dimensions but also to introduce multiple resonances that can be properly selected by using electronic switches placed across the four gaps of the two SRRs. The physics behind the operation of the proposed antenna as well as the design procedure are presented in details and the expected multi-frequency operation is demonstrated and supported by proper full-wave numerical simulations. By properly combining the ON/OFF status of the four switches, in fact, it is possible to either change the operation frequency and/or the shape of the radiation pattern of the printed monopole or even add new operation frequencies. The proposed SRR-loaded printed antenna, thus, may find applications in mobile communications requiring pattern diversity and multiple operation frequencies. Then, we present the design of a compact antenna consisting of two orthogonal parasitic

meandered monopoles excited by the near-filed coupling with a feeding bow-tie. The two parasitic radiators and the driven element are placed on two different faces of the same dielectric substrate and a coaxial probe excites the bow-tie through a metallic ground plane. In this way, the antenna has compact dimensions of $\lambda_0/6 \times \lambda_0/12 \times \lambda_0/75$ (excluding the ground plane) and shows a good impedance matching in the 2.4-2.485 GHz Wi-Fi band with an overall efficiency around 50%.

2.1 Multi-Functional SRR-Loaded Printed Monopole Antenna

2.1.1 INTRODUCTION

Recently, Ozbay and Alici have proposed the design of a short whip antenna loaded by a SRR [10] that, without considering the ground plane dimensions, behaves as an electrically small antenna (ESA). The basic idea of this design is that the electrically short monopole excites the SRR placed in its close proximity, in such a way that the whole structure (monopole + SRR) resonates at a rather low frequency, due to the sub-wavelength dimensions of the SRR. Similarly, Varadan and Kim have designed a microstrip antenna using a SRR and a feed line [14]. In this case, the feed line and the SRR radiate independently and, therefore, the whole structure behaves as a dual-band antenna.

In this Section, inspired by the latter works, we propose the design of a planar multi-functional monopole antenna loaded with two equal SRRs printed on the same board and placed at the two sides of the monopole. Besides the miniaturization, the main idea here is to place four switches across the gaps of the two SRRs, in order to enable multi-functional capabilities, including pattern diversity and frequency operation shift. In addition, compared to [14], where the SRR resonates at a frequency greater than the resonant frequency of the isolated monopole, and to [10], where the dimensions of the ground plane are electrically large, the proposed planar version of the SRR-loaded short monopole is very compact, being the dimensions of the ground plane a fraction of the wavelength, at the lower operation frequency of the antenna.

The structure of the Section is as follows. In the next subsection, we describe the proposed antenna layout and show its operation at the lower resonant frequency. In the

last subsection, instead, we present the multi-functional capabilities obtained by using the switches placed across the gaps of the two SRRs.

2.1.2 DESIGN OF THE PROPOSED STRUCTURE

2.1.2.1 Design of the single-SRR loaded printed monopole

The basic configuration of the proposed antenna is shown in Fig. 15 and consists of a standard printed monopole antenna loaded with a squared SRR placed nearby. The monopole and the SRR are printed on the same substrate, as well as the coplanar waveguide feeding line.

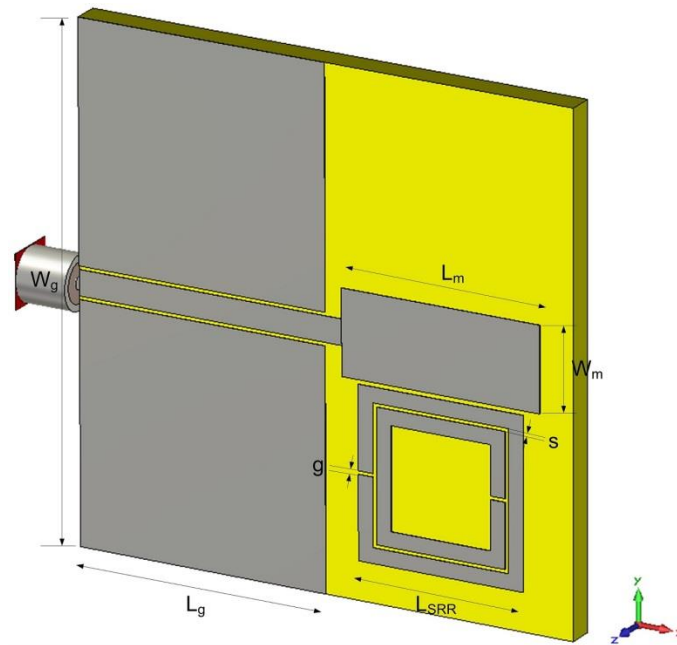


Fig. 15: Geometrical sketch of the single-SRR loaded printed monopole. Antenna dimensions are in mm: $W_g = 30$, $L_g = 15$, $L_m = 12$, $W_m = 5$, $L_{SRR} = 10$, $g = 0.2$, $s = 0.2$.

Slab material: FR-4 ($\epsilon_r = 4.4$, $\tan \delta = 0.0085$). Slab thickness: 1.59 mm. Separation between monopole and SRR: 0.2 mm.

Due to the currents flowing on the ground plane, the SRR is excited at its resonant frequency through the outer ring gap and radiates as a magnetic dipole directed along the z -axis. The resonant frequency of the SRR is mostly independent of the monopole dimensions and is mainly related to the geometrical dimensions of the SRR itself [15]-

[16]. Thus, being the SRR a sub-wavelength resonator, by appropriately designing its dimensions, we can obtain a much lower resonant frequency than that of the unloaded printed monopole.

In particular, as it can be seen from the plot in Fig. 16, we have obtained a resonant frequency at 1.75 GHz, at the expense of a slight variation in the monopole behavior. In fact, despite the monopole even resonates, its wide bandwidth is splits into two smaller ones.

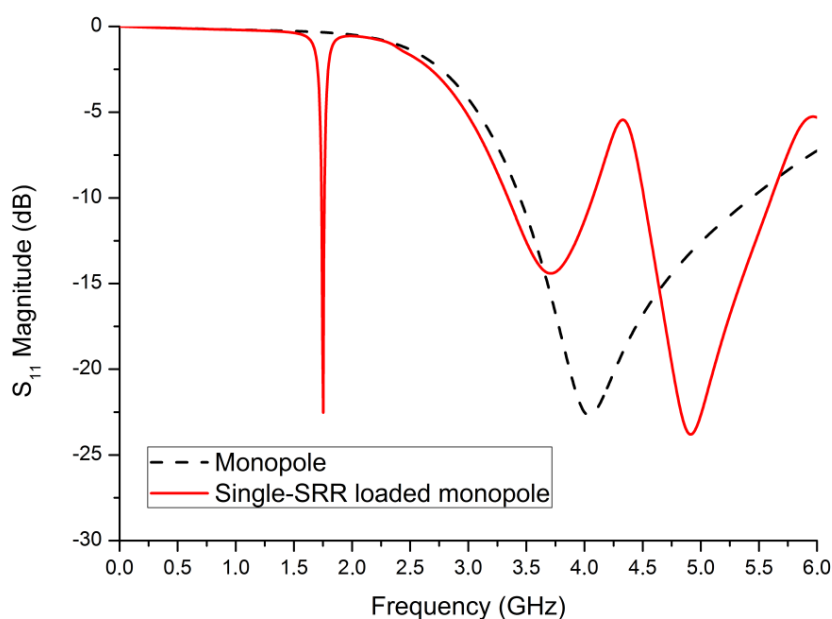


Fig. 16: Magnitude of the scattering parameter S_{11} of the antenna reported in Fig. 15 and of a standard printed monopole antenna with the same dimensions.

The 3D radiation pattern of the antenna at its lowest resonant frequency is reported in Fig. 17, while the radiation pattern at the upper bands is the one of the regular monopole and is not reported here for sake of brevity. From the result in Fig. 17, we observe that the beam produced by the radiating SRR points towards the monopole, which, then, acts as a director. The radiation efficiency at the lower resonant frequency is around 16%, due to the magnetic-type resonance and to the small size of the SRR.

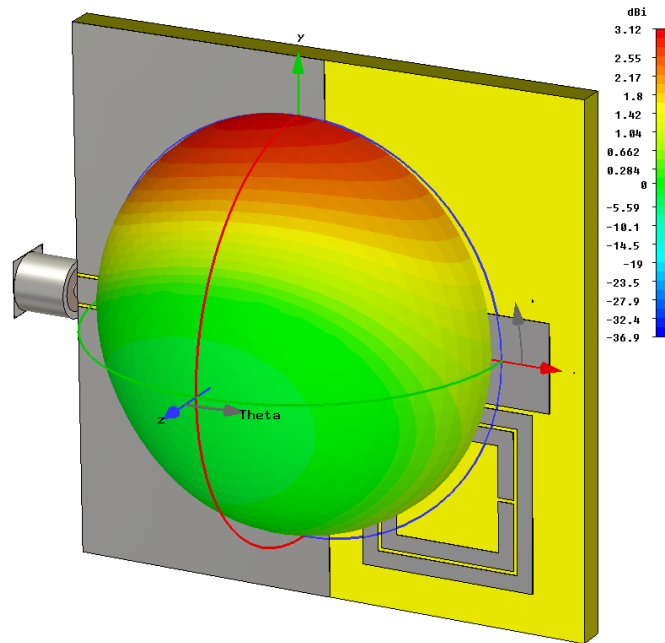


Fig. 17: 3D directivity pattern of the single-SRR loaded printed monopole at the resonant frequency of the SRR 1.752 GHz.

2.1.2.2 Two-SRR loaded printed monopole

The directivity pattern shown in Fig. 17 suggested us to use two symmetrical SRRs to further enhance the multi-functional capabilities of the antenna. The geometrical sketch of the structure is the one reported in Fig. 18. All the dimensions are assumed to be the same as in the previous design (see the caption of Fig. 15).

This time, however, we put four ideal switches connected across the four gaps of the two SRRs, as reported in Fig. 18. This structure has been simulated through the full-wave numerical solver CST Studio Suite [17] and the results of the simulations showing the different operation modes are reported and summarized in the next section.

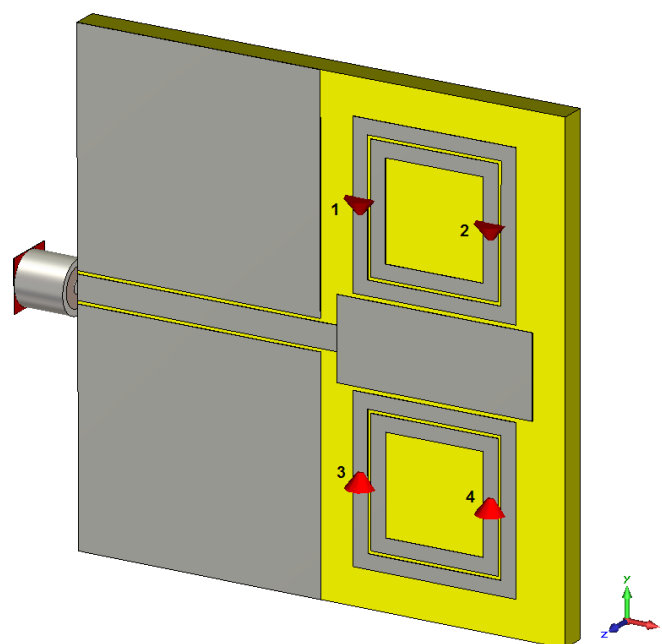


Fig. 18: Geometrical sketch of the multi-functional two-SRR loaded printed monopole. The numbered markers represent the switches placed in the gaps.

2.1.3 NUMERICAL RESULTS

Considering the ON-OFF status of the four switches, sixteen different configurations have been studied and numerically simulated. Only eight of them lead to interesting results (i.e. either antenna miniaturization or change of the antenna operation frequency while maintaining a reasonable matching level) and the corresponding operation frequencies and radiating properties have been summarized in Table 2.

The related magnitudes of the S_{11} parameter are reported in Fig. 19. When all the switches are in the ON status (i.e. the gaps are all open; line 1 of Table 2 – curve with square marks in Fig. 19), the structure works in two operation modes: one due to the excitation of both SRRs (the resonant frequency is slightly changed from the one of the single radiating SRR shown in the previous section: 1.72 GHz vs. 1.75 GHz; the radiation pattern points in two opposite directions along the y-axis, due to the specular positions of the SRRs with respect to the monopole) and one due to the monopole (with a reduced bandwidth compared to the isolated monopole: 3.5 – 5.5 GHz vs. 4.8 – 5.2 GHz).

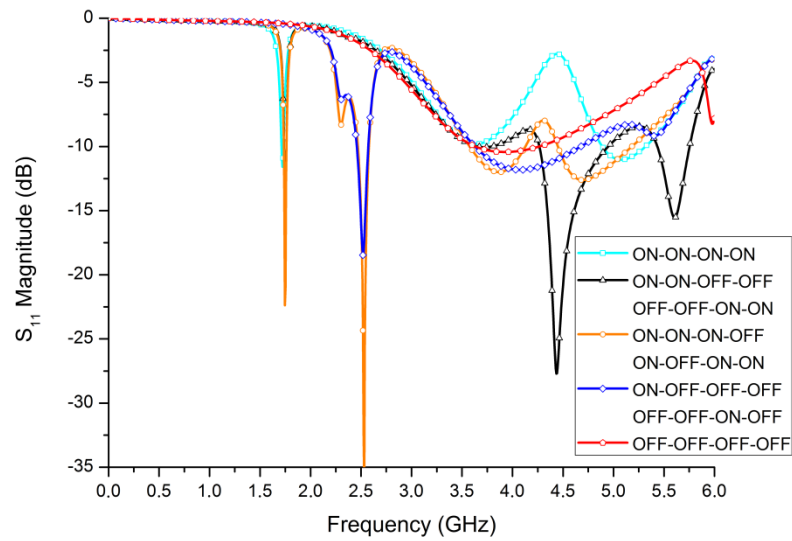
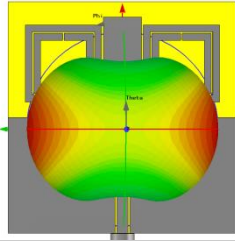
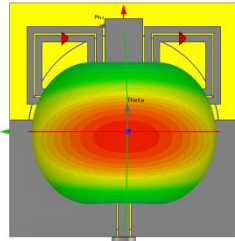
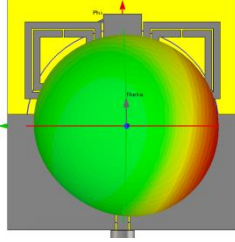
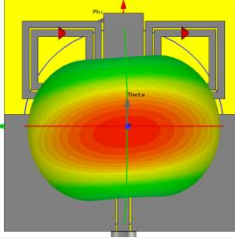
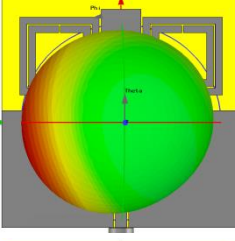
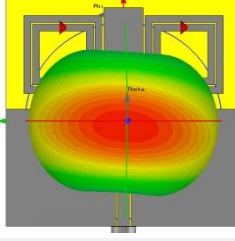
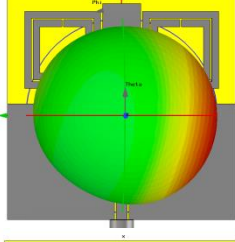
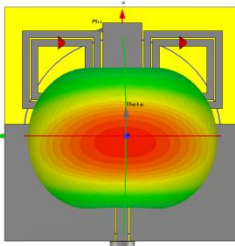
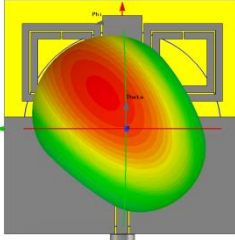


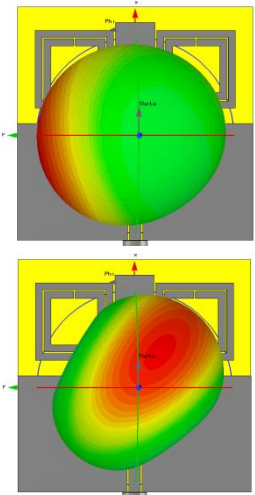
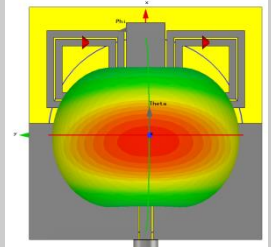
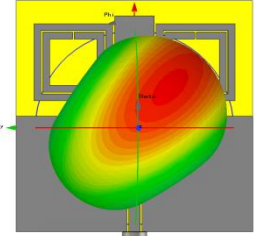
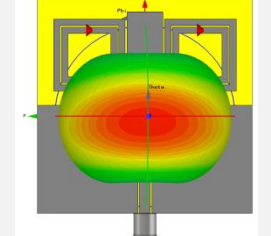
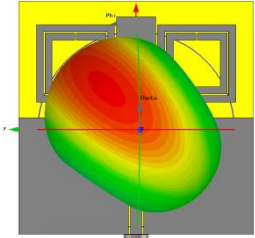
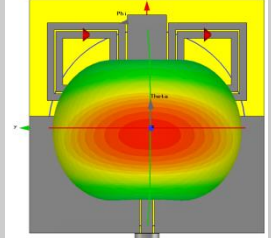
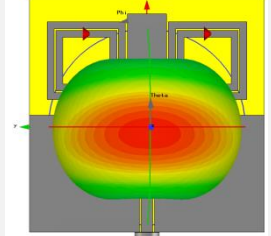
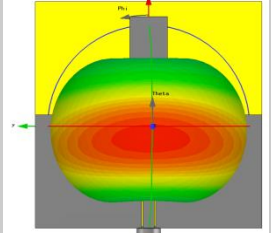
Fig. 19: Magnitude of the S_{11} parameter of the two-SRR loaded printed monopole for the eight switch status reported in Table 2.

When the switch status is such that only one of the two SRRs is active, while the other one has both the gaps short-circuited, the lower resonance frequency returns to the value of the single-SRR loaded monopole (1.75 GHz), as well as its radiation pattern. Therefore, depending on the active SRR, we can make the radiation pattern pointing either along the positive or the negative y -axis (lines 2-3 of Table 2 – curves with triangular marks in Fig. 19). The monopole behavior is again preserved, but, as already shown for the single-SRR loaded monopole, the operation band splits into two sub-bands (4.2 – 4.8 GHz, 5.4 – 5.7 GHz).

When the switch status is such that one SRR is regularly active and the other one has the inner gap short-circuited (lines 4-5 of Table 2 – curves with circular marks in Fig. 19), the antenna operates, as expected, in three modes: the lowest resonant frequency is due to the regularly active SRR (1.75 GHz), the next higher frequency (2.53 GHz) is due to the other SRR, which resonates at a higher frequency because of the short-circuit on the inner gap, and the third operation band is the one of the regular monopole, though split again into two sub-bands (3.5 – 4.1 GHz, 4.4 – 5.1 GHz). It is worth noticing that the radiation patterns due to the two excited SRRs point towards different directions.

Table 2: Summary of the operation frequencies and radiation properties for the different combinations of the switch status.

SRR_{left}		SRR_{right}		f_{SRR} (GHz)	radiation pattern $_{SRR}$	BW_{mon} (GHz)	radiation pattern $_{\text{mon}}$
sw 1	sw 2	sw 3	sw 4				
ON	ON	ON	ON	1.72		4.8 – 5.2	
ON	ON	OFF	OFF	1.75		4.2 – 4.8 5.4 – 5.7	
OFF	OFF	ON	ON	1.75		4.2 – 4.8 5.4 – 5.7	
ON	ON	ON	OFF	1.75 (SRR_{left})		3.5 – 4.1 4.4 – 5.1	
				2.53 (SRR_{right})			

SRR _{left}		SRR _{right}		f _{SRR} (GHz)	radiation pattern _{SRR}	BW _{mon} (GHz)	radiation pattern _{mon}
sw 1	sw 2	sw 3	sw 4				
ON	OFF	ON	ON	1.75 (SRR _{right}) 2.53 (SRR _{left})		3.5 – 4.1 4.4 – 5.1	
ON	OFF	OFF	OFF	2.53		3.6 – 4.6	
OFF	OFF	ON	OFF	2.53		3.6 – 4.6	
OFF	OFF	OFF	OFF	-	-	3.7 – 4.0	
no SRRs				None	none	3.5 – 5.5	

When the switch status is such that one SRR has both the gaps short-circuited and the other one the inner gap short-circuited and the outer gap open (lines 6-7 of Table 2 – curves with rhombic marks in Fig. 19), the lower operation frequency is due to the resonance of the latter SRR (2.53 GHz), while the monopole operation is again preserved, though the frequency band (3.6 – 4.6 GHz) is reduced if compared to the isolated printed monopole.

Finally, when the two SRRs have all the gaps short-circuited (line 8 of Table 2 – curves with hexagonal marks in Fig. 19), they do not resonate at lower frequencies anymore and the antenna works only as a monopole, with the bandwidth (3.7 – 4.0 GHz) affected by the mismatch caused by the presence of the two pairs of loops printed at the left and right sides of the monopole.

In summary, the proposed antenna is a truly multi-functional one and may find application in mobile terminals of modern communication systems, where smart tools, such as pattern diversity, MIMO channels, and frequency agility need to be used to increase the quality of service and maximize the signal-to-noise ratio in multipath affected environments. The proposed antenna, in fact, is capable to work at different operation frequencies, change the operation frequencies in real-time, and enable pattern diversity by properly configuring the status of the four switches mounted across the gaps of the SRRs.

It is worth remarking that in our simulations, the switches have been assumed as galvanic connections. However, their actual implementation can be obtained by using commercial devices based on different technologies, such as PIN diodes [18], FETs [19], optical switches [20], and radio frequency micro-electro-mechanical system (RF-MEMS) [21]. In particular, PIN diodes can be used, without significantly affecting the antenna performances, because in the off-state in which the switch essentially acts as a resistance, the SRR no longer resonates and there is no current flowing in the switches. However, it is important to remark that the capacitance of the switches in the on-state (of the order of 0.1-1 pF) has to be taken into account at the design stage, anyway, because it influences the resonant frequency of the SRR.

2.2 Design of a Compact Antenna by using Orthogonal Parasitic Meandered Monopoles

2.2.1 INTRODUCTION

Monopole antennas have been widely used in mobile communication systems due to their simple structure, omnidirectional radiation pattern and size reduction compared to the equivalent dipole antennas. However, the main dimension of a quarter-wave monopole ($\lambda_0/4$, where λ_0 is the free-space wavelength at the operating frequency) is often too high for modern communication systems, which are characterized by ever smaller available space for the radiating element. For this reason, several effective ways to reduce the antenna dimensions are proposed, such as the use of fractal or meandered structures [22], shorting pins [23] and MTM-inspired resonators [24]. However, as is evident by considering the well-known limits of electrically small antennas [25]-[27], the antenna bandwidth decreases with decreasing its size. Therefore, it is often difficult to simultaneously satisfy the requirements in terms of impedance bandwidth and overall dimensions.

In order to design a compact antenna with a good impedance matching in the 2.4 GHz Wi-Fi band, we propose here to use two orthogonal meandered printed monopoles with slightly different dimensions. In this way, we are able to merge the two independent resonances of the monopoles to achieve a wideband response.

However, although the meandered structure may seem the simplest solution to reduce the monopole size, it can lead to difficulties in the impedance matching to the source. In order to overcome this issue, we propose here to use a MTM-inspired solution [28]. In fact, MTMs concepts have been widely used to design several radiating structures [29]-[32]. Some of them [28], [31]-[32] are based on the employment of driven and parasitic elements that allow obtaining nearly complete impedance matching to the source and high radiation efficiency. Following this approach, although the two monopoles are the main radiating structures, in our case they aren't connected to the feeding coaxial cable but act as parasitic resonators of a feeding bow-tie.

The structure of this Section is as follows. In Subsection 2, we present the design of a compact antenna based on the use of two meandered monopoles with the same

dimensions. However, due to its narrow bandwidth, this structure cannot be used to cover the entire frequency spectrum of Wi-Fi systems. Therefore, in Subsection 3, we slightly change the dimensions of one of the monopoles in order to obtain two resonant frequencies that, properly merged, allow covering the 2.4-2.485 GHz frequency band.

2.2.2 ANTENNA DESIGN WITH EQUAL MEANDERED MONOPOLES

2.2.2.1 Antenna Structure

In order to show the benefit of using two slightly different monopoles in term of operating bandwidth, we first consider the design of an antenna with equal meandered monopoles. The structure, shown in Fig. 20-21, consists of a square ground plane and an FR4 substrate ($\epsilon_r = 4.3$; $\tan \delta = 0.025$; thickness 1.6 mm) positioned orthogonal to it. Two orthogonal meandered monopoles connected to the ground are etched on one side of the dielectric substrate. On the other side, it is placed a bow-tie-like monopole connected to the inner conductor of a 50 Ω coaxial cable.

By properly co-designing the dimensions of the parasitic monopoles and the length of the driven bow-tie, we can tune the resonant frequency of the overall structure and obtain a good impedance matching. Moreover, thanks to the meandered structure, a compact antenna with overall dimensions of $\lambda_0 / 6 \times \lambda_0 / 12 \times \lambda_0 / 75$ has been obtained.

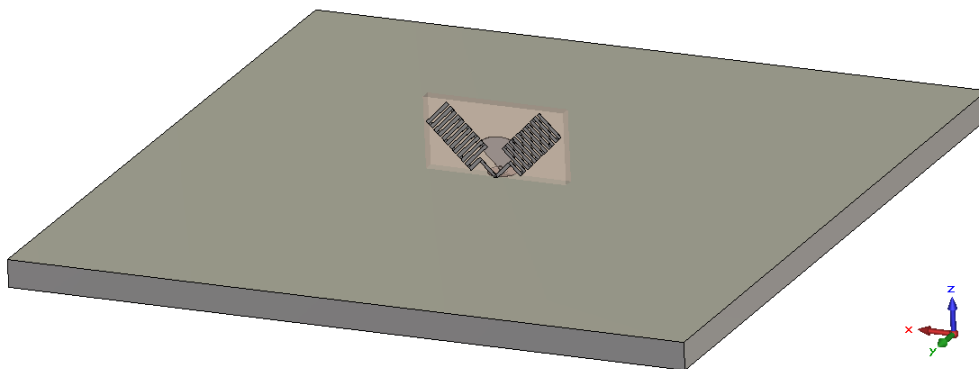


Fig. 20: Perspective view of the proposed antenna. The ground side is 10 cm.

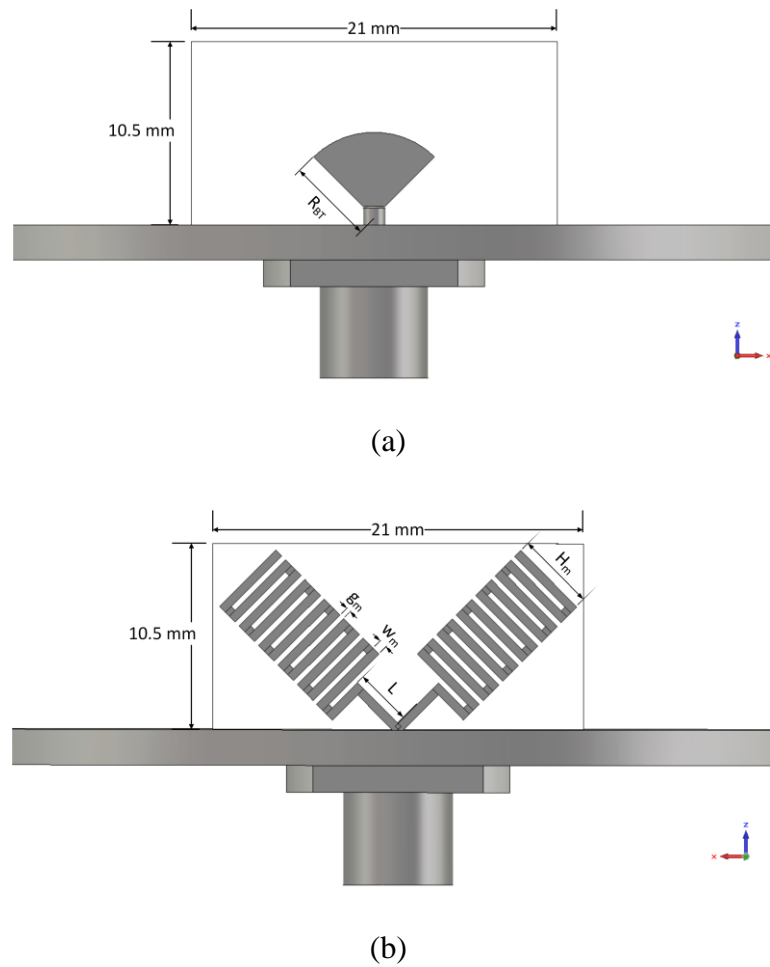


Fig. 21: Front view (a) and back view (b) of the proposed antenna with equal meandered monopoles. Antenna dimensions are: $R_{BT} = 4.9$ mm, $H_m = 4.5$ mm, $g_m = 0.3$ mm, $w_m = 0.48$ mm, $L = 3$ mm.

2.2.2.2 Simulation Results

The behavior of the structure presented in the previous subsection has been numerically evaluated by using the full-wave simulator CST Microwave Studio [17]. The reflection coefficient, reported in Fig. 22, show good impedance matching around 2.4 GHz. However, due to the identical size of the two monopoles, only one resonant frequency with a 2% -10 dB fractional bandwidth is present. Therefore, this antenna cannot cover the entire Wi-Fi band at 2.4 GHz.

For this reason, in the next Subsection we propose a modified structure with different monopoles lengths that shows a greater impedance bandwidth.

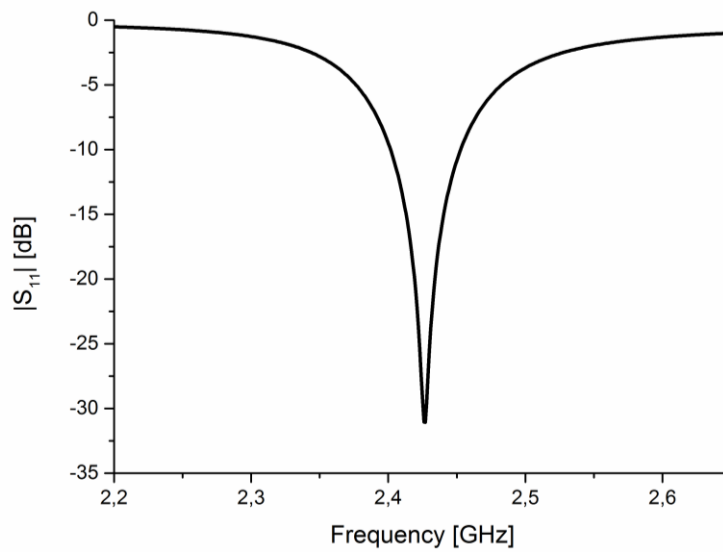


Fig. 22: Reflection coefficient amplitude of the proposed antenna with equal meandered monopoles.

For sake of completeness, in Fig. 23 we report also the radiation patterns at the resonant frequency of 2.425 GHz. The overall efficiency is around 65% in all the impedance bandwidth. Finally, the surface currents on the two meandered monopoles at 2.425 GHz, shown in Fig. 24, have approximately the same intensity, confirming the single frequency resonant behavior.

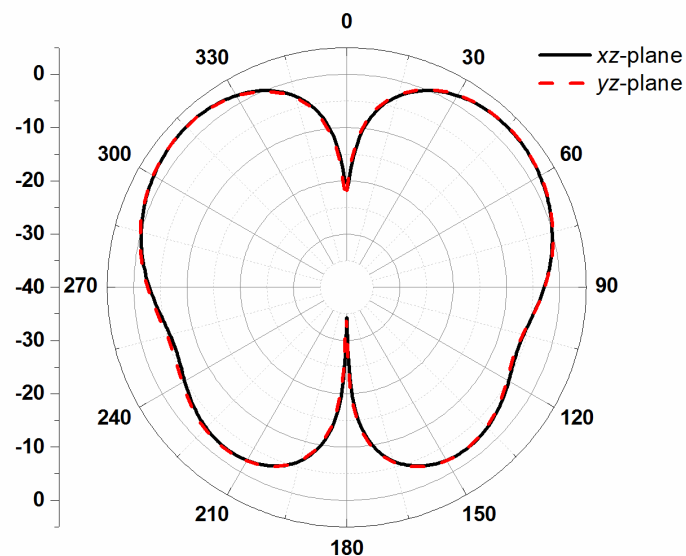


Fig. 23: Realized gain pattern at the resonant frequency (2.425 GHz) of the antenna with equal meandered monopoles.

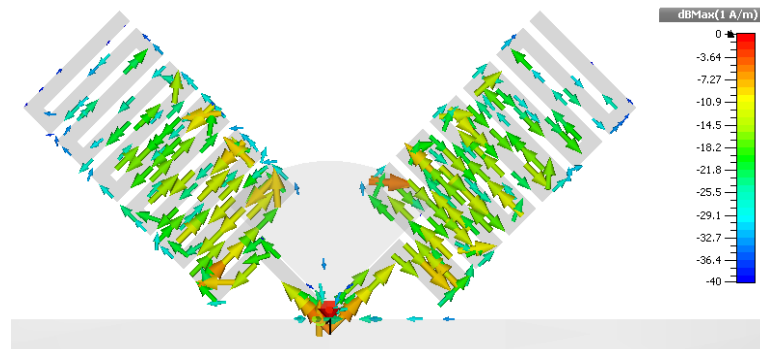


Fig. 24: Surface currents on the two meandered monopoles at the resonant frequency of the overall structure (2.425 GHz).

2.2.3 ANTENNA DESIGN WITH SLIGHTLY DIFFERENT MEANDERED MONOPOLES

2.2.3.1 Antenna Structure

In Subsection 2 we have presented the design of a compact antenna by using two parasitic meandered monopoles and a driven bow-tie. As shown through proper full-wave simulations, this antenna has a narrow operating bandwidth that doesn't allow its employment as radiating element in 2.4 GHz Wi-Fi band. In order to enlarge its operating bandwidth and make it compatible with that application field, we propose here to use two slightly different meandered monopoles with different but close together resonant frequencies.

The resulting structure and the corresponding dimensions are shown in Fig. 25. In particular, the lengths of the two meandered monopoles differ for 5 mm, while all the other dimensions of the two monopoles are equal between them.

2.2.3.2 Simulation Results

The simulated reflection coefficient, obtained by using CST Microwave Studio, is shown in Fig. 26 and compared to the previous case. By properly co-designing the bow-tie and meandered monopoles, a good impedance matching is obtained. Moreover, due to the different dimensions of the monopoles, two slightly different resonant frequencies are readily apparent. In this way, the -10 dB fractional bandwidth grows from 2% to 3.5% and allows covering the entire 2.4-2.485 GHz band assigned to the Wi-Fi systems.

In particular, as can be seen from Fig. 27 and Fig. 28, the shortest meandered monopole resonates at 2.416 GHz, while the longest one resonates at 2.461 GHz. These frequencies correspond to the two negative peaks of the reflection coefficient. The radiation patterns at these resonant frequencies are shown in Fig. 29-30.

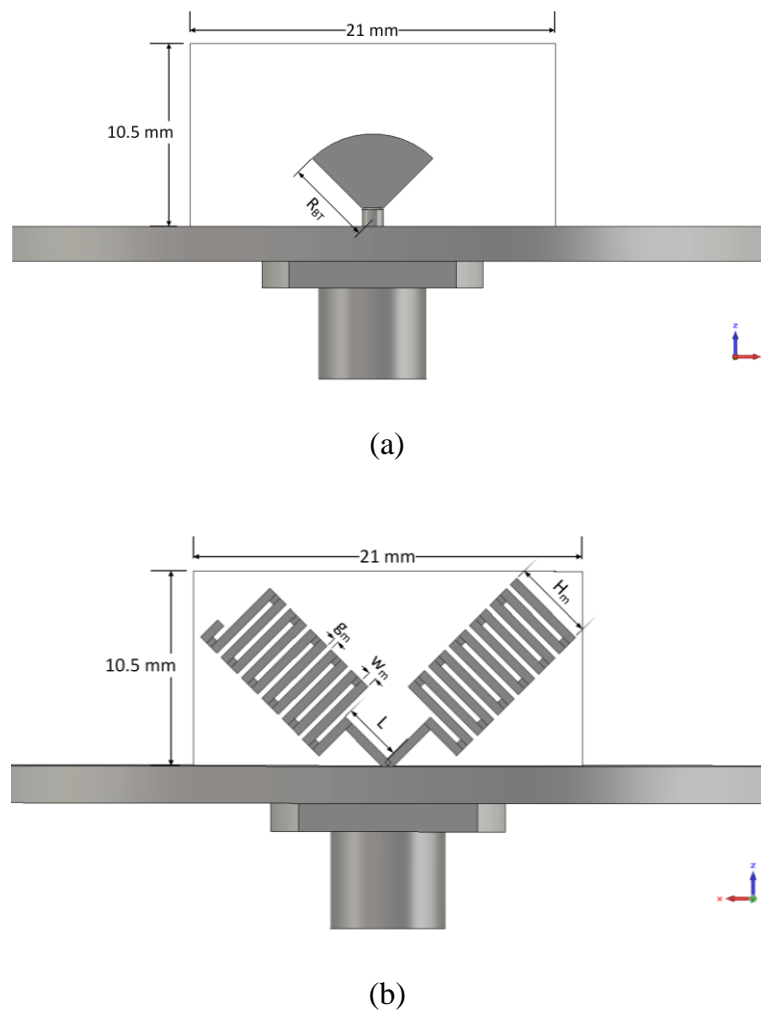


Fig. 25: Front view (a) and back view (b) of the proposed antenna with slightly different meandered monopoles. Antenna dimensions are: $R_{BT} = 5$ mm, $H_m = 4.5$ mm, $g_m = 0.3$ mm, $w_m = 0.48$ mm, $L = 3$ mm.

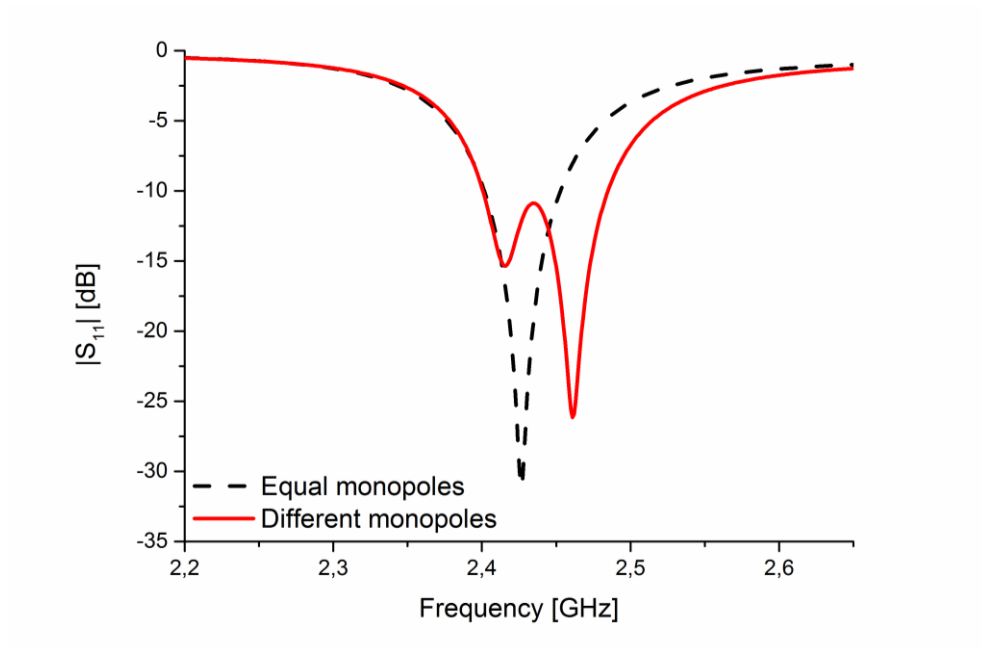


Fig. 26: Reflection coefficient amplitude of the proposed antenna with slightly different monopoles (red-solid line), compared to the one of the previous case (black-dashed line).

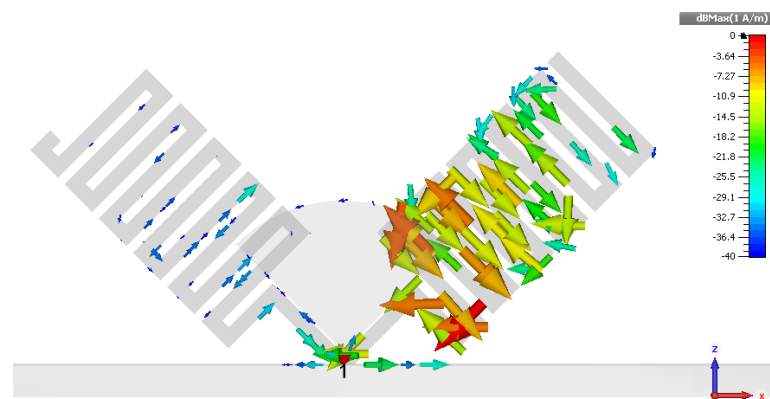


Fig. 27: Surface currents on the two meandered monopoles at the lowest resonant frequency of the overall structure shown in Fig. 25.

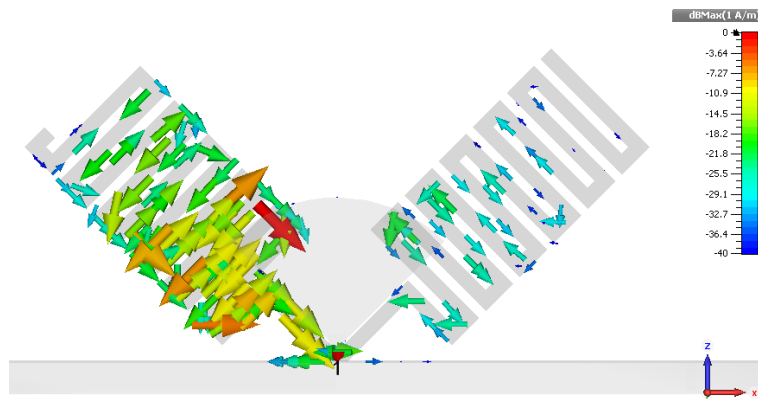


Fig. 28: Surface currents on the two meandered monopoles at the highest resonant frequency of the overall structure shown in Fig. 25.

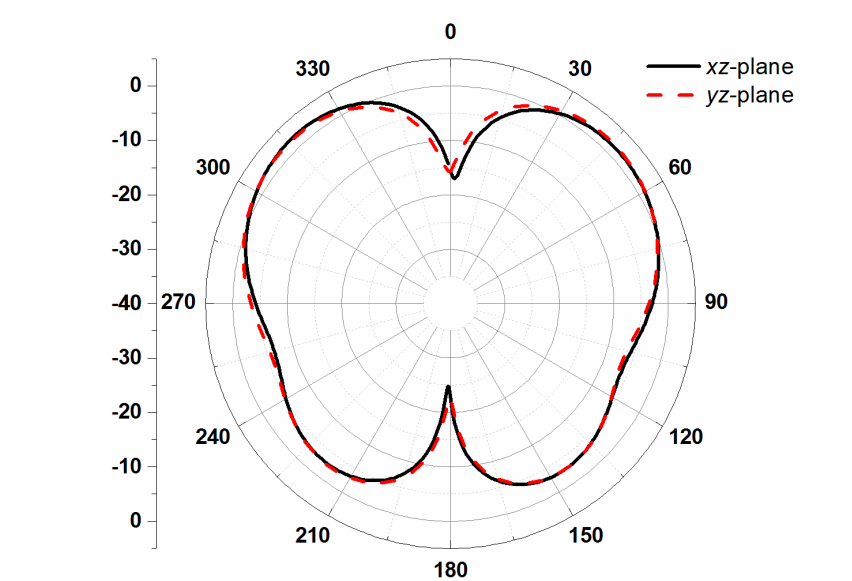


Fig. 29: Realized gain pattern at the lowest resonant frequency (2.416 GHz) of the antenna with slightly different monopoles.

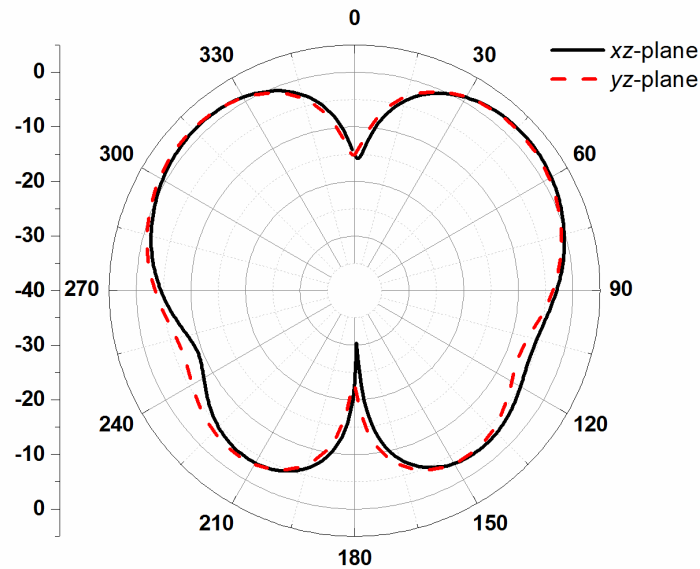


Fig. 30: Realized gain pattern at the highest resonant frequency (2.461 GHz) of the antenna with slightly different monopoles.

2.3 Summary

In this Chapter, we have first presented a novel electrically small and multi-functional printed monopole antenna loaded with a couple of SRRs, whose operation is assisted by four switches placed across the gaps. Considering the presence of four switches to open and close the gaps of the SRRs, we have shown that such an antenna can work at different frequencies, enabling real-time pattern diversity and operation frequency shift. The proposed antenna, thus, represents a good candidate for mobile terminals enabling smart countermeasures in multipath affected and highly interfered channels. The analysis of the proposed antenna has been supported by full-wave numerical simulations performed through CST Design Studio.

Then, we have presented a compact antenna consisting of two orthogonal meandered monopoles that act as parasitic elements of a driven bow-tie. In particular, we have shown that by using two monopoles with slightly different dimensions, a greater impedance bandwidth can be obtained. Using this approach, we have presented a compact antenna operating in the 2.4 GHz Wi-Fi band with overall dimensions of $\lambda_0/6 \times \lambda_0/12 \times \lambda_0/75$.

2.4 References

- [1] R.W. Ziolkowski and A.D. Kipple, "Application of double negative materials to increase the power radiated by electrically small antennas," *IEEE Trans. Antennas Propagat.*, vol. 52, pp. 2626-2640, 2003.
- [2] R.W. Ziolkowski and A. Erentok, "Metamaterial-based efficient electrically small antennas," *IEEE Trans. Antennas Propagat.*, vol. 54, pp. 2113-2130, 2006.
- [3] P. Jin and R.W. Ziolkowski, "Multi-frequency, linear and circular polarized, metamaterial-inspired, near-field resonant parasitic antennas," *IEEE Trans. Antennas Propagat.*, vol. 59, pp. 1446-1459, 2011.
- [4] F. Qureshi, M.A. Antoniades, and G.V. Eleftheriades, "A compact and low-profile metamaterial ring antenna with vertical polarization," *IEEE Antennas Wireless Propag. Lett.*, vol. 4, pp. 333-336, 2005.
- [5] A. Alù, F. Bilotti, N. Engheta, and L. Vegni, "Sub-wavelength planar leaky-wave components with metamaterial bilayers," *IEEE Trans. Antennas Propagat.*, vol. 55, pp. 882-891, 2007.
- [6] F. Bilotti, A. Alù, and L. Vegni, "Design of miniaturized metamaterial patch antennas with μ -negative loading," *IEEE Trans. Antennas Propagat.*, vol. 56, pp. 1640-1647, 2008.
- [7] J. Zhu, M.A. Antoniades, and G.V. Eleftheriades, "A compact tri-band monopole antenna with single-cell metamaterial loading," *IEEE Trans. Antennas Propagat.*, vol. 58, pp. 1031-1038, 2010.
- [8] S. Tricarico, F. Bilotti, and L. Vegni, "Multi-functional dipole antennas based on artificial magnetic metamaterials," *IET Microw. Antennas Propag.*, vol. 4, pp. 1026-1038, 2010.
- [9] F. Bilotti and C. Vegni, "Design of high-performing microstrip receiving GPS antennas with multiple feeds," *IEEE Antennas Wireless Propagat. Lett.*, vol. 9, pp. 248-251, 2010.
- [10] K.B. Alici and E. Ozbay "Electrically small split ring resonator antennas," *J. Appl. Phys.*, vol. 101, pp. 08314-1-4, 2007.
- [11] A. Alù, F. Bilotti, N. Engheta, and L. Vegni, "A conformal omni-directional sub-wavelength metamaterial leaky-wave antenna," *IEEE Trans. Antennas Propagat.*, vol. 55, pp. 1698-1708, 2007.
- [12] F. Bilotti and C. Vegni, "On the employment of artificial magnetic metamaterials to effectively reduce the back-lobe of patch antennas," *Electromagnetics*, vol. 48, pp. 513-522, 2008.
- [13] J. Gemio, J. Parròn, P. de Paco, G. Junkin, J. Marin, and O. Menéndez, "A split-ring-resonator loaded monopole for triple band applications," *J. Electromagn. Waves and Applicat.*, vol. 24, pp. 241-250, 2010.

- [14] V. V. Varadan and I. K. Kim, "Compact, multi band plasmonic resonator antenna," Proc. of the IEEE/URSI Int. Symp. Antennas Propagat., Charleston, USA, 1-5 June 2009.
- [15] F. Bilotti, A. Toscano, and L. Vegni, "Design of Spiral and Multiple Split-Ring Resonators for the realization of miniaturized metamaterial samples," IEEE Trans. Antennas Propagat., vol. 55, pp. 2258-2267, 2007.
- [16] F. Bilotti, A. Toscano, L. Vegni, K.B. Alici, K. Aydin, and E. Ozbay, "Equivalent circuit models for the design of metamaterials based on artificial magnetic inclusions," IEEE Trans. Microwave Theory Tech., vol. 55, pp. 2865-2873, 2007.
- [17] CST Studio Suite 2010, CST Computer Simulation Technology AG, www.cst.com.
- [18] D.J. Roscoe, L. Shafai, A. Ittipiboon, M. Cuhaci, and R. Douville, "Tunable dipole antennas," Proc. of the IEEE/URSI Int. Symp. Antennas Propagat., vol. 2, pp. 672-675, 1993.
- [19] S. Kawasaki, and T. Itoh, "A slot antenna with electronically tunable length," Proc. of the IEEE/URSI Int. Symp. Antennas Propagat., vol. 1, pp. 130-133, 1991.
- [20] J. L. Freeman, B. J. Lamberty, and G.S. Andrews, "Optoelectronically reconfigurable monopole antenna," Electron. Lett., vol. 28, pp. 1502-1503, 1992.
- [21] B. Schoenliner, A. Abbaspour-Tamijani, L.C. Kempel, and G.M. Rebeiz, "Switchable low-loss RF MEMS Ka-band frequency-selective surface," IEEE Trans. Microwave Theory Tech., vol. 52, pp. 2474-2481, 2004.
- [22] S. R. Best, "On the performance properties of the Koch fractal and other bent wire monopoles," IEEE Trans. Antennas Propagat., vol. 51, pp. 1292-1300, June 2003.
- [23] S. C. Pan and K. L. Wong, "Dual frequency triangular microstrip antenna with a shorting pin", IEEE Trans Antennas Propagation, pp. 1889-1891, December 1997.
- [24] M. Barbuto, F. Bilotti, and A. Toscano, "Design of a multifunctional SRR-loaded printed monopole antenna," Int. J. RF Microw. CAE, vol. 22, pp. 552-557, 2012.
- [25] R. C. Hansen, "Fundamental limitations in antennas," Proceedings of the IEEE, vol. 69, pp. 170-182, February 1981.
- [26] J. S. McLean, "A re-examination of the fundamental limits on the radiation Q of electrically small antennas," IEEE Trans. Antennas Propagat., vol. 44, pp. 672-676, May 1996.
- [27] R. Collin, S. Rothschild "Evaluation of antenna Q," IEEE Trans. Antennas Propagat., vol. 12, pp. 23-27, January 1964.
- [28] P. Jin and R. W. Ziolkowski, "Multiband extensions of the electrically small near field resonant parasitic Z antenna," Microw. Antennas Propag., vol. 4, pp. 1016-1025, Aug. 2010.
- [29] M. Barbuto, F. Trotta, F. Bilotti, and A. Toscano "A combined bandpass filter and polarization transformer for horn antennas," IEEE Antennas Wireless Propag. Lett., vol. 12, pp. 1065-1068, 2013.

-
- [30] J. Zhu, M. A. Antoniadis, and G. V. Eleftheriades “A compact tri-band monopole antenna with single-cell metamaterial loading,” *IEEE Trans. Antennas Propagat.*, vol. 58, pp. 1031-1038, April 2010.
- [31] P. Jin, C. C. Lin, and R. W. Ziolkowski, “Multifunctional, electrically small, planar near-field resonant parasitic antennas,” *IEEE Antennas Wireless Propag. Lett.*, vol. 11, pp. 200–204, 2012.
- [32] M. Barbuto, A. Monti, F. Bilotti, and A. Toscano, “Design of a non-foster actively loaded SRR and application in metamaterial-inspired components,” *IEEE Trans. Antennas Propag.*, vol. 61, no. 3, pp. 1219–1227, Mar. 2013.

Chapter 3

Horn antennas with integrated MTM-inspired filtering modules

Band-pass and band-stop filters are usually employed in the receiver front-end of communication systems in order to improve the performance and increase the signal-to-noise ratio. In fact, since wideband communication systems use a large portion of the electromagnetic spectrum, the performance of the receiver front-end is typically affected by the interfering signals generated by other services operating in a narrower portion of the same frequency band. On the other hand, narrowband receiving systems have to discriminate the desired signal from the out-of-band noise. Therefore, depending on the communication system and the relative operating environment, proper filtering modules with band-pass or band-stop characteristics should be inserted between the antenna and the receiver front-end, resulting in increased complexity, size, weight and cost of the overall system.

One possible solution to solve the problem is to employ a filtering antenna, or *filtenna*, which integrates the radiating element and the filter in a single module [1]-[7].

In the past few years, several configurations have been proposed to design both microstrip and horn antennas with a filtering behavior. In particular, for patch antennas a multitude of both band-pass and band-stop configurations (see, for instance, [4]-[7]) have been proposed. On the contrary, in the case of filtering horn antennas only few band-pass modules have been presented [1]-[3].

In this Chapter, in order to obtain proper horn filtennas with band-stop or band-pass operation, we introduce a novel approach, based on the use of MTM-inspired resonators. In particular, we show that, by properly placing a MTM-inspired resonator inside a standard horn antenna, the radiating and matching properties of the overall

structure are affected by the strong resonance of the inclusion leading to a band notch or a band-pass behavior around its resonant frequency.

The structure of the Chapter is as follows. In Section 1, we present the design of a 3D linear-to-circular polarization transformer that can be easily integrated in existing radiation systems to change their polarization and reduce impedance bandwidth of a standard horn antenna. In Section 2, we improve this approach by using a 2D structure consisting of only a complementary electrically small resonators etched on a metallic sheet. Finally, in Section 3, we present a filtering module with an opposite behavior (a notched-band), which can be inserted inside horn antennas to limit their receiving properties around the operating frequency of a narrow-band interfering signal.

3.1 Linear-to-Circular Polarization Transformer

In the last years there has been a great interest in a physical phenomenon known as “enhanced transmission” through sub-wavelength single apertures drilled in a metallic plate, at both microwave and optical frequencies. As theoretically reported in [8], in the case of an electrically small circular aperture of radius a in a perfectly conducting metallic screen of zero thickness, transmission is negligible and goes as the fourth power of the ratio a/λ_0 . In the last decade, however, several approaches have been proposed to overcome this limit. The first technique is based on the excitation of perturbed leaky-modes by corrugating the metallic surface around the hole with periodic grooves and properly choosing the corrugation period to obtain a reasonable coupling with the radiation impinging on the screen [9]. An alternative approach, exploiting again the properties of perturbed leaky-wave resonances, is proposed in [10]. In that setup, the extraordinary transmission is obtained by placing on the two sides of the aperture, MTM covers characterized by near-zero values of either permittivity or permeability, depending on the polarization of the impinging radiation. Better performances have been achieved by using conjugate-matched single-negative MTM bi-layers on the two opposite faces of the screen, allowing the reduction of the cover thickness. Then, in order to reduce the transverse dimensions of the cover, a new setup exploiting the resonances localized at the interface between conjugate-matched single-negative MTM has been proposed. In that case, the transverse extension of the cover is comparable to

the hole dimension. Following this approach, a new setup has been recently proposed, consisting in a properly excited SRR placed in front of the aperture [11]. The physical reason behind the operation of this device is that the strong magnetic resonance of the SRR allows increasing the magnetic dipole representing the aperture [8], leading, thus, to the enhanced transmission phenomenon.

Recently, it has been shown that by placing two identical resonators at the two opposite faces of the aperture and connecting them through metallic strips [12], power extraction from the aperture can be further improved. Though any resonant element is in principle useful to achieve an efficient power transmission, sub-wavelength resonators represent the best candidates in order to keep the space occupancy of the whole structure at a minimum.

However, these setups consist of resonators that can be effectively excited by a single polarization only and, then, they cannot transmit the other polarization beyond the screen.

In this Section, we show that a new setup based on the circular-polarized electrically small antennas proposed in [13], can be used to change the polarization of a field propagating in a circular waveguide from linear to circular. The proposed setup can be considered as a linear-to-circular polarization transformer and can be used to adapt existing radiation systems to work in different environments and operate for different services.

3.1.1 DESIGN OF THE LINEAR-TO-CIRCULAR POLARIZATION TRANSFORMER

The setup presented in [12] to increase power transmission through a sub-wavelength aperture consists of a pair of SRR placed at the opposite sides of the aperture and connected through two metallic strips starting from the respective external gaps. Such a structure, however, is sensitive to a single polarization only. The SRR at the entrance face, in fact, can be effectively excited by a magnetic field directed along the axis of the resonator. Only one single polarization, thus, is allowed to pass through the aperture. The SRR on the exit face, in fact, can be seen as an electrically small resonating antenna

radiating with the same polarization of the electromagnetic field exciting the SRR at the entrance face.

Following these considerations, we may think of using efficient electrically small antennas as the ones the authors of [13] have put forward in the last decade. Replacing the SRRs with such antennas, power transmission through the aperture would be more efficient. On the other hand, while the SRR based setup presented in [12] can be used for a single polarization only, employing electrically small antennas may lead to setups working also for two orthogonal linear polarizations or even for the circular polarization.

In this regard, the MTM-inspired electrically small antennas recently presented in [13] represent good candidates. As reported in Fig. 31, in fact, we may think of using two connected and identical circularly polarized electrically small antennas placed at the two faces of a sub-wavelength aperture. As reported in [13], the two protractor elements constituting the individual electrically small antenna have slightly different dimensions in such a way to provide the proper $\pi/2$ phase-shift required to achieve the circular polarization. In the configuration proposed in [13], the two protractor elements are fed by the near field of two printed monopoles connected to a coaxial cable. In our case, instead, the two antennas are connected together, by removing the coaxial cable and extending the two monopole strips across the aperture.

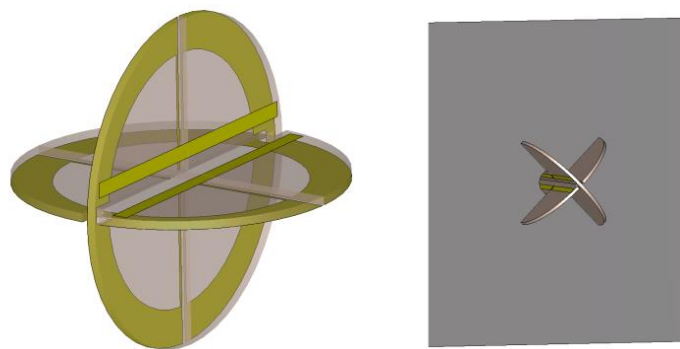


Fig. 31: 3D view of the novel resonator (left) and of the proposed polarization transformer (right).

The resulting resonator has been inserted across a circular aperture made of a metallic screen, as shown in Fig. 31 (right), to obtain a linear-to-circular polarization

transformer. In this way, a vertical or horizontal linearly polarized electromagnetic field impinging on one side of the screen can excite both the protractor elements placed at the same screen side. The extended monopoles, in turn, excite the two protractor elements placed on the other side of the screen, obtaining, thus, an emerging circularly polarized field beyond the screen.

In order to validate this idea, we have numerically simulated the behavior of the structure reported in Fig. 32, consisting of an open-ended linearly polarized rectangular waveguide (WR-650) capped with the proposed polarization transformer. The dimensions of the resonators are reported in Fig. 33.

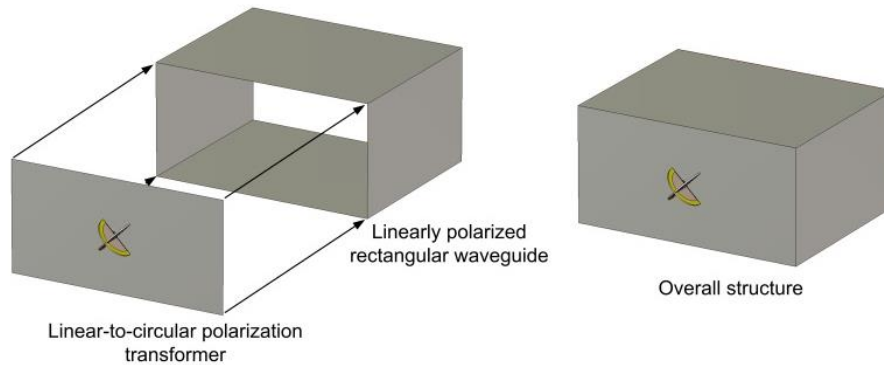


Fig. 32: Geometrical sketch of the proposed polarization transformer and its integration with a linearly polarized rectangular waveguide.

By using the full-wave simulator CST Microwave Studio [14], we have compared the matching and radiating properties of a regular open-ended rectangular waveguide, of the same waveguide capped by a metallic screen with a sub-wavelength circular aperture, and of the structure shown in Fig. 32. As reported in Fig. 34, the proposed setup exhibits a good impedance matching around the resonant frequency of the resonators and a narrower bandwidth compared to the one of a regular rectangular open-ended waveguide. Instead, as expected, the rectangular waveguide capped by a metallic screen with the sub-wavelength circular aperture is characterized by a reflection coefficient almost equal to 0 dB, due to the electrically small dimensions of the aperture.

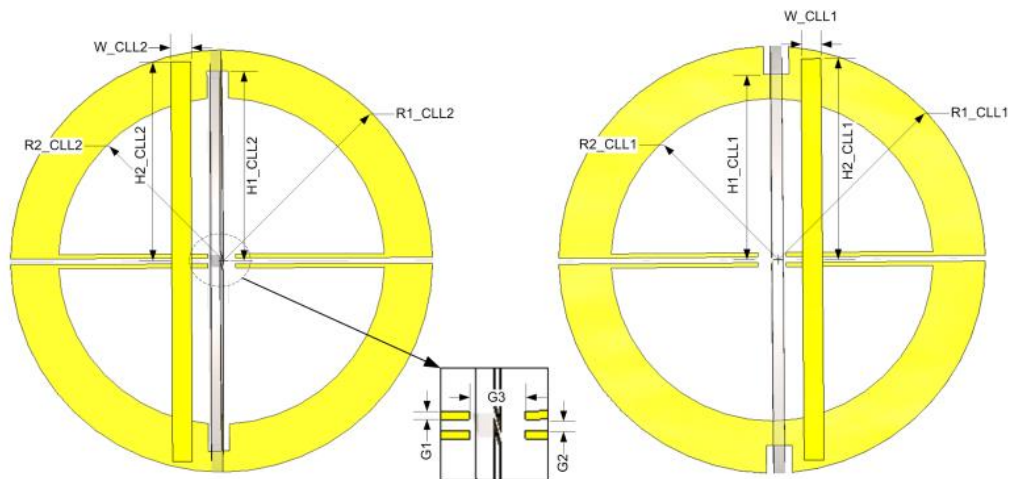


Fig. 33: Dimensions of the electrically small resonator used to design the polarization transformer: $R1_{CLL1} = R1_{CLL2} = 15$ mm, $R2_{CLL1} = 11.73$ mm, $R2_{CLL2} = 12.21$ mm, $H1_{CLL1} = 13.04$ mm, $H1_{CLL2} = 13.5$ mm, $H2_{CLL1} = 13.9$ mm, $H2_{CLL2} = 14$ mm, $W_{CLL1} = W_{CLL2} = 1.4$ mm, $G1 = 0.3$ mm, $G2 = 0.2$ mm, $G3 = 2$ mm. Metallizations are printed on the two sides of an 0.7874 mm thick Rogers Duroid 5880 dielectric slab.

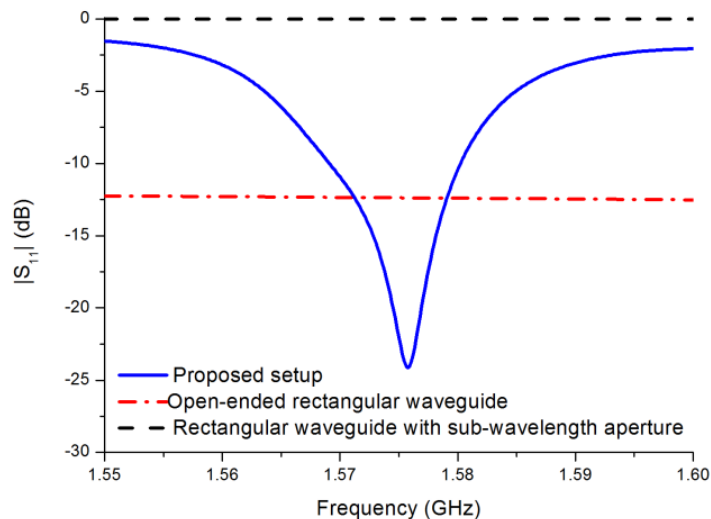


Fig. 34: Reflection coefficient of an open ended rectangular waveguide (dash-dotted line), of the same waveguide with a sub-wavelength circular aperture (dashed line), and of the structure shown in Fig. 32.

Fig. 35 and Fig. 36 show the simulated gain radiation patterns on the two principal planes at the central frequency 1.575 GHz for both polarizations. The axial ratio in the main beam direction, shown in Fig. 37, is below 3 dB at the GPS L1 frequency (1.575 GHz) with a bandwidth of about 7.5 MHz. These results confirm the effectiveness of the proposed structure to transform an impinging linear polarization into a circular one.

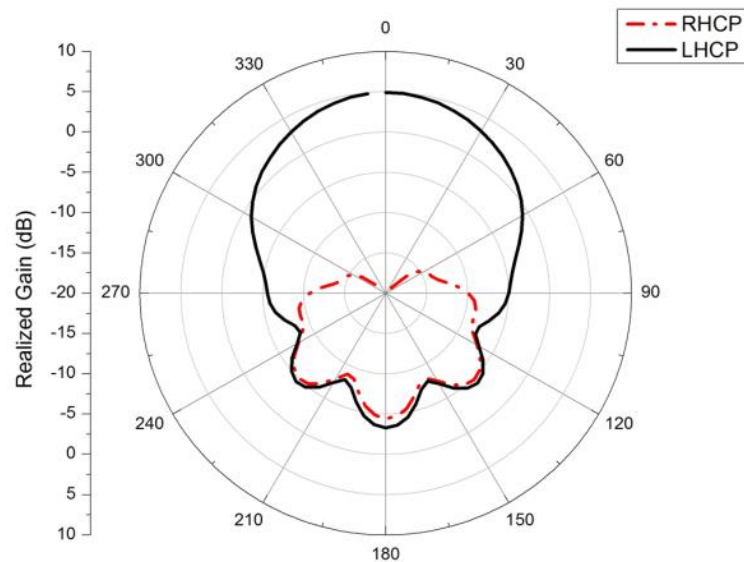


Fig. 35: Realized gain radiation patterns at 1.575 GHz of the structure shown in Fig. 32 ($\varphi = 0^\circ$).

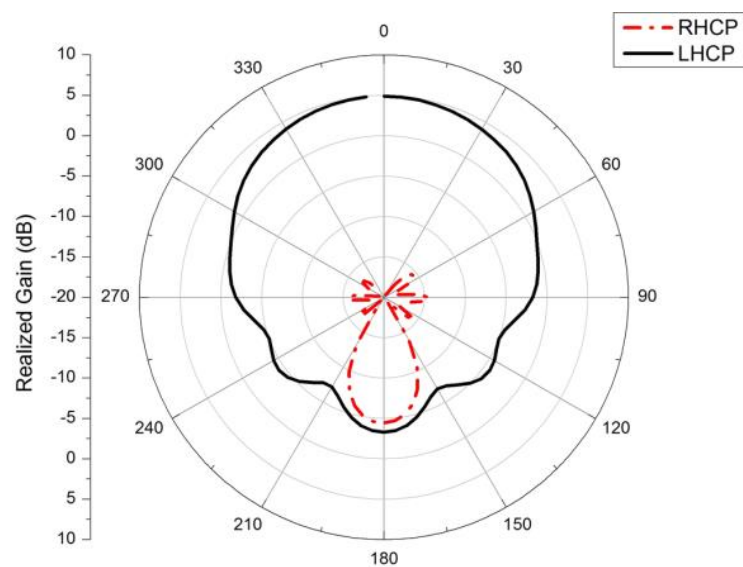


Fig. 36: Realized gain radiation patterns at 1.575 GHz of the structure shown in Fig. 32 ($\varphi = 90^\circ$).

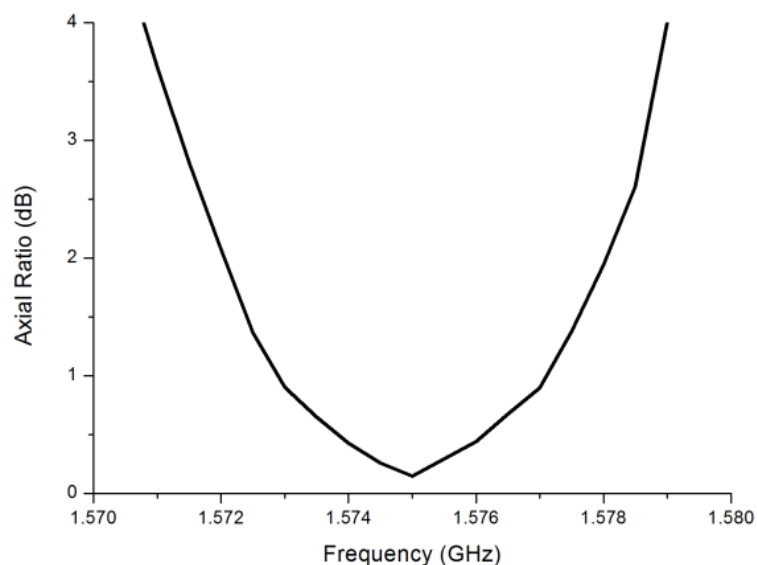


Fig. 37: Axial ratio for the main beam direction of the structure shown in Fig. 32.

3.1.2 DESIGN OF THE SELF-FILTERING CIRCULARLY POLARIZED HORN ANTENNA

In the previous Subsections we have presented a novel linear-to-circular polarization transformer based on the employment of electrically small and circularly polarized antennas. This setup, thanks to its compact size and the independence of its features from the surrounding environment, can be easily integrated in a regular radiation element to change its polarization properties. Moreover, as shown in Fig. 34, a regular waveguide capped by the proposed polarization transformer exhibits a narrow operation bandwidth that can be useful to reduce the out-of-band noise in satellite receiving systems.

In fact, in satellite receiving systems, reflector antennas (e.g. parabolas) are usually fed by a horn radiator. However, in satellite applications, the received signal is less affected by fading and flutter when circularly polarized antennas are used at each end of the link. Therefore, in order to maximize system performance, circularly polarized feeds should be used. Moreover, the bandwidth of the signals in satellite systems is usually narrower compared to the operation frequency range of a regular horn feed. Consequently, in order to reduce the amount of noise captured by the receiving system, a filtering module is usually needed.

In [3], a possible solution to reduce the operation bandwidth of a regular horn antenna based on resonant bi-omega resonators was presented. However, the used bi-omega particle inherently works for linearly polarized signals and, thus, the horns proposed in [3] cannot radiate/receive a dual linear polarization or a circular polarization.

In this Subsection, in order to obtain the two features (i.e. circular polarization and filtering behavior), we propose the design of a linear-to-circular polarization transformer, which, being a cheap and light component, can be integrated in more complex devices, without increasing their space occupancy. The proposed transformer, inspired to the setups presented in [11]-[12] and used to efficiently extract power from a sub-wavelength aperture, can be considered as an add-on tool to change the polarization properties of transmitting/radiating systems. At the same time, the proposed transformer is designed to properly work in a narrow frequency band, exhibiting filtering performances for the suppression of the out-of-band noise. Inserting this component at the throat of a regular conical horn, we show how this radiator can be fed by a rectangular waveguide working in the fundamental linearly polarized mode and can filter out the undesired noise receiving only the GPS signals at L1 band.

The proposed structure is shown in Fig. 38, and consists of a WR-650 waveguide, a regular conical horn and the proposed polarization transformer placed between the waveguide and the horn.

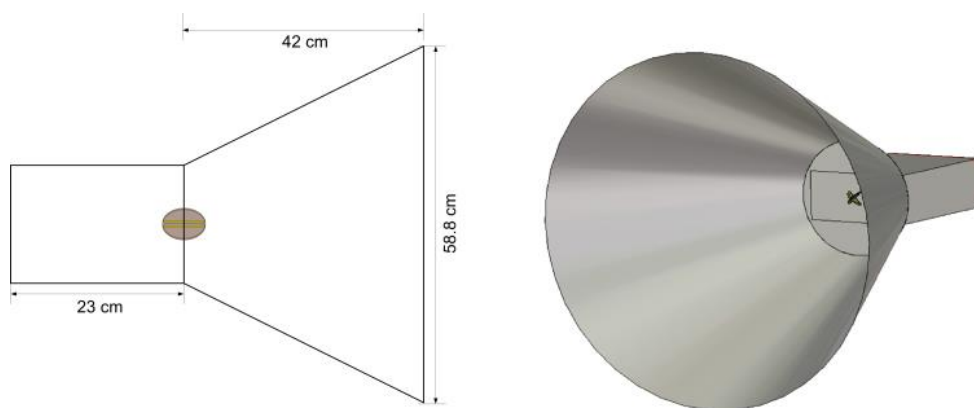


Fig. 38: Top view (left) and perspective view (right) of the self-filtering circularly polarized horn antenna.

The radiating and matching properties of this structure have been numerically evaluated by using CST Microwave Studio. The reflection coefficients as well as the axial ratio, shown in Fig. 39 and Fig. 40, respectively, are very similar to the ones presented in the previous Subsection, proving the independence of the inclusion from the environment. In fact, in order to maintain the resonant frequency around the GPS L1 frequency band, we used the following value for the inside radius of one of the protractor elements: $R2_CLL1 = 11.76$ mm; while all other dimensions of the inclusion are those given in Fig. 33. In particular, the antenna is well matched only in a narrow frequency band around the resonant frequency of the particle. In this way, the unwanted signals are directly reflected and do not reach the receiver, while the in-band signal is correctly received by the antenna.

Moreover, the plot of the axial ratio (shown in Fig. 40), which is below 3 dB in the GPS L1 frequency band, proves that the proposed antenna can be used in satellite systems requiring circular polarization. The radiation patterns on the principal planes at the central frequency of 1.575 GHz are reported in Fig. 41 and Fig. 42 and show that a left-handed circular polarized field is radiated with a maximum realized gain greater than 17 dBi.

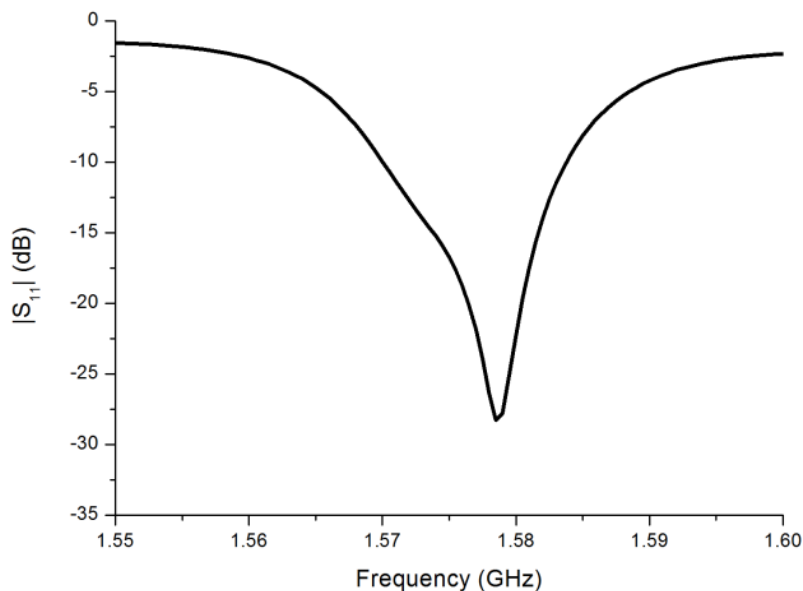


Fig. 39: Reflection coefficient of the self-filtering circularly polarized horn antenna shown in Fig. 38.

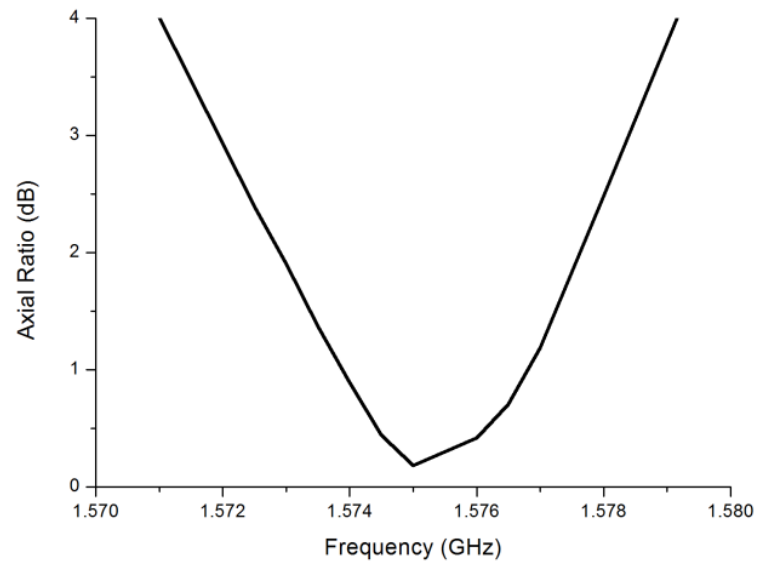


Fig. 40: Axial ratio for the main beam direction of the self-filtering circularly polarized horn antenna shown in Fig. 38.

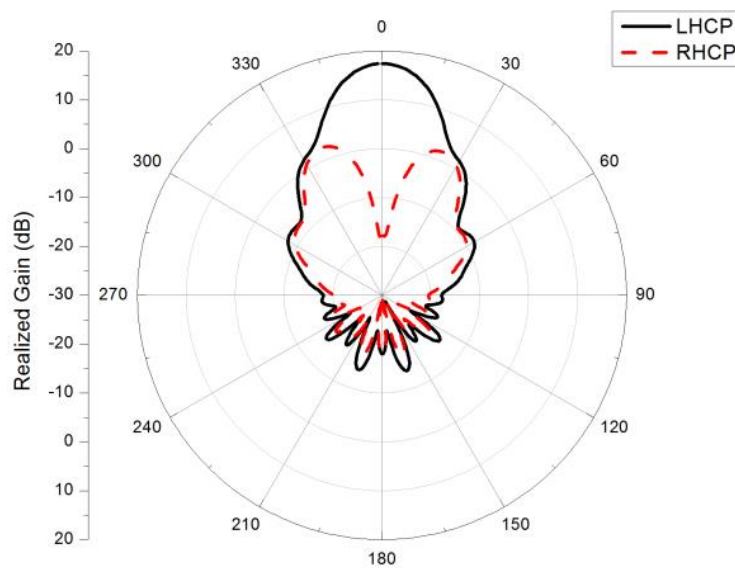


Fig. 41: Realized gain radiation patterns at 1.575 GHz of the self-filtering circularly polarized horn antenna shown in Fig. 38 ($\varphi = 0^\circ$).

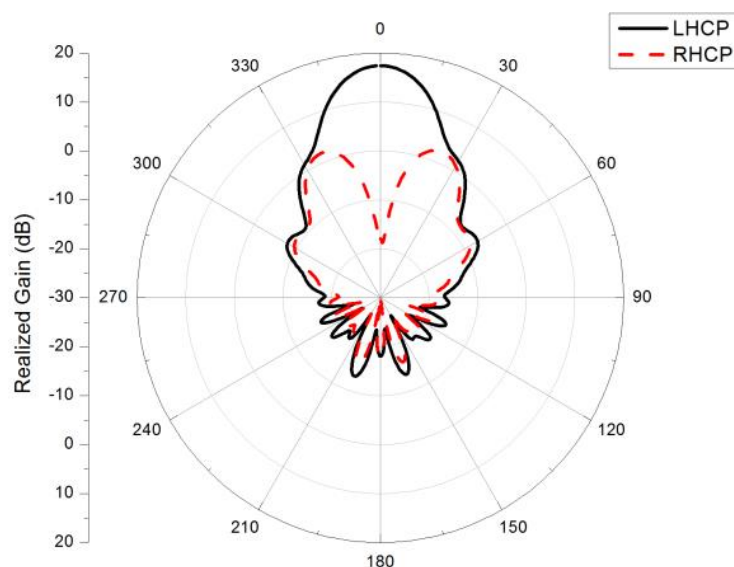


Fig. 42: Realized gain radiation patterns at 1.575 GHz of the self-filtering circularly polarized horn antenna shown in Fig. 38 ($\varphi = 90^\circ$).

3.2 A Combined Band-pass Filter and Polarization Transformer for Horn Antennas

3.2.1 DESIGN OF A PLANAR LINEAR-TO-CIRCULAR POLARIZATION TRANSFORMER

In previous Section, a linear-to-circular polarization transformer has been proposed based on the use of a MTM-inspired electrically small antenna. However, this setup is not planar, consists of different and geometrically orthogonal structures, involves the use of dielectric materials leading to an efficiency reduction, and can handle only low-power signals (i.e. the operation is limited to the receiving mode only). In order to overcome these issues, we propose here a new approach to design a planar and all-metallic polarization transformer inspired to the compact waveguide filter presented in [15] consisting of a complementary SRR drilled in a metallic sheet. However, since this resonator type inherently works for a single polarization only, in order to design a linear-to-circular polarization transformer, we need to replace it with an element showing different polarization properties.

In this regard, we propose the design of a different resonator using a complementary version of the one used in [16] to design a circularly polarized electrically small antenna. In particular, as shown in Fig. 43, we have drilled on a metallic sheet two mutually orthogonal meander-line slot dipoles. As well explained in [16], in order to obtain a circular polarization operation, the two dipoles are terminated with arrows that have slightly different dimensions in such a way that the phase shift between them is equal to $\pi/2$.

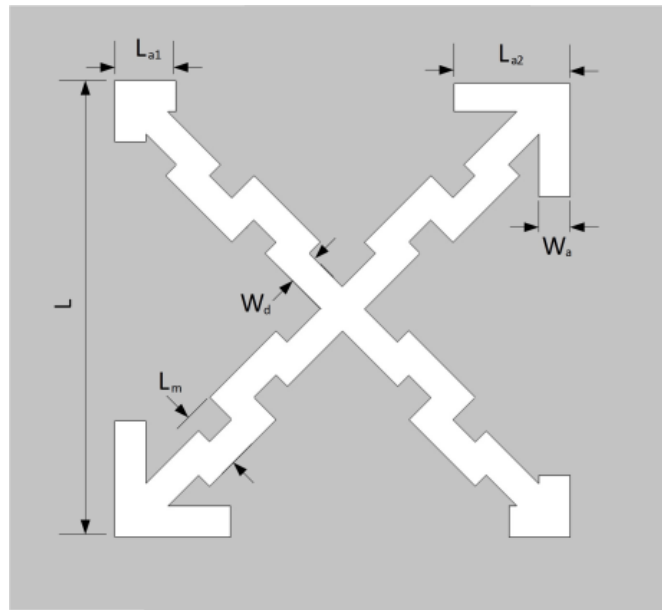


Fig. 43: Geometrical sketch of the proposed polarization transformer with dimensions: $L = 5.8$ mm, $L_{a1} = 0.3$ mm, $L_{a2} = 0.9$ mm, $L_m = 0.8$ mm, $W_d = 0.4$ mm, $W_a = 0.4$ mm.

In this way, a vertical or horizontal linearly polarized electromagnetic field impinging on one side of the screen can excite the complementary resonator etched on the screen. The two dipoles radiate on the other side of the screen, obtaining, thus, an emerging circularly polarized field beyond it.

In order to validate this idea, we have numerically simulated the behavior of the structure reported in Fig. 44, consisting of an open-ended linearly polarized rectangular waveguide (WR-62) capped with the proposed polarization transformer. The dimensions of the resonators are reported in Fig. 43.

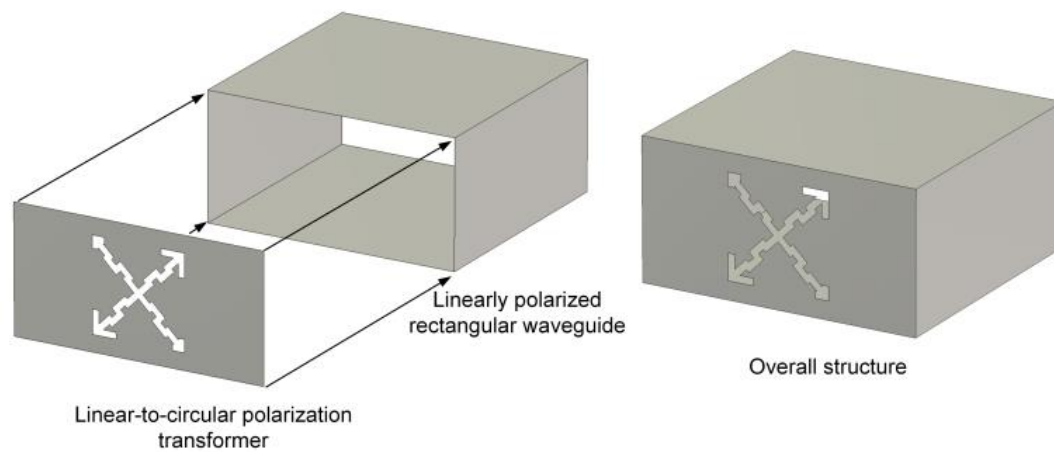


Fig. 44: Geometrical sketch of the proposed polarization transformer and its integration with a linearly polarized rectangular waveguide.

By using the full-wave simulator CST Microwave Studio, we have compared the matching and radiating properties of a regular open-ended rectangular waveguide with the ones of the structure shown in Fig 44. As shown in Fig. 45, the proposed setup exhibits a good impedance matching around the resonant frequency of the resonator and a narrower bandwidth compared to the one of a regular rectangular open-ended waveguide.

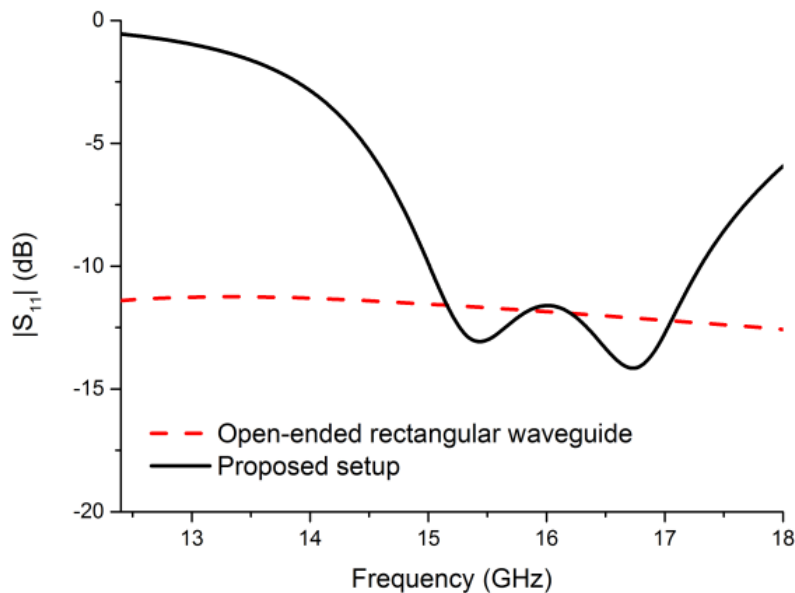


Fig. 45: Reflection coefficient amplitude of an open ended rectangular waveguide (dashed line) and of the structure shown in Fig. 44 (solid line).

Fig. 46 shows the simulated gain patterns on the two principal planes at the central frequency 15.75 GHz for both polarizations, respectively. The axial ratio in the main beam direction, shown in Fig. 47, is below 3 dB around 15.75 GHz with a bandwidth of about 625 MHz. These results confirm the effectiveness of the proposed structure to transform an impinging linear polarization into a circular one.

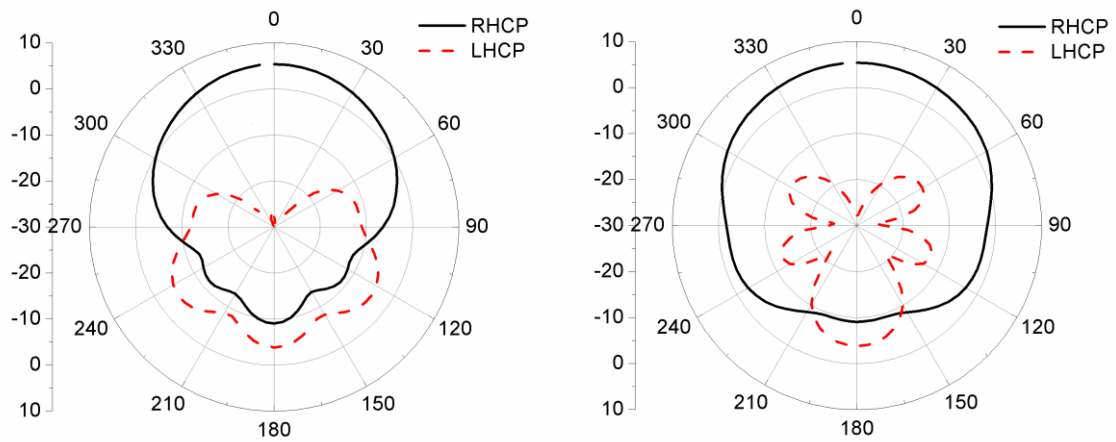


Fig. 46: Realized gain patterns at 15.75 GHz of the structure shown in Fig. 44: (left) $\varphi = 0^\circ$; (right) $\varphi = 90^\circ$.

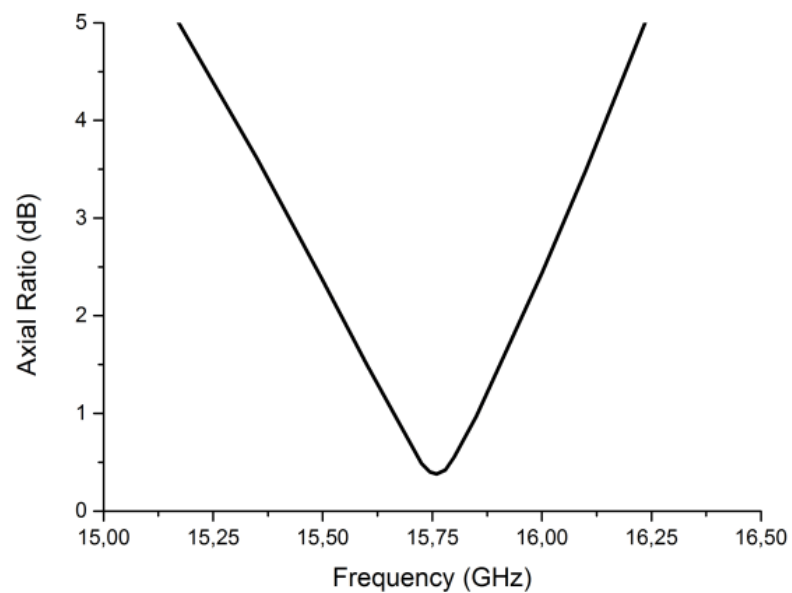


Fig. 47: Axial ratio for the main beam direction of the structure shown in Fig. 44.

3.2.2 DESIGN OF THE SELF-FILTERING CIRCULARLY POLARIZED HORN ANTENNA

In the previous Subsection, we have presented a novel linear-to-circular polarization transformer based on the employment of a complementary resonator. This setup, thanks to its compact size and the independence of its features from the surrounding environment, can be easily integrated in a regular radiation element to change its polarization properties. Moreover, as shown in Fig. 45, a regular waveguide capped by the proposed polarization transformer exhibits a narrow operation bandwidth. This feature, which is typically regarded as a limitation in most of MTM-inspired devices, can be useful to reduce the out-of-band noise in satellite receiving systems.

Exploiting this concept, we present in this section a self-filtering circularly polarized horn antenna that can be used as the feed of regular parabolas for narrowband satellite systems. The proposed structure is shown in Fig. 48, and consists of a WR-62 waveguide, a regular corrugated conical horn and the proposed polarization transformer placed between the waveguide and the horn.

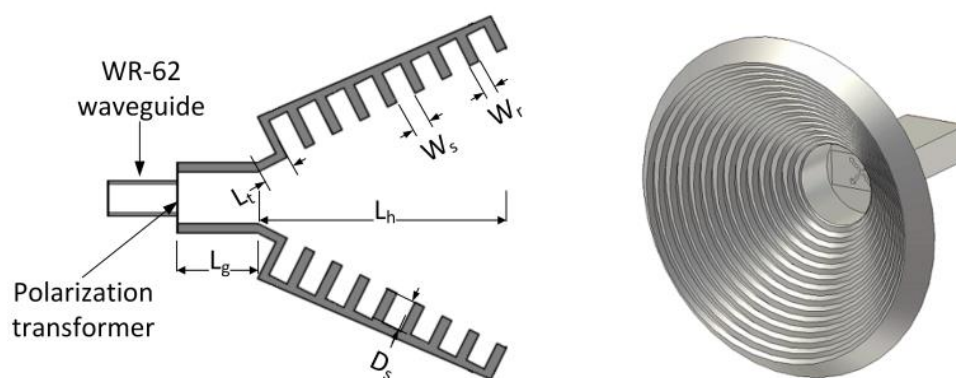


Fig. 48: Side view (left) and perspective view (right) of the filtering circularly polarized horn antenna. Corrugated horn dimensions: $D_s = 6.3$ mm, $L_g = 33$ mm, $L_h = 25.6$ mm, $L_t = 5$ mm, $W_s = 1.3$ mm, $W_r = 1.3$ mm.

The radiating and matching properties of this structure have been numerically evaluated by using CST Microwave Studio. The reflection coefficient amplitude as well as the axial ratio, shown in Figs. 49 and 50, respectively, is very similar to the ones presented in the previous Subsection, proving the independence of the inclusion from the environment. In fact, in order to maintain the AR below 3 dB, we used the following

value for the length of one of the arrows: $L_{a2} = 0.8$ mm; while all other dimensions of the inclusion are those given in Fig. 42. In particular, the antenna is well matched only in a narrow frequency band around the resonant frequency of the complementary resonator. In this way, the unwanted signals are directly reflected back and do not reach the receiver, while the in-band signal is efficiently received by the antenna.

Moreover, the plot of the axial ratio (shown in Fig. 50), which is below 3 dB around 15.85 GHz, proves that the proposed antenna can be used in satellite systems requiring circular polarization. The radiation patterns on the principal planes at the central frequency of 15.85 GHz are reported in Fig. 51 and show that a right-handed circular polarized (RHCP) field is radiated with a maximum realized gain greater than 14 dBi.

Finally, the realized gain and the directivity of the proposed horn are shown in Fig. 52 as a function of frequency. This figure confirms that, due to the mismatch introduced by the polarization transformer, the proposed setup efficiently radiates/receives only in a narrow frequency band. Please note that, compared to the self-filtering horn antennas presented in the literature, the proposed one is less complex, lighter, and less expensive. In fact, the combined band-pass filter and polarization transformer simply consists of a single metal sheet with a slot of suitable geometry.

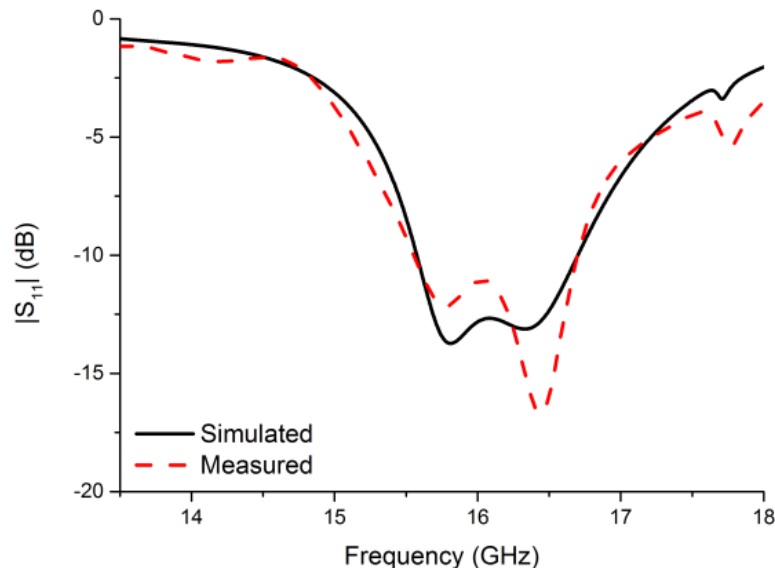


Fig. 49: Simulated and measured reflection coefficient amplitude of the self-filtering circularly polarized horn antenna shown in Fig. 48.

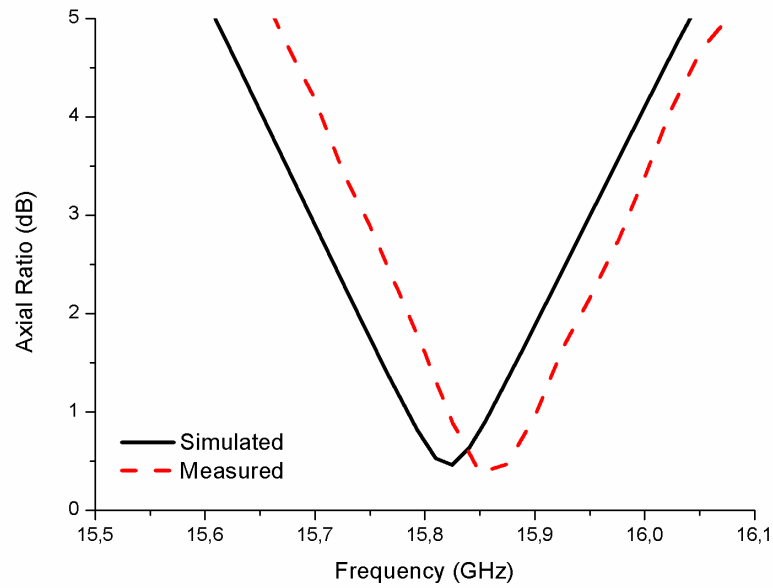


Fig. 50: Simulated and measured axial ratio for the main beam direction of the self-filtering circularly polarized horn antenna shown in Fig. 48.

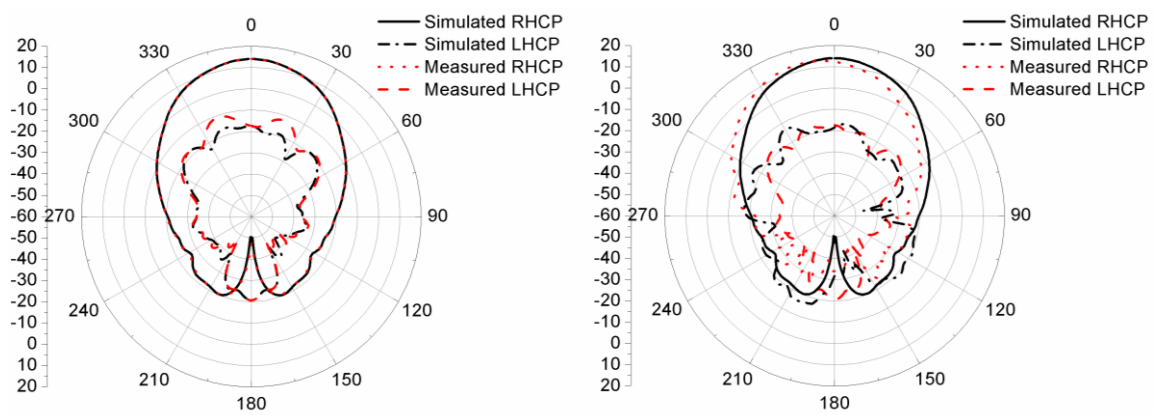


Fig. 51: Simulated and measured realized gain patterns at 15.85 GHz of the self-filtering circularly polarized horn antenna shown in Fig. 48: (left) $\phi = 0^\circ$; (right) $\phi = 90^\circ$.

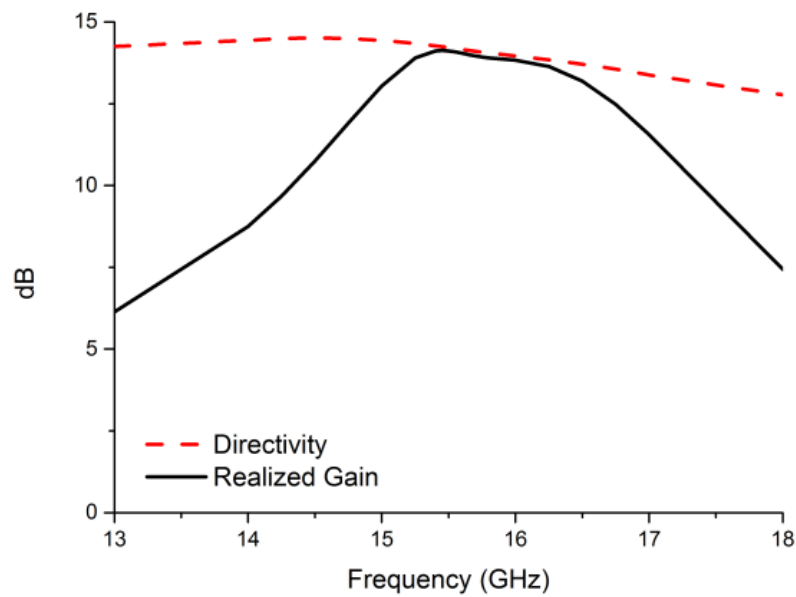


Fig. 52: Realized gain (solid line) and directivity (dashed line) of the self-filtering circularly polarized horn antenna shown in Fig. 48.

3.2.3 EXPERIMENTAL REALIZATION AND MEASUREMENTS

In order to validate the numerical results reported in the previous Subsection, we have realized the proposed polarization transformer and assembled the overall structure, as shown in Fig 53. In particular, a polarization transformer with the same dimensions reported in Subsection 2 has been realized on a 0.1 mm thick copper foil using the LPKF Protomat-S milling machine. This device has been inserted between a WR-62 coaxial-to-waveguide transition and a corrugated conical horn.

The matching and radiating properties, reported in Fig. 49 - Fig. 51, have been measured by using a vector network analyzer and the near field antenna measurement system Satimo StarLab. As predicted by the full-wave simulations, the measurements confirm that the antenna radiates a RHCP field, confirming the expected filtering behavior.

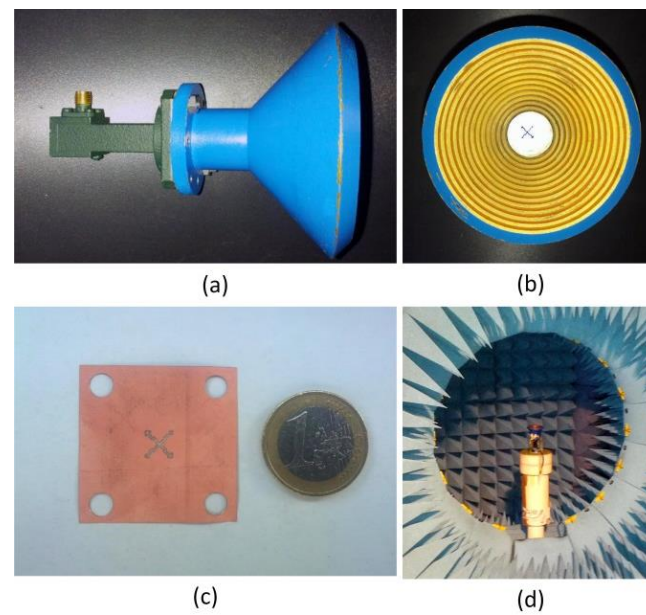


Fig. 53: Photographs showing: (a) side view of the overall antenna structure consisting of a coaxial-to-waveguide transition, the proposed polarization transformer, and a corrugated conical horn; (b) front view of the overall antenna structure; (c) the realized polarization transformer; (d) the overall antenna structure in the Satimo StarLab.

3.3 Horn Antennas with Integrated Notch Filters

Both the designs proposed in the previous Sections incorporate a band-pass filter that allows reducing the out-of-band noise. However, some wideband communication systems suffer from the interference generated by narrowband services operating in a portion of the same frequency band. In this case, a notch filter rather than a band-pass filter would be needed

In this Subsection, in order to obtain proper horn antennas with band-stop operation, we propose to use a single SRR placed inside a regular pyramidal horn. In this way, the radiating and matching properties of the overall structure are affected by the strong resonance of the SRR only around its resonant frequency – leading to a band notch – while they are almost unchanged in the rest of the operating frequency band. The dimensions of the SRR can be easily chosen to make the notched-band centered at the frequency of the interfering signal we want to suppress. Moreover, using two or more SRRs, we are able to suppress multiple interfering signals at different frequencies.

3.3.1 DESIGN OF A HORN FILTENNA WITH A SINGLE-BAND-STOP CHARACTERISTIC

3.3.1.1 Overview of the proposed structure

In the previous Sections, exploiting the inherent narrow bandwidth of MTM-inspired resonators, we have proposed radiating elements exhibiting a self-filtering behavior. However, as both approaches involve the insertion of a metallic screen orthogonal to the propagation direction of the electromagnetic field, they can be used only for microwave components exhibiting a band-pass behavior. The series resonance linked to the presence of connected electrically small antennas or complementary resonators, in fact, allows a complete transmission of the energy through the metallic screen in a narrow frequency band centered at the resonant frequency of the resonating structure.

In order to design a horn filtenna with band-stop characteristic, thus, we need to remove the metallic screen and design a proper resonant inclusion that stores/dissipates energy at a given frequency, leading to a band-notch in a narrow frequency range.

For this purpose, we have chosen the SRR that, due to its strong magnetic resonance, can significantly affects the antenna matching properties only around its resonant frequency, while at the other frequencies it weakly interacts with the electromagnetic field inside the horn, without affecting the radiating and matching properties of the overall system.

The entire structure, shown in Fig. 54, consists of a WR-90 waveguide (whose operating frequency range is 8.2 – 12.4 GHz), a regular pyramidal horn and the proposed filtering module. The latter consists of a SRR etched on one side of a Rogers DuroidTM RT5870 ($\epsilon_r = 2.33$, $\tan \delta = 0.0012$) dielectric substrate with a thickness of 0.787 mm. Following the design in [17], the dimensions of the SRR are properly chosen to obtain a resonant frequency at 10 GHz. In particular, the metallization and the capacitive gaps have a width of 0.5 mm, while all the other dimensions are reported in Fig. 54. Please note that the dielectric substrate has been properly shaped in order to facilitate the placement of the filter inside the horn antenna at the appropriate position.

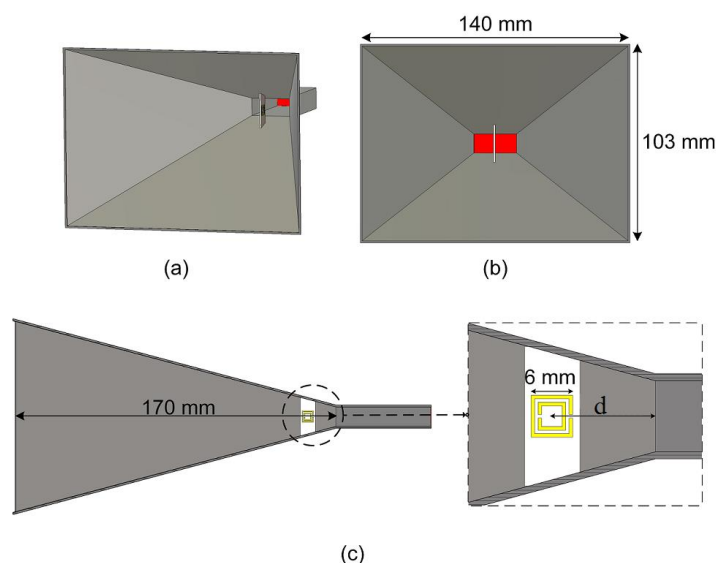


Fig. 54: Geometrical sketch of the proposed horn antenna with the notched-band filter:
 (a) perspective view; (b) front view; (c) side view.

3.3.1.2 Simulation results

The design of the proposed antenna has been carried out by using the full-wave simulator CST Microwave Studio. Considering the field distribution of the fundamental mode travelling through the waveguide and the horn, we expect that the frequency position of the notched-band depends mainly on the SRR dimensions and the relative permittivity of the dielectric substrate where the resonator is printed on. On the other hand, we expect that the distance d between the center of the resonator and the throat of the horn influences the magnitude of the reflection/transmission. In fact, when the SRR is further away from the throat of the horn, it intercepts a progressively lower portion of the impinging power and, thus, the expected reflection at the resonance is progressively lower. These expectations are confirmed by the graphs reported in Fig. 55 showing the frequency variation of the reflection coefficient amplitude at the input port for different values of d . The position of the reflection peak is quite stable with the variation of the distance d , while the amplitude of the peak is lower for larger values of d . In addition, we note that if the SRR is too close to the throat, due to the reactive effects of the discontinuity waveguide-horn, the amplitude of the reflection coefficient is higher in the whole monomodal operation frequency of the horn. Therefore, in order to make a wise

design, we have chosen the distance $d = 15$ mm, which guarantees a strong mismatch in the notched-band and a good impedance matching in the rest of the frequency band. In this way, as reported in Fig. 56, the performance of the horn with and without the filtering module is similar over the whole frequency range, except for the notched part.

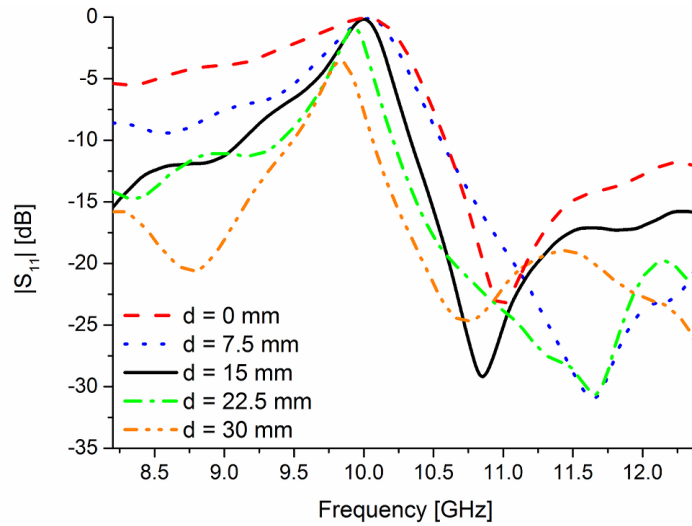


Fig. 55: Reflection coefficient amplitude at the input port of the structure shown in Fig. 54 for different positions of the SRR.

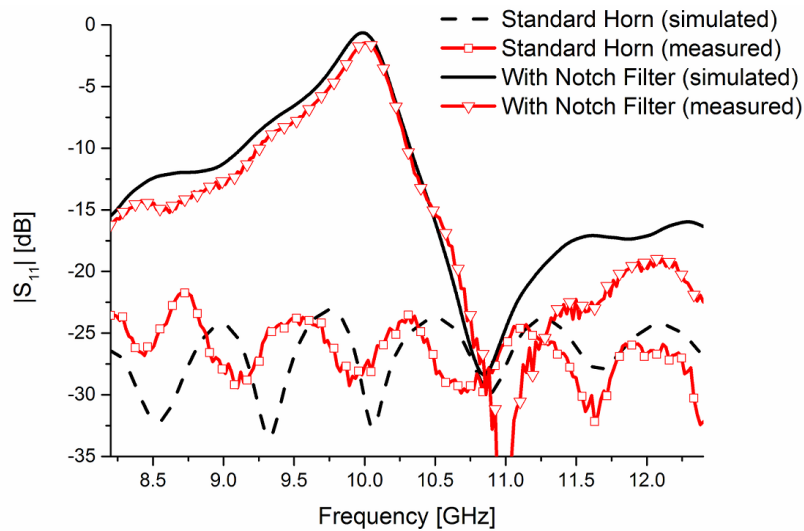


Fig. 56: Measured and simulated reflection coefficient amplitude at the input port of the structure shown in Fig. 54 for the case of $d = 15$ mm.

The expected filtering behavior of the proposed structure is also confirmed by the values of the broadside gain shown in Fig. 57 and Fig. 58. As expected, in fact, the realized gain is very low within a narrow frequency band around 10 GHz, due to the strong excitation of the SRR. An interfering signal falling in the same frequency range, thus, would not affect the performance of the receiver. On the contrary, in the rest of the frequency band, the radiating properties of the proposed structure are almost identical to the ones of the regular horn.

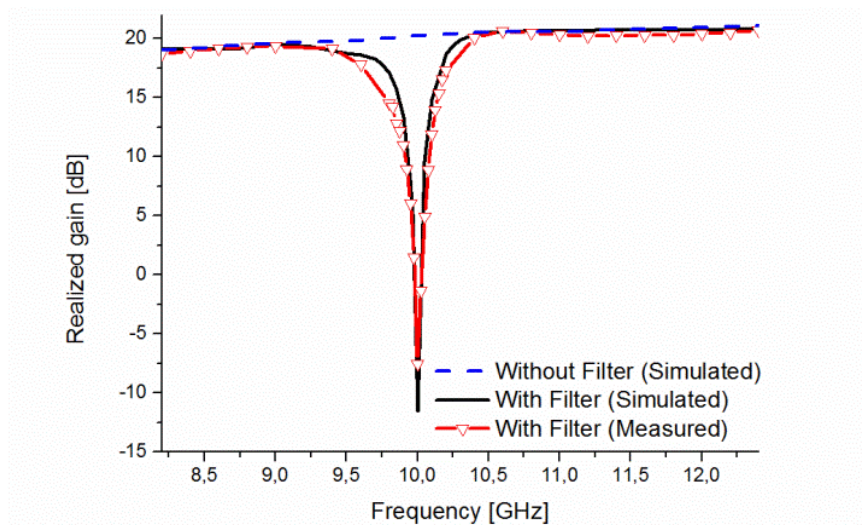


Fig. 57: Measured and simulated realized gain in the main beam direction of the proposed horn antenna with the notched-band filter and of the corresponding standard horn antenna.

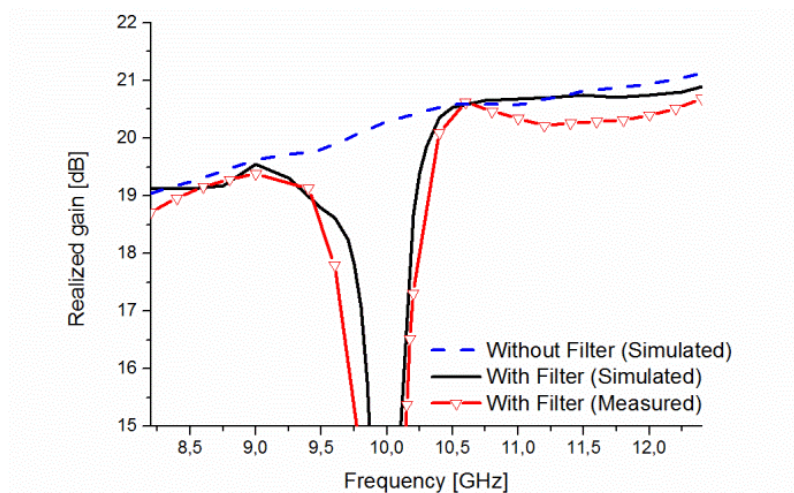


Fig. 58: Close-up of Fig. 57.

In Fig. 59, we also show the realized gain patterns at three sample frequencies. These results confirm that, at 10 GHz, the field is not simply deviated from the broadside direction, but is, indeed, not radiated by the antenna.

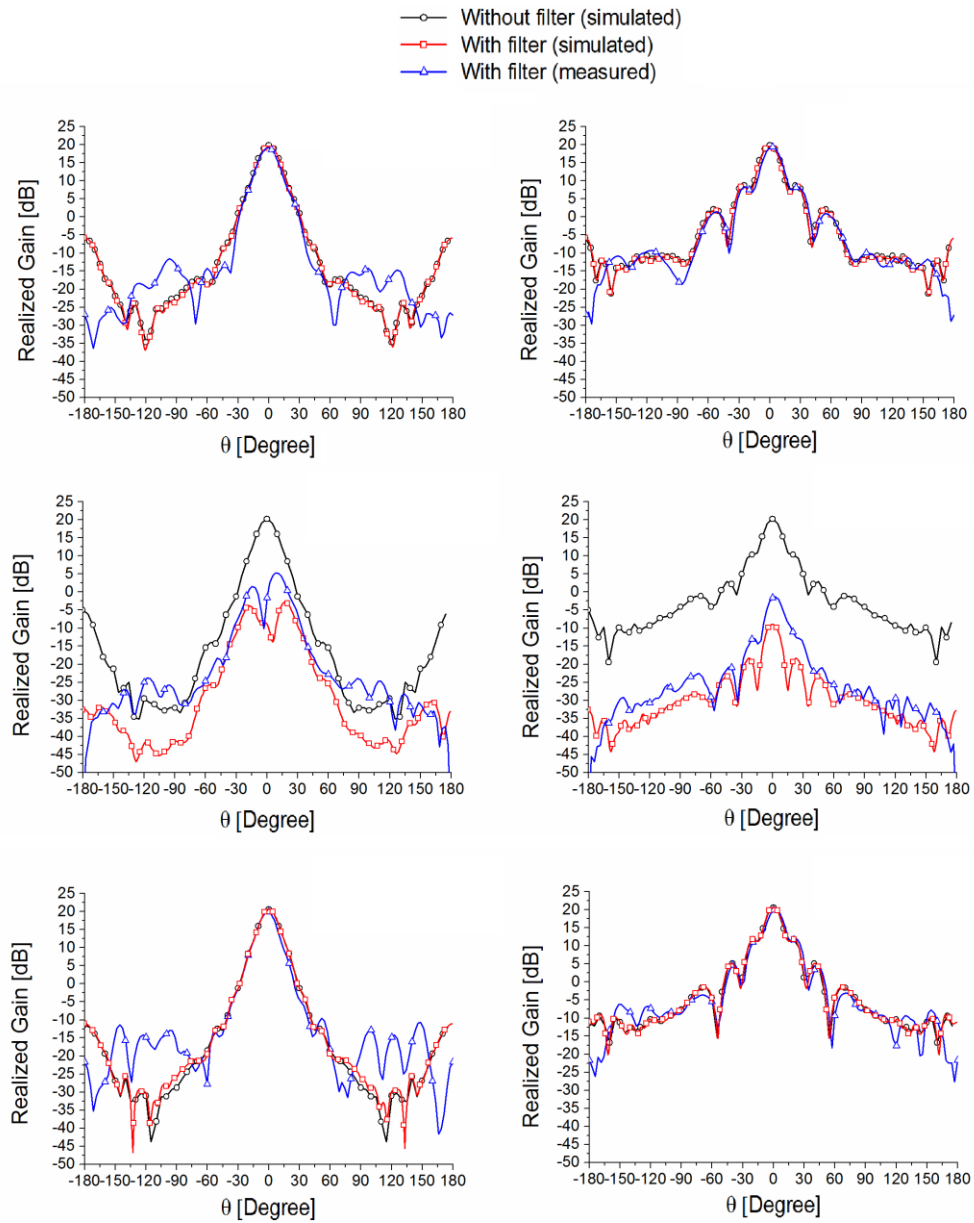


Fig. 59: Simulated and measured realized gain patterns of the proposed horn antenna with and without the notched-band filter on the E-plane (left column) and H-plane (right column) at: (first line) 9 GHz, (second line) 10 GHz and (third line) 11 GHz.

3.3.2 DESIGN OF A HORN FILTENNA WITH A DUAL-BAND-STOP CHARACTERISTIC

By properly designing and positioning a single SRR inside a horn antenna we can obtain a filtenna with a notched-band characteristic. However, many wideband communication systems require more than one notched-band. In order to obtain a horn filtenna with a dual-band behavior, we have etched two SRRs with slightly different dimensions on the same Rogers DuroidTM RT5870 substrate (see Fig. 60) in order to have two almost independent resonant frequencies at 9.25 GHz and 10.75 GHz. The main geometrical dimensions of the structure are reported in Fig 60.

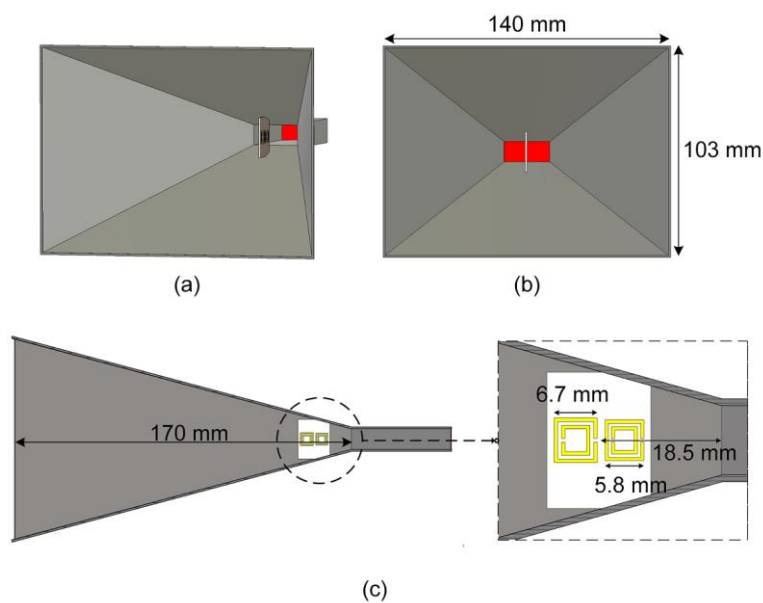


Fig. 60: Geometrical sketch of the proposed horn antenna with the dual-band-notch filter: (a) perspective view; (b) front view; (c) side view.

The simulated results of the matching (i.e. magnitude of the reflection coefficient at the input port) and radiating (i.e. broadside realized gain) properties of the dual-band structure, reported in Figs. 61-63, respectively, confirm the expectations.

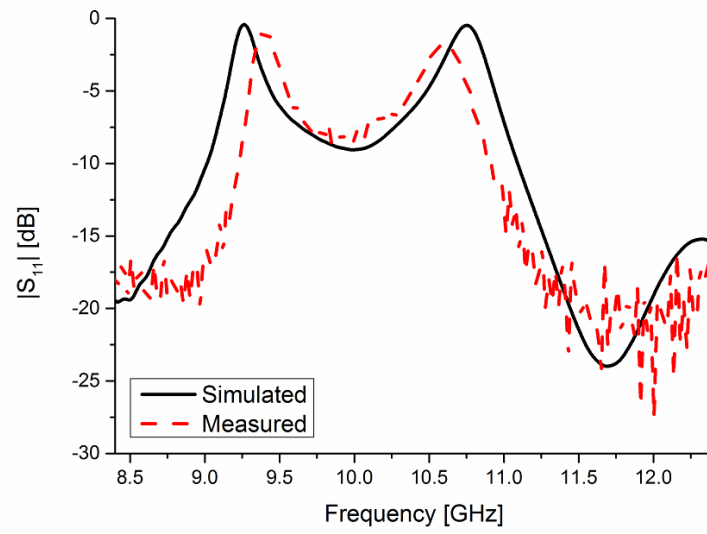


Fig. 61: Simulated and measured reflection coefficient amplitude at the input port of the horn filtenna with a dual band-stop characteristic.

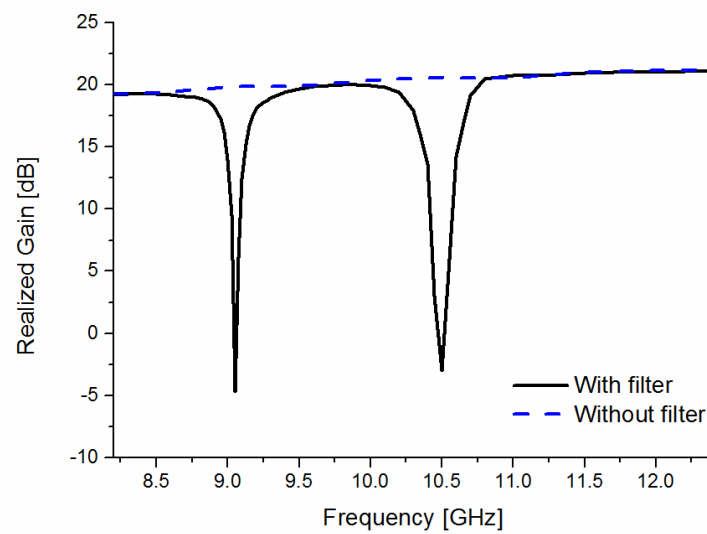


Fig. 62: Simulated realized gain in the main beam direction of the horn antenna with and without a dual-band-stop filter.

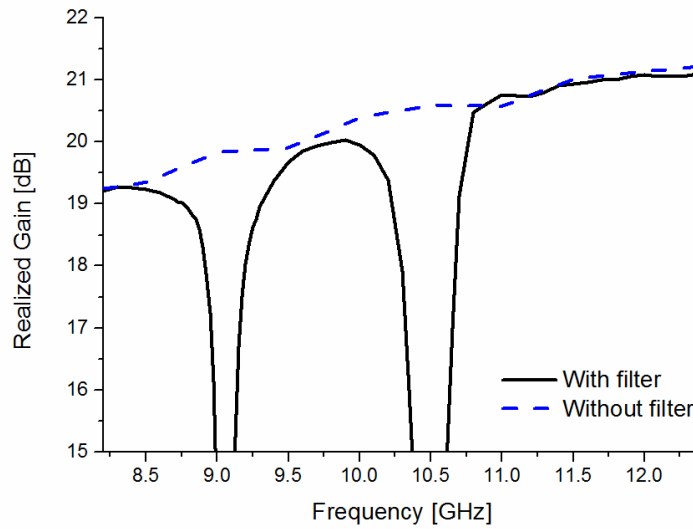


Fig. 63: Close-up of the simulated realized gain in the main beam direction of the horn antenna with and without a dual-band-stop filter.

3.3.3 EXPERIMENTAL REALIZATION AND MEASUREMENTS

In order to validate the proposed approach, the single-band filtering module shown in Fig. 54 has been manufactured with a LPKF Protomat-S milling machine. As shown in Fig. 64, the overall structure has been assembled by using standard foam to properly fix the SRR inside the horn. Finally, the performances of the radiating element have been tested by using a vector network analyzer and a near-field antenna measurement system.

As shown in Fig. 56, the measured amplitude of the reflection coefficient at the input port is in a good agreement with the simulated one. In particular, the antenna has a maximum mismatch at around 10 GHz, while in the rest of the operating bandwidth it exhibits a good impedance matching. The measured realized gain, reported in Fig. 57-58, has the same behavior of the simulated one, showing a minimum of -8 dB at around 10 GHz. In addition, the measured realized gain patterns, shown in Fig. 59, are again in a very good agreement with the simulated one, confirming the effectiveness of the proposed approach.

As a further verification of the previous results, we have also measured the transmission parameters of the setup shown in Fig. 65, where we have used the proposed filtering horn antenna and a standard horn antenna placed at a distance of 60 cm. As shown in Fig. 66, in this case we have a deep minimum of the transmission

coefficients at around 10 GHz that, compared to the case of two standard horn antennas, confirms the filtering behavior enabled by the SRR. Moreover, by using two identical versions of the proposed antenna placed again at a distance of 60 cm, we have obtained a further reduction of the transmission due to the filtering behavior of both antennas.

Finally, we have also fabricated and measured the dual-band version simulated in Section 3. In particular, we have measured the reflection coefficient of the overall structure, reported in Fig. 61, which is, again, in a good agreement with the simulated one, confirming the dual-band behavior of the filtering module. These results confirm that, if properly designed, SRRs can be easily integrated inside a standard horn antenna to introduce notched-bands inside the operating bandwidth of the horn itself, without significantly increasing weight, cost, and space occupancy of the overall structure.

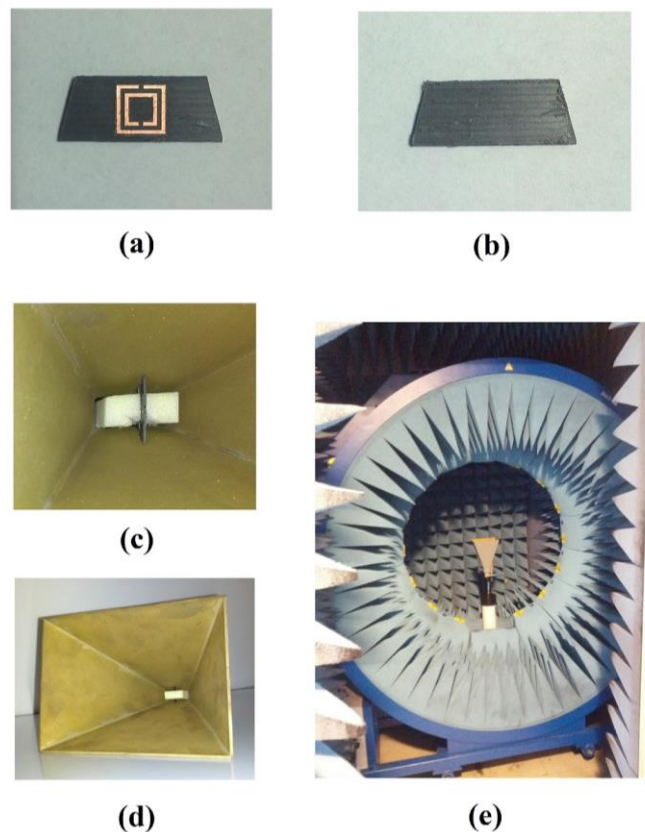


Fig. 64: Photographs showing: top (a) and bottom (b) views of the realized filtering module; (c) the filtering module fixed in the horn antenna; (d) perspective view of the proposed self-filtering horn antenna; (e) the proposed structure placed inside the near-filed measurement system.

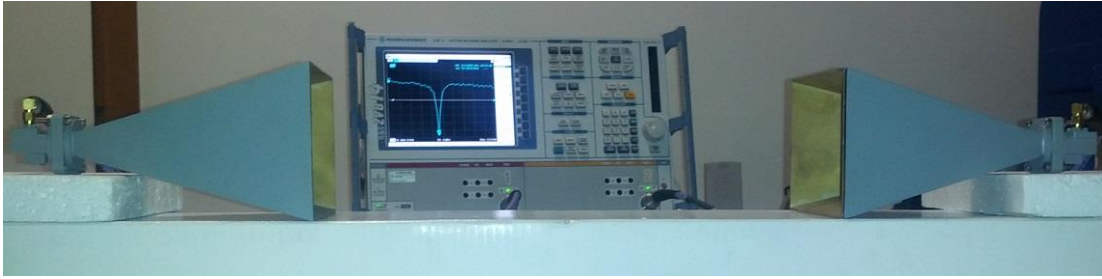


Fig. 65: Photographs showing the transmission measurement setup.

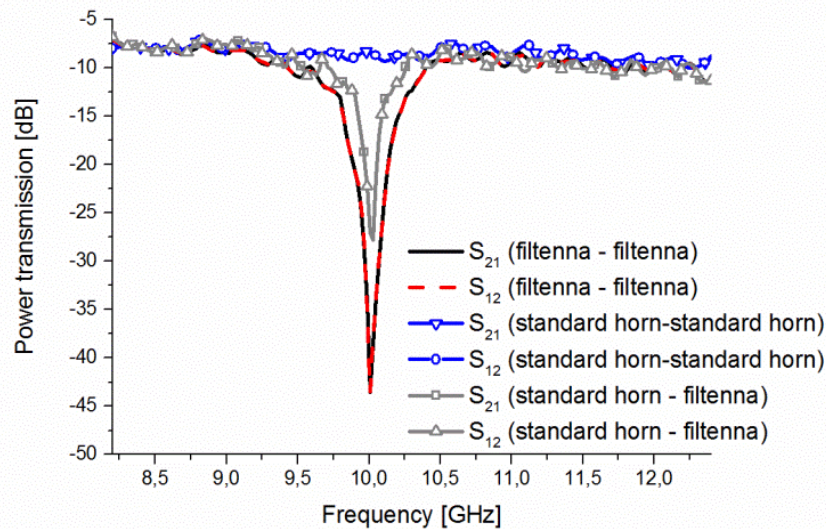


Fig. 66: Power transmission between two single-band filtering horn antennas, two standard horns and between a standard horn and the single-band filtering horn antenna, in the setup shown in Fig. 65.

3.4 Summary

In this Chapter, we have presented a novel class of horn antennas that also performs filtering operations. At first, we have designed and numerically simulated a linear-to-circular polarization transformer based on the employment of electrically small antennas. Specifically, it consists of a sub-wavelength aperture drilled in a metallic screen and a pair of electrically small resonators obtained by connecting together two identical circularly polarized electrically small protractor antennas. This structure has

been used to cap an open-ended rectangular waveguide, in order to prove its effectiveness in transforming the linear polarization of the waveguide into a circular one. The same polarization transformer can be successfully used to design a self-filtering and circularly polarized horn antenna. In particular, we have inserted the proposed polarization transformer at the section connecting a WR-650 waveguide and a conical horn. By using CST Microwave Studio, we have numerically demonstrated that the overall structure radiates a left-handed circularly polarized electromagnetic field with a maximum realized gain greater than 17 dBi. Moreover, the reflection coefficient is below -10 dB only in a narrow frequency band around the resonant frequency of the resonating particle, which mainly depends on the particle dimensions.

Then, we have presented a circular polarized (CP) filtering antenna consisting of a regular conical horn and a planar and all metallic polarization transformer. The proposed linear-to-circular polarization transformer is obtained by using complementary electrically small resonators etched on a metallic sheet. This structure behaves both as a polarization transformer and a filter allowing to reduce the impedance bandwidth of the conical horn to avoid additional noise in satellite receiving systems. The proposed antenna, operating at X-band, exhibits a CP realized gain of 17.5 dBic.

Finally, we have proposed the design of filtering horn antennas with band-stop characteristics obtained through the use of electrically small magnetic resonators. In particular, a SRR etched on a Rogers DuroidTM RT5870 dielectric substrate is inserted within the metallic flare of the horn at a proper distance from the throat. At around the resonant frequency of the SRR transmission is highly reduced and a single notched-band is obtained. In order to extend the result to dual-band operation, we have also presented the design of the filtering module made by two SRRs with different dimensions.

The validity of the proposed approach is verified through proper sets of full-wave simulations and experiments on fabricated prototypes. The obtained results prove that the proposed antenna can be employed in receiver front-ends of satellite systems to remove the necessity of external filtering modules. Moreover, we remark here that the proposed radiators can be employed in communication platforms, where structural and cost constraints require strong integration of different components. The proposed

modules, in fact, allow for a dramatic reduction of the interfering signal power, besides having advantages such as reduced cost, weight, and space occupancy. Finally, the filtering modules can be thought of as a simple add-on to be designed and inserted into already operating horn antennas to suppress interference, when needed.

3.5 References

- [1] B. Froppier, Y. Mahe, E.M. Cruz, and S. Toutain, "Design of a filtering antenna: application to the electromagnetic horn," in *IEEE AP-S Symp. Digest*, Jun. 2003, vol. 2, pp. 1173-1176.
- [2] G.Q. Luo, W. Hong, H.J. Tang, J.X. Chen, X.X. Yin, Z.Q. Kuai, and K. Wu, "Filtenna consisting of horn antenna and substrate integrated waveguide cavity FSS," *IEEE Trans. Antennas Propagat.*, vol. 55, pp. 92-98, 2007.
- [3] F. Bilotti, L. Di Palma, D. Ramaccia, and A. Toscano, "Self-filtering low-noise horn antenna for satellite applications," *IEEE Antennas Wireless Propag. Lett.*, vol. 11, pp. 354-357, 2012.
- [4] C. Yu, W. Hong, Z. Kuai, and H. Wang, "Ku-band linearly polarized omnidirectional planar filtenna," *IEEE Antennas Wireless Propag. Lett.*, vol. 11, pp. 310-313, 2012.
- [5] X. Chen, F. Zhao, L. Yan, and W. Zhang, "A compact filtering antenna with flat gain response within the passband," *IEEE Antennas Wireless Propag. Lett.*, vol. 12, pp. 857-860, 2013.
- [6] M. Naser-Moghadasi, R.A. Sadeghzadeh, T. Sedghi, T. Aribi, and B.S. Virdee, "UWB CPW-fed fractal patch antenna with band-notched function employing folded t-shaped element," *IEEE Antennas Wireless Propag. Lett.*, vol. 12, pp. 504-507, 2013.
- [7] J.Y. Siddiqui, C. Saha, and Y. M.M. Antar, "Compact SRR loaded UWB circular monopole antenna with frequency notch characteristics," *IEEE Trans. Antennas Propagat.*, vol. 62, pp. 4015-4020, 2014.
- [8] H. A. Bethe, "Theory of diffraction by small holes," *Phys. Rev.*, vol. 66, pp. 163-182, 1944.
- [9] D. E. Grupp, H. J. Lezec, T. Thio, and T. W. Ebbesen, "Beyond the Bethe limit: tunable enhanced light transmission through a single sub-wavelength aperture," *Adv. Mat.*, vol. 11, pp. 860-862, 1999.
- [10] A. Alù, F. Bilotti, N. Engheta, and L. Vegni, "Metamaterial covers over a small aperture," *IEEE Trans. Antennas Propagat.*, vol. 54, pp. 1632-1643, 2006.
- [11] K. Aydin, A.O. Cakmak, L. Sahin, Z. Li, F. Bilotti, L. Vegni, and E. Ozbay, "Splitting-resonator-coupled enhanced transmission through a single subwavelength aperture," *Phys. Rev. Lett.*, vol. 102, pp. 013904-1-4, 2009.

-
- [12] D. Ates, A.O. Cakmak, E. Colak, R. Zhao, C.M. Soukoulis, and E. Ozbay, "Transmission enhancement through deep sub-wavelength apertures using connected split-ring resonators," *Opt. Expr.*, vol. 18, 3952, 2010.
- [13] P. Jin, and R.W. Ziolkowski, "Multi-frequency, linear and circular polarized, metamaterial-inspired, near-field resonant parasitic antennas", *IEEE Trans. Antennas Propagat.*, vol. 59, pp. 1446-1459, 2011.
- [14] CST Studio Suite 2012, CST Computer Simulation Technology AG, Available at: www.cst.com.
- [15] N. Ortiz, J. D. Baena, M. Beruete, F. Falcone, M.A.G. Laso, T. Lopetegi, R. Marqués, F. Martin, J. Garcia-Garcia, and M. Sorolla "Complementary split-ring resonator for compact waveguide filter design," *Microw. Opt. Techn. Lett.*, vol. 46, pp. 88–92, 2005.
- [16] P. Jin, C.C. Lin, and R.W. Ziolkowski, "Multifunctional, electrically small, planar near-field resonant parasitic antennas," *IEEE Antennas Wireless Propag. Lett.*, vol. 11, pp. 200-204, 2012.
- [17] F. Bilotti, A. Toscano, L. Vegni, K. Aydin, K. B. Alici, and E. Ozbay, "Equivalent-circuit models for the design of metamaterials based on artificialmagnetic inclusions," *IEEE Trans. Microw. Theory Tech.*, vol. 55, no. 12, pp. 2865–2873, Dec. 2007.

Chapter 4

Novel MTM-inspired microwave components

Since metamaterials were proposed and experimentally realized, there has been an increasing interest in using their unique properties to improve the performances of standard microwave components. In this regard, in the previous Chapters MTM concept has been used to design several components with interesting properties. Although these components are different from each other and use the concept of MTM in a different manner, they are characterized by all being radiating elements. In this Chapter, we focus instead our attention on non-radiative elements such as transmissive microwave components and absorbers.

First, we present a new class of waveguide components based on the use of complementary electrically small resonators etched on metallic sheets. In particular, we propose a rectangular-to-circular waveguide transition that allows to effectively match waveguides with different cross-sections and to transform the linearly polarized TE_{10} -mode of a rectangular waveguide into a circularly polarized TE_{11} -mode of a circular waveguide. Moreover, using similar structures, we present the design of two power dividers and of an orthomode transducer. All these components, employing only thin metallic sheets with properly shaped slits, can be integrated in waveguide transmission systems without increasing their space occupancy.

Then, we propose a novel and low-cost metamaterial-inspired absorber operating in X-band. It consists of a single resistive sheet properly spaced from a double-ring based metasurface. Its operation principle is similar to the one of a Salisbury screen, in which a $377 \Omega/\text{sq}$ resistive sheet is placed $\lambda/4$ apart from a metal plate. In our configuration, however, the metasurface replaces the metallic backing significantly reducing the used

percentage of metal. This is very convenient when the absorber is used to reduce the RCS of non-metallic objects. In this scenario, the absence of a metal ground plane allows a significant weight reduction and a smaller increase of the object RCS outside the operating band of the absorber. Moreover, we propose a simple and low-cost technique for realizing the resistive sheet. Our approach, requiring only easy-to-find and inexpensive materials, consists in the deposition of graphite powder on ultrathin plastic sheet substrates. By controlling the deposition time and the mass of the deposited powder, we show that it is possible to realize resistive sheets exhibiting a desired surface resistance in a wide range of values.

4.1 Novel Waveguide Components based on Complementary Electrically Small Resonators

A large number of antennas and microstrip components has been already realized by using volumetric and transmission line metamaterials [1]-[6], or by properly loading conventional structures with MTM-inspired resonators [7]-[9]. In particular, several new microstrip components (filters, phase shifters, couplers, duplexer, etc.) have been introduced [10] that, thanks to the use of MTM concepts, exhibit unique properties, such as compactness, multi-functionality, multi-band behavior, etc.

While these results have been extensively obtained in microstrip technology, little efforts have been devoted to the implementation of similar concepts in the context of metallic waveguides, where only recently some interesting applications have been proposed. For instance, in [11], a possible solution to design a compact waveguide filter based on a complementary split-ring resonator drilled in a metallic sheet has been presented. Moreover, exploiting the frequency selective power transmission of bi-omega particles placed at the junction sections of different waveguides, our group has recently proposed a waveguide diplexer [12] and a balanced and an unbalanced waveguide power splitter [13].

In this Section, replacing the bi-omega particles with complementary electrically small resonators, we generalize this approach to the use of circular waveguides working in circular polarization. In particular, we first introduce a rectangular-to-circular

waveguide transition and, then, we use a similar structure to design a power divider that equally splits the input power into two circularly polarized (CP) modes at the output ports. Finally, we also propose the design of a novel orthomode transducer that can be useful in dual-polarized antennas or in diplexing systems based on the use of orthogonal polarization.

The structure of the Section is as follows. In Subsection 2, we present the design and the simulated results of the rectangular-to-circular waveguide transition that allows transforming the linearly polarized TE_{10} -mode of the rectangular waveguide into a CP TE_{11} -mode in the circular waveguide. In Subsection 3, we use a similar structure to design a waveguide power divider that equally splits power from a rectangular waveguide input port to two output ports. In particular, two different configurations characterized by either linear or CP fields at the output ports will be presented. Then, in Subsection 4, we present the design of an orthomode transducer based on the same concepts.

4.1.1 DESIGN OF A RECTANGULAR-TO-CIRCULAR WAVEGUIDE TRANSITION

In the previous Chapter, we have presented a CP filtering horn antenna based on the use of a complementary electrically small resonator. This radiator consists of a standard horn antenna in which we have inserted a MTM-inspired resonator drilled in a metallic sheet. This structure, exploiting its geometrical features and the inherent narrow bandwidth of MTM-inspired components, allows radiating only in a narrow frequency band and transforming the linear polarization of a rectangular waveguide into a CP radiated field.

Using a similar structure, we propose here to design a waveguide transition that allows connecting waveguide ports with different cross-sections. This kind of structure can be useful in satellite systems where horn and reflector antennas are typically fed by circular waveguides, while rectangular waveguides are preferred for connecting the radiating elements to the remaining receiving/transmitting circuitry.

In particular, we have placed the complementary resonator reported in Fig. 67 between a WR-90 waveguide and a standard circular waveguide, as shown in Fig. 68. In this

way, we expect that the two meandered dipoles of the complementary resonator convert the TE_{10} -mode of the rectangular waveguide into a CP TE_{11} -mode of the circular waveguide. In fact, as experimentally demonstrated in the previous Chapter, the used structure effectively acts as a linear-to-circular polarization transformer. Moreover, this setup is greatly independent from the surrounding environment; therefore, the operation is not affected by the different cross-sections of the connected waveguides.

In order to validate this idea, we have numerically simulated the behavior of the overall structure reported in Fig. 68, consisting of a rectangular and a circular waveguide connected together through the proposed complementary resonator.

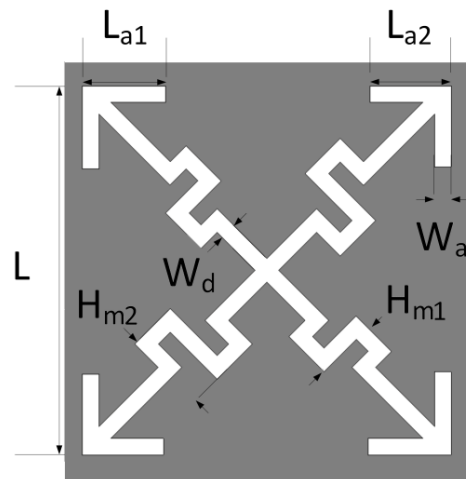


Fig. 67: Geometrical sketch of the proposed complementary resonator with dimensions: $L = 8.2$ mm, $L_{a1} = 2$ mm, $L_{a2} = 1.9$ mm, $H_{m1} = 1.8$ mm, $H_{m2} = 1.5$ mm, $W_d = 0.4$ mm, $W_a = 0.4$ mm. The resonator is drilled in a metallic sheet.

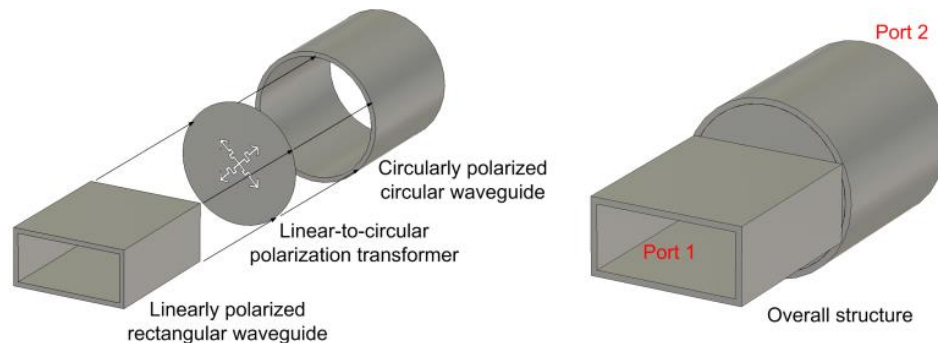


Fig. 68: Geometrical sketch of the proposed rectangular-to-circular waveguide transition.

By using the full-wave simulator CST Microwave Studio [14], we have evaluated the scattering parameters of the overall structure. Please note that, in the mono-modal frequency range of the WR-90, the rectangular waveguide supports only the TE_{10} -mode, while the circular waveguide supports a pair of degenerate TE_{11} -modes, as shown in Fig. 69.

From the S-parameters reported in Fig. 70, we can conclude that the complementary resonator effectively conveys the electromagnetic field from the rectangular waveguide to the circular one. In fact, the magnitude of the reflection coefficient of the rectangular feeding port $|S_{1(1)1(1)}|$ (where the numbers in parenthesis refer to the waveguide mode) is below -10 dB around the resonant frequency of the resonator. Moreover, two degenerate TE_{11} -modes are excited in the circular waveguide. These two modes, at the resonant frequency of 9.4 GHz, have the same amplitude ($|S_{2(1)1(1)}|$ and $|S_{2(2)1(1)}|$ both around -3 dB) and show a phase difference of 90° (see Fig. 71), confirming the presence of a CP TE_{11} -mode in the circular waveguide.

We remark here that, compared to other rectangular-to-circular waveguide transitions, such as the one reported in [15], the proposed structure is more compact and easy to realize, while adding the functionality of a polarization transformer. Furthermore, the self-filtering behavior of the proposed transition is particularly useful in satellite communication systems, where satellite signals usually exhibit a narrower bandwidth compared to the operative band of the used waveguides.

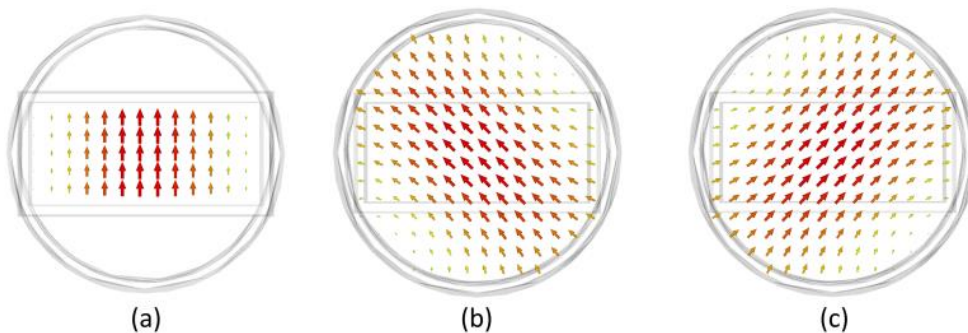


Fig. 69: Electric field lines of the structure shown in Fig. 68: (a) TE_{10} -mode of the rectangular waveguide, (b) and (c) degenerate TE_{11} -modes of the circular waveguide.

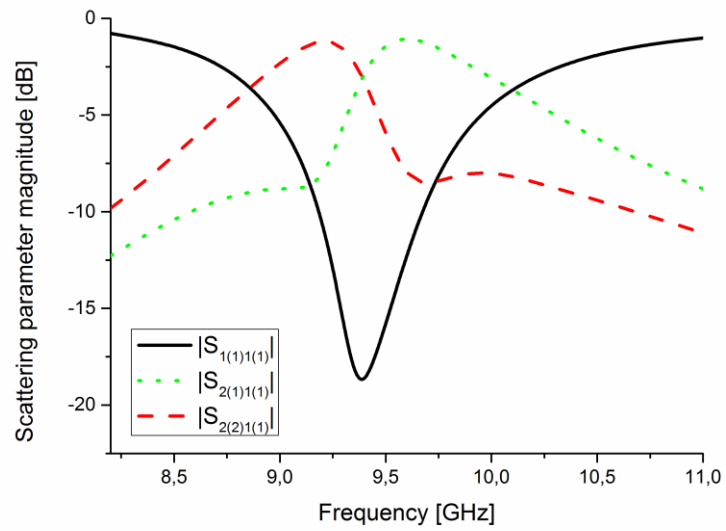


Fig. 70: Simulated magnitude of the scattering parameters of the structure shown in Fig. 68.

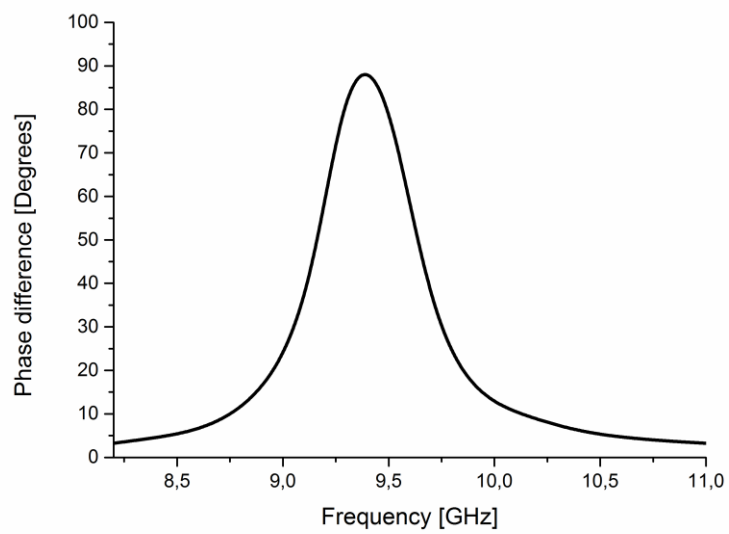


Fig. 71: Simulated phase difference between the degenerate TE_{11} -modes at port 2 of the structure shown in Fig. 68.

4.1.2 DESIGN OF POWER DIVIDERS

4.1.2.1 Output ports in circular waveguide

In the previous Subsection, we have presented a novel rectangular-to-circular waveguide transition based on the employment of a complementary resonator. This setup, being extremely compact, can be used as the fundamental element to design other waveguide components.

As a first example, we propose the design of a power divider using one rectangular waveguide and two circular waveguides connected to the rectangular one through a complementary resonator. The resulting structure is shown in Fig. 72, where the dimensions of the complementary resonator are: $L = 8.2$ mm, $L_{a1} = 2$ mm, $L_{a2} = 2$ mm, $H_{m1} = 1.2$ mm, $H_{m2} = 1.5$ mm, $W_d = 0.4$ mm, $W_a = 0.4$ mm. This component allows to equally splitting the power from the rectangular into the two circular waveguides. Moreover, similarly to the previous case, inside the circular waveguides a CP TE_{11} -mode is excited. This behavior is confirmed by the simulated results reported in Fig. 73 and Fig. 74.

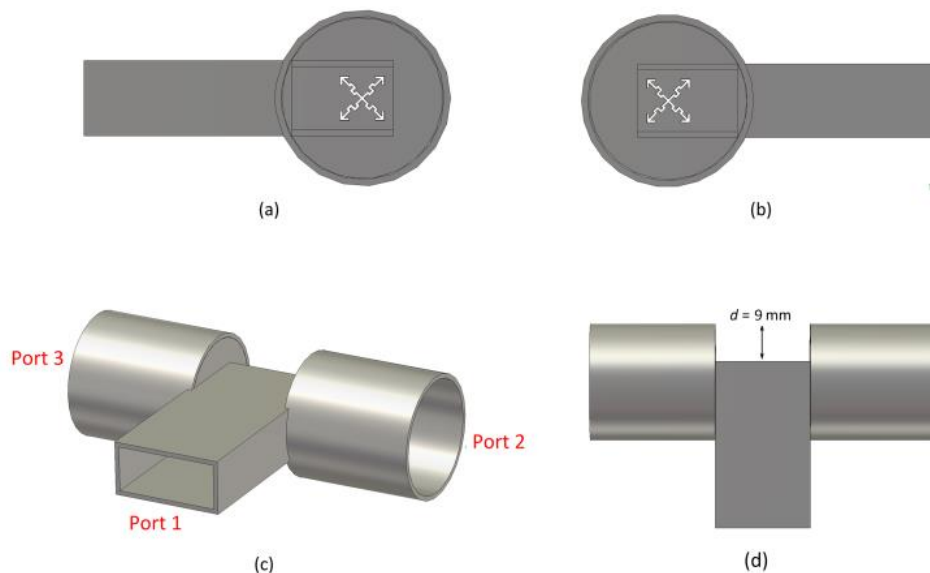


Fig. 72: Right view (a), left view (b), perspective view (c) and top view (d) of the power divider having output ports in circular waveguides.

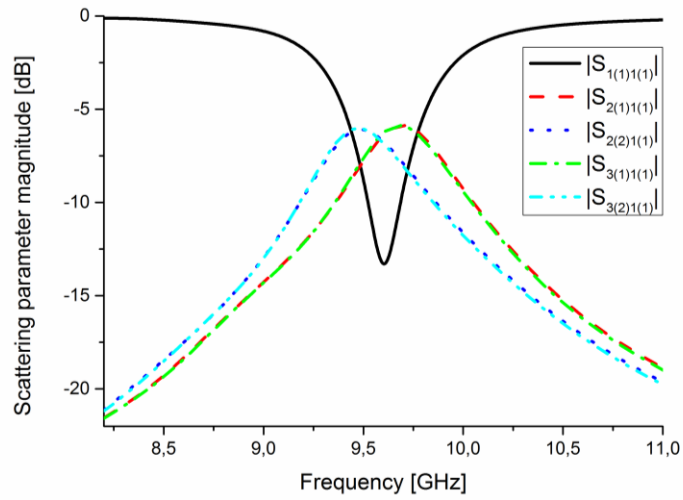


Fig. 73: Simulated magnitude of the scattering parameters of the structure shown in Fig. 72.

In fact, around the resonant frequency of the complementary resonators, the magnitude of the reflection coefficient at the input port ($|S_{1(1)1(1)}|$) is below -10 dB, while the transmission parameters of the output port modes ($|S_{2(1)1(1)}|$, $|S_{2(2)1(1)}|$, $|S_{3(1)1(1)}|$, $|S_{3(2)1(1)}|$) are around -6 dB. Therefore, the input power is equally split between the four modes of the two circular waveguides. Moreover, the phase difference between the two degenerate TE_{11} -modes of each circular waveguide is around 90° , confirming the presence of a CP TE_{11} -mode in both circular waveguides.

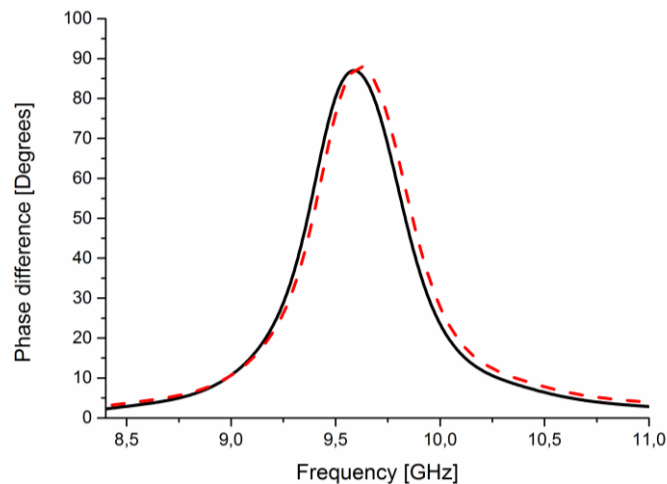


Fig. 74: Simulated phase difference between the degenerate TE_{11} -modes at port 2 (black-solid line) and port 3 (red-dashed line) of the structure shown in Fig. 72.

4.1.2.2 Output ports in rectangular waveguide

Using a similar complementary resonator, we can also design a power divider with output ports in rectangular waveguides, as shown in Fig. 75. In this case, the complementary resonators (whose dimensions are reported in Fig. 75) transmit a linear polarization in the output ports and allow equally splitting the input power, as shown in Fig. 76. Moreover, the reflection coefficient at the input port is again below -10 dB around the resonant frequency of the complementary resonators.

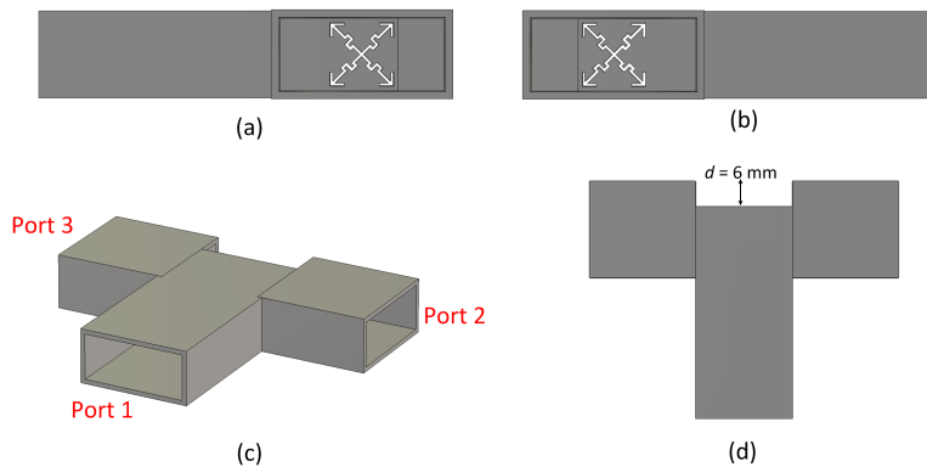


Fig. 75: Right view (a), left view (b), perspective view (c) and top view (d) of the power divider with rectangular waveguides. Resonator dimensions are: $L = 8.2$ mm, $L_{a1} = 2$ mm, $L_{a2} = 2$ mm, $H_{m1} = 1.5$ mm, $H_{m2} = 1.5$ mm, $W_d = 0.4$ mm, $W_a = 0.4$ mm.

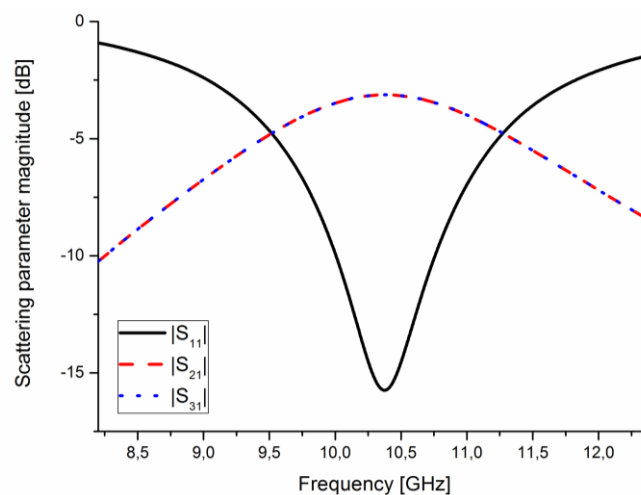


Fig. 76: Magnitude of the scattering parameters of the structure shown in Fig. 75.

4.1.3 DESIGN OF AN ORTHOMODE TRANSDUCER

The orthomode transducer is a microwave component that allows combining or separating two orthogonally polarized modes into a single waveguide. In particular, this component finds application in those communication systems that use a single horn antenna to simultaneously transmit and receive signals over two orthogonal polarizations.

As shown in Fig. 77, we consider here an orthomode transducer having two linearly polarized output ports at the end of two regular rectangular waveguides and a dual-linear polarization input at the end of a squared waveguide. At the junctions between the three ports we have placed the complementary resonator shown in Fig. 78. In this case, since the complementary resonators have to transmit a single linear polarization only, we have removed one of the two branches of the original complementary resonator. In this way, it can be excited by and can transmit only the waveguide mode with the electric field orthogonal to it.

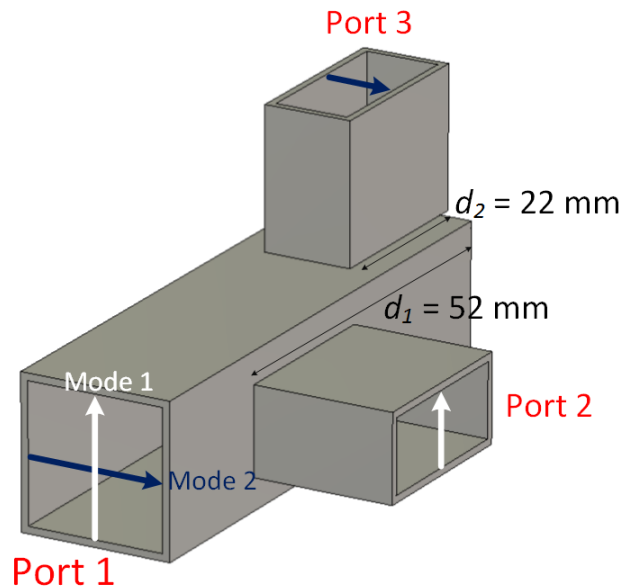


Fig. 77: Perspective view of the proposed orthomode transducer.

In Fig. 79, we show the corresponding scattering parameter magnitudes, obtained through a proper full-wave numerical simulation. From this figure, we can see that the squared waveguide input modes are well matched with different output ports. In fact, $|S_{1(1)1(1)}|$ and $|S_{1(2)1(2)}|$ are below -10 dB around the resonant frequency of the

complementary resonators. Moreover, the transmission from the input port mode 1 to output port 2 ($|S_{2(1)1(1)}|$) and from the input port mode 2 to output port 3 ($|S_{3(1)1(2)}|$) is close to one. Finally, the achieved isolation between the two polarizations is greater than -50 dB.

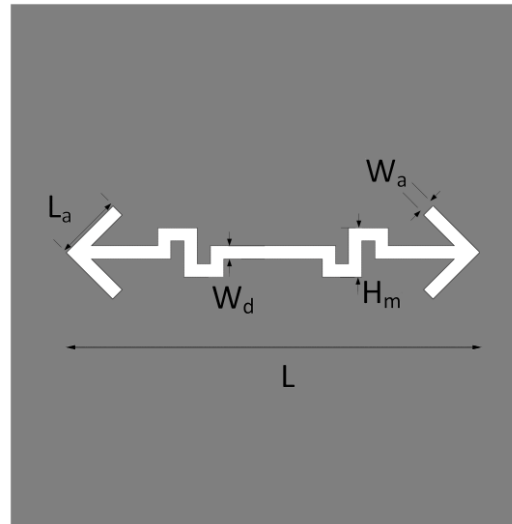


Fig. 78: Geometrical sketch of the linearly polarized complementary resonator with dimensions: $L = 8.6$ mm, $L_a = 3.5$ mm, $H_m = 2$ mm, $W_d = 0.4$ mm, $W_a = 0.4$ mm.

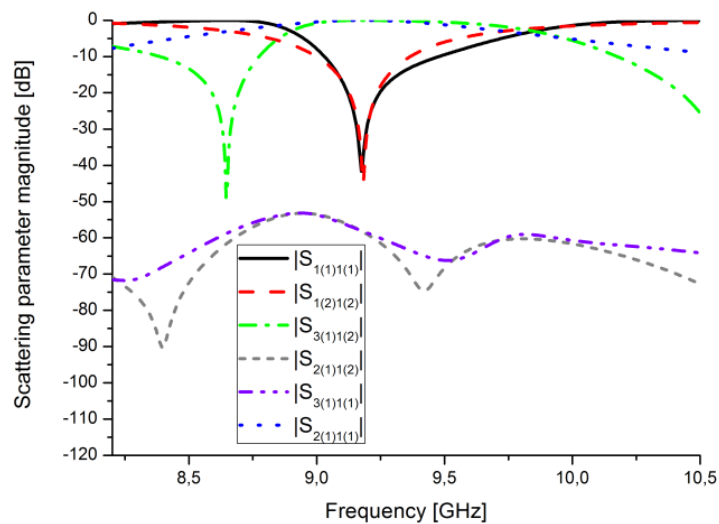


Fig. 79: Simulated magnitude of the scattering parameters of the structure shown in Fig. 77.

4.2 Low-cost and Broadband MTM-Inspired Absorber without a Metallic Backing

Radar absorbing structures (RAS) play a key-role in different application fields, and, particularly, in the reduction of the RCS of civil or military platforms (e.g. aircraft, ships, tanks, and other objects). Although several RAS configurations have been proposed in the literature [16], most of them require, as it happens also for the first radar absorbers (i.e. the Dallenbach absorber and the Salisbury screen), the use of a metallic ground plane, allowing both cancellation of the transmitted field beyond the absorber and introduction of a proper boundary condition useful to cancel the reflected wave. However, the use of a metallic plate entails also some inherent disadvantages, e.g. when a non-metallic object has to be hidden, a metallic cover may significantly increase the weight as well as the RCS of the object itself outside the operating band of the absorber.

Reducing both the out-of-band reflection and the weight of the absorber is possible exploiting the unusual properties of MTMs. For instance, in [17] a MTM-based absorber without a metallic backing is proposed by using a perfect magnetic conductor made of a proper array of magnetic inclusions. In [18], Landy et al. propose to use only two MTM resonators to design an absorbing structure with near unity absorption. Another similar approach has been proposed in [19], consisting of two resonators and a metal wire. However, all these approaches are limited by the narrow frequency bandwidth characterizing the operation of MTM-based components [20].

In order to overcome this issue, we propose here to move from a MTM-based approach to a MTM-inspired one. In fact, recently, several components have been proposed [21]-[24] that, rather than using tri-dimensional bulky metamaterials, take advantage of MTM concepts by using a single metallic inclusion or a two-dimensional structure (i.e. metasurface). In particular, this Section introduces a new low-cost and wideband absorber based on the use of a metasurface and a proper resistive sheet. First, we design a metasurface that acts as a metallic plate in the X-band. Then, in order to absorb the wave reflected by the metasurface, we realize a resistive sheet with the required surface resistance. Finally, we present the design and the experimental characterization of the overall absorber.

4.2.1 DESIGN OF THE METASURFACE

The structure of a traditional Salisbury screen, whose sketch is reported in Fig. 80, consists of a metallic backing and a resistive sheet placed $\lambda/4$ apart from it (where λ is the desired operational wavelength). In order to remove the metallic backing without affecting the behaviour of the absorber, we need a proper metasurface that, in a specific range of frequencies, acts as a metallic plate.

Inspired by the reflection properties shown by MTM resonant inclusions, we have designed a simple resonating MTM-inspired structure consisting of a planar array of metallic rings printed on both sides of a 1.6 mm-thick dielectric substrate (FR4 with $\epsilon_r = 4.3$ and $\tan \delta = 0.025$). The metasurface has been simulated through the use of the full-wave simulator CST Microwave Studio. For the sake of simplicity, we report in Fig. 81 only the transmission (S_{21} scattering parameter) and reflection coefficients (S_{11} scattering parameter) for a normally incident plane-wave with linearly y-polarized electric field. However, due to the isotropy of the inclusion on the array plane, the MTM-inspired surface is able to reflect any polarization of the incident electric field. The spatial periodicity and the inner and outer diameter of the rings have been designed in order to have a PEC-like behaviour (zero transmission and high reflection) in a broad frequency range centred at 10.2 GHz. As shown in Fig. 81, the EM wave is almost completely reflected by the metasurface and no transmission occurs in the entire X-band. Please note that this behaviour has been obtained despite the significant reduction of metallic material (about 70% less than a full metal plate).

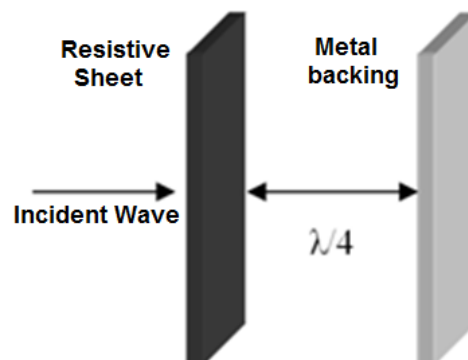


Fig. 80: Geometrical sketch describing the structure of a traditional Salisbury screen.

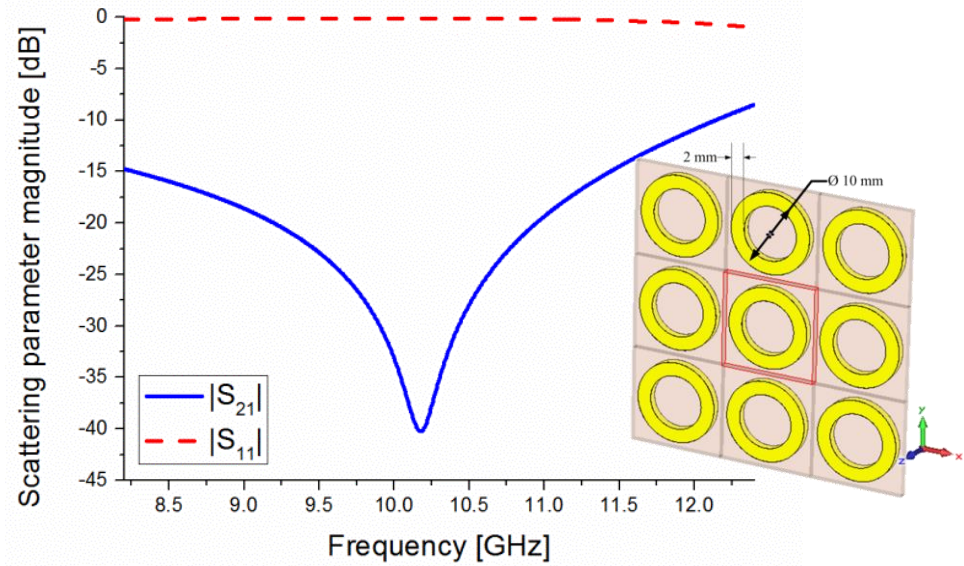


Fig. 81: Simulated amplitude of the transmission and reflection coefficients (for normal incidence) of the proposed metasurface (inset: geometrical sketch of the metasurface and dimensions of the metallic rings).

4.2.2 DESIGN OF THE RESISTIVE SHEET

Due to their inherent low weight and low space occupancy, the use of engineered surfaces has experienced a great development in the last decade [25]. These surfaces, also known as reactive sheets, exhibit ideally a zero real part and a tunable imaginary part of their intrinsic surface impedance [26] and can be employed for many intriguing applications, i.e., [27]-[28]. On the contrary, resistive sheets, which exhibit a zero imaginary part and a tunable real part R_s (Ω/sq), are typically used for the reduction of the radar cross section of a target [29] and/or for the reduction of the antenna edge effects [30], due to their ability to dissipate the electromagnetic energy.

From a conceptual viewpoint, resistive sheets simply consist of a thin layer of a lossy material. Nevertheless, their practical realization still remains a not straightforward task. In fact, since the surface resistance of a sheet is equal to $R_s = 1/(\sigma t)$, being σ the conductivity of the lossy material and t its thickness, the fabrication of a sheet exhibiting a desired value of R_s requires a strict control of both the thickness and the conductivity of the lossy material constituting the sheet.

In this Subsection, we propose an easy realization procedure of resistive sheets made of graphite powder. Graphite powder has been proposed as an element to realize electromagnetic shielding devices [31] or to design artificially synthesized dry phantom material [32] but, to the best of our knowledge, the use of graphite powder for the realization of resistive sheets has not been investigated yet, especially for what concerns the design procedure and the actual implementation.

4.2.2.1 Realization technique

As already clarified, the main issue in the realization of a resistive sheet is the choice of a proper lossy material. After an accurate analysis, we have found that, due to its peculiarities, powdered graphite can be considered as an excellent candidate for this purpose. In fact, graphite powder is a low-cost material available in spray bottles as an anti-adhesive and lubricant (see Fig. 82-(a)). The availability of a spray product dramatically simplifies the deposition process of the lossy material. Moreover, its electrical conductivity can be tuned in a wide range by controlling the powder volume fraction [33]. As we will show below, the possibility to control the graphite conductivity during the powder deposition process allow us achieving a fine control of the surface resistance exhibited by the sheet.

Taking into control the deposition time, the graphite powder has been deposited onto a square semi-rigid plastic sheet with thickness 0.2 mm and relative electric permittivity equal to $\varepsilon_r = 2.7$ [34]. To guarantee the homogeneity of the samples, sheet dimensions are chosen to be small compared to the emission cone of the graphite spray. Following this procedure, we have realized 18 samples progressively increasing the deposition time. A picture of a realized sample is shown Fig. 82-(b).

4.2.2.2 Resistive sheets characterization

The realized resistive sheets have been characterized using the well-known Van der Pauw method [34]. This method allows retrieving the surface resistance of a resistive sheet by using a set of four DC voltage measurements. For these measurements we have used the regulated power supply Life 41.5D1731SB3A and a digital multimeter EuroTEK DM50. The DC measurement setup is shown in Fig 83.

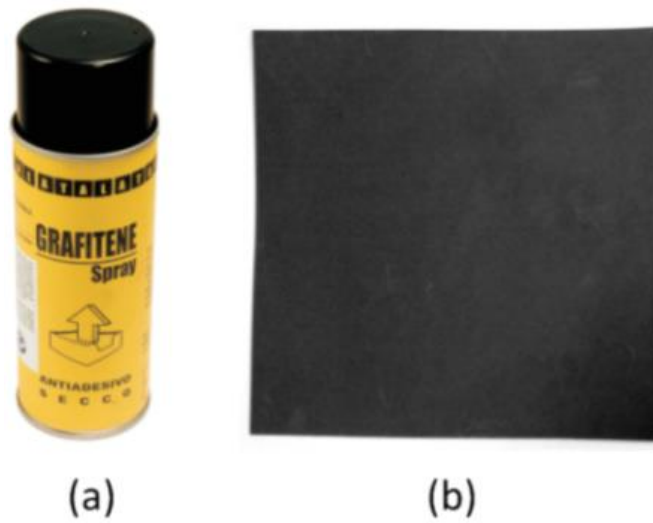


Fig. 82: (a) Commercial graphite powder spray produced by ATAL SrL; (b) A realized resistive sheet composed by a plastic sheet covered by a proper amount of graphite powder. The two images are not in scale.

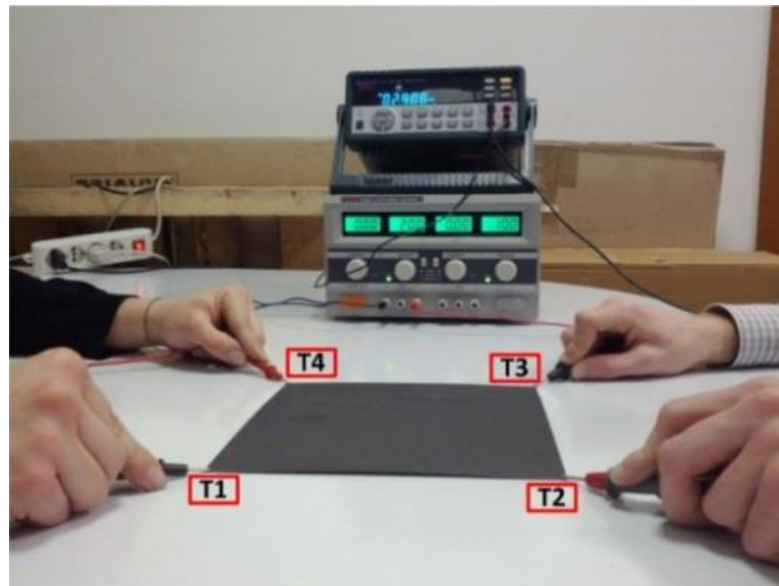


Fig. 83: Application of the Van der Pauw method for the resistive sheet characterization.

First, the sample is excited by a DC current I_{23} at one side (delimited by the points T2-T3) and the output voltage V_{14} is measured at the opposite side (T1-T4). The

resistance $R_{23,14}$ is equal to $R_{23,14} = V_{41} / I_{23}$. The procedure is then repeated to calculate $R_{14,23}$ by inverting the input and the output sheet side. According to the Van der Pauw method, the vertical resistance R_v is equal to the average value of the two resistances, i.e.:

$$R_v = \frac{R_{23,14} + R_{14,23}}{2}. \quad (11)$$

A similar procedure can be performed to calculate the vertical resistance R_h . Once R_h and R_v have been calculated, the surface resistance R_s of the resistive sheet can be computed by numerically solving the following equation:

$$e^{-\pi R_v / R_s} + e^{-\pi R_h / R_s} = 1. \quad (12)$$

In Fig. 84, we report the measured surface resistance values of the 18 realized samples as a function of the surface density of the graphite powder deposited on each sample. The surface density is defined as the ratio between the mass of the graphite powder and the area of the plastic sheet. The powder mass has been retrieved by measuring the mass of the resistive sheet with a professional scale (Nahita series 5023 100g/1 mg) and subtracting to it the mass of the bare plastic sheet. As expected, as the mass of the deposited graphite powder increases, the relative surface resistance of the sheet decreases. In particular, the surface resistance is almost inversely proportional to the graphite powder mass. This is a non-surprising result since the surface resistance of a lossy material is inversely proportional to its thickness and to its conductivity that, in the case of the graphite powder, increases with its volume fraction [33]. The curve in Fig. 84 can be considered as the calibration curve of the graphite spray and can be easily exploited to estimate the mass of the graphite powder able to return a desired value of the surface resistance. It is worth noticing that, by finely controlling the amount of the deposited graphite powder, it is possible to achieve surface resistance values ranging from $50 \Omega/sq$ to $800 \Omega/sq$.

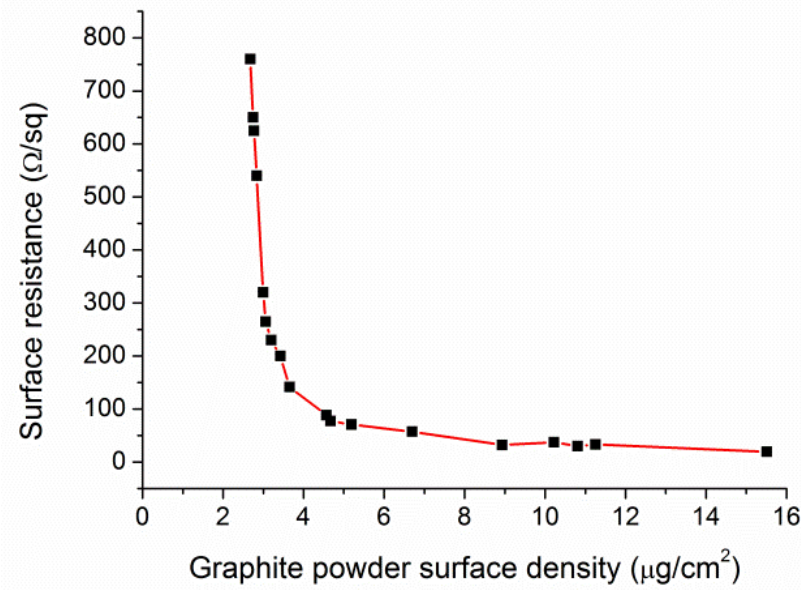


Fig. 84: Surface resistance exhibited by the 18 realized samples compared to the relative graphite powder surface density.

4.2.2.3 Experimental verification

To experimentally verify the effectiveness of both the realization procedure and the characterization process, we have used the experimentally setup schematized in Fig. 85 consisting of a coax-to-waveguide adapter connected to a Rohde Swartz R&S®ZVA40, a WR90 waveguide, and a matched load. A properly shaped portion of the resistive sheet under test, supported by a sample holder, is placed between the matched load and the WR90 waveguide (see the inset of Fig. 85). This setup allows to measure the reflection coefficient of the resistive sheet that can be compared to the one returned by a full-wave simulator when a resistive sheet of the value retrieved in the previous Subsection is used. The comparison between the measured and simulated reflection coefficients is shown in Fig 86 for two resistive sheets with surface resistance equal to $41 \Omega/\text{sq}$ and $141 \Omega/\text{sq}$, respectively. The agreement between simulations and measurements is excellent, confirming the effectiveness of the proposed procedure to realize a resistive sheet with a desired value of surface resistance.

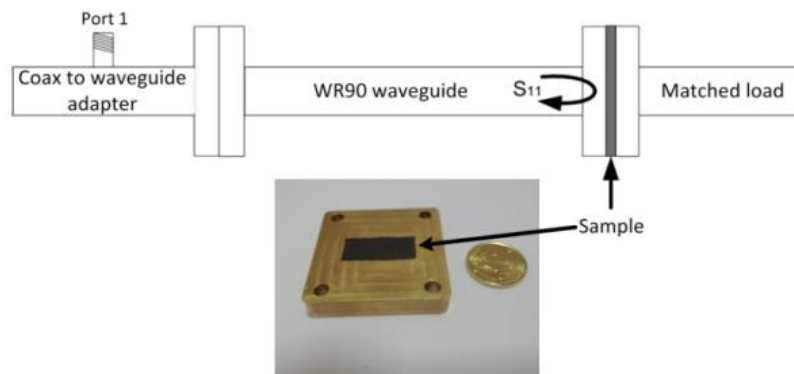


Fig. 85: Experimental setup used to measure the reflection coefficient of the realized resistive sheets.

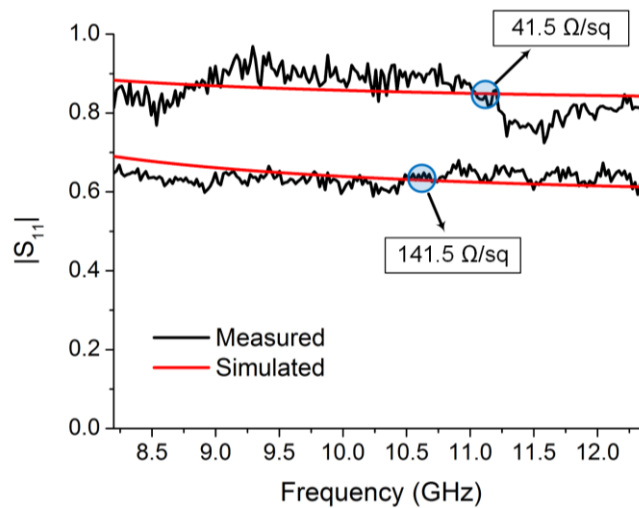


Fig. 86: Comparison between the measured and the simulated amplitude of the S_{11} parameter for two resistive sheets with $41 \Omega/sq$ and $141 \Omega/sq$, respectively.

4.2.3 IMPLEMENTATION OF THE ABSORBER

Since the metasurface emulates the behaviour of a metal plate within the band of interest, it can be used to implement a MTM-inspired absorber. In particular, starting from the classical configuration of a Salisbury screen (see, e.g. Fig. 80), the absorber here presented consists of the proposed metasurface, some foam sheets used as spacers, and a proper resistive sheet, as shown in Fig. 87. In order to achieve the impedance matching between free-space and the resistive sheet and, at the same time, allow absorbing the reflected wave from the metasurface, the resistive sheet must exhibit a surface resistance around 377Ω . The metasurface has been fabricated through the use

of a LPKF Protomat-S milling machine (Fig. 87-b) and the resistive sheet has been realized by using the procedure described in previous Subsection, obtaining a surface resistance around 390Ω (Fig. 87-c). Finally, we have assembled the overall structure, obtaining the planar absorber of dimensions $210 \times 210 \times 5 \text{ mm}^3$ shown in Fig. 87-a.

4.2.4 EXPERIMENTAL REALIZATION AND MEASUREMENTS

The performances of the absorber have been verified by using a measurement system consisting of two high-gain pyramidal horn antennas (one in TX mode and one in RX mode) and a vector network analyzer, as shown in Fig. 88. In order to emulate the illumination from a monostatic radar, the absorber has been placed in the far-field zone of both radiators and centred with respect to the joining between them, in order to illuminate the absorber with a normally incidence plane-wave. Such configuration tests the performances of the absorber in the worst case, i.e. normal incidence, because for different incidence angles the energy is reflected back in opposite direction with respect to the transmitter and the captured reflected energy is much lower. Please note that the fabricated prototype has lateral dimensions of $210 \times 210 \text{ mm}^2$ ($7\lambda_0 \times 7\lambda_0$), which are large enough to perform a reliable measurement in free-space conditions.

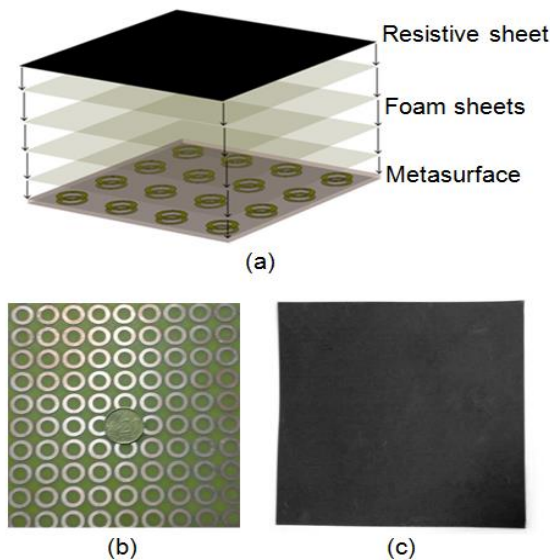


Fig. 87: (a) Geometrical sketch, (b) rear and (c) front view of the proposed absorber.

The corresponding measured and simulated absorption (defined as $A = 1 - |S_{11}|^2 - |S_{21}|^2$) is reported in Fig. 89. From this figure, it is possible noticing that the combined

operation of the metasurface and the resistive sheet significantly reduces the reflection from and the transmission through the metasurface, being the energy delivered by the incident field almost completely dissipated by the resistive sheet. In fact, the measured absorption values are greater than 0.9, i.e., more than 90% of the energy is absorbed in the entire X-band, confirming the wideband behaviour of the proposed absorber.

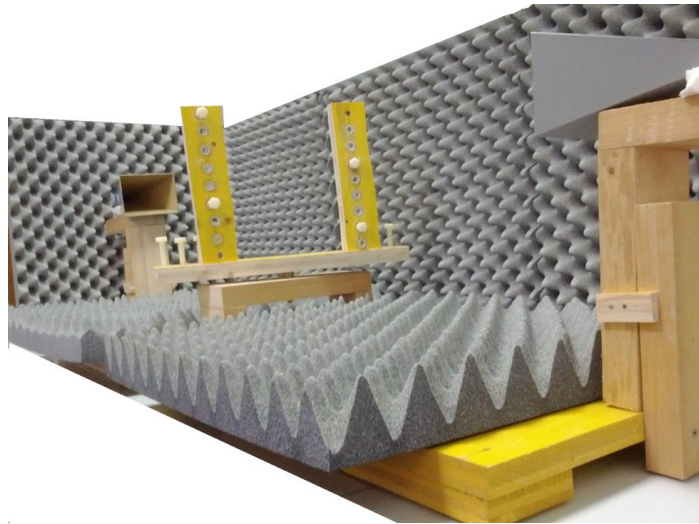


Fig. 88: Photograph of the measurement system consisting of two high-gain pyramidal horn antenna and the sample holder.

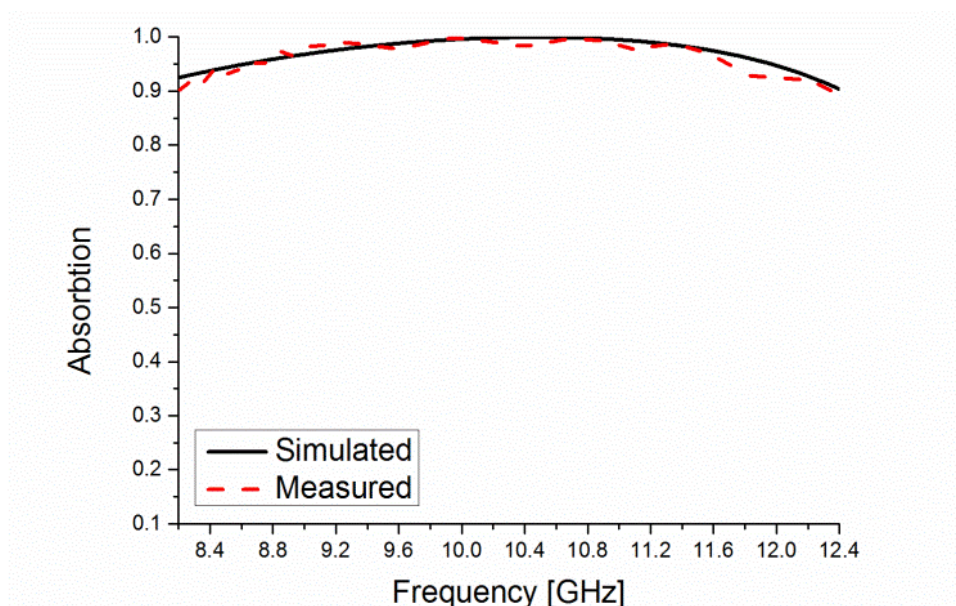


Fig. 89: Absorption of the metamaterial-inspired absorber shown in Fig. 87.

4.3 Summary

In this Chapter, we have first proposed the design of a few microwave components characterized by a compact and easily realizable structure based on the employment of MTM-inspired resonators. At first, we have presented a waveguide transition that allows effectively coupling a rectangular waveguide and a circular one. At the same time, this component converts the linearly polarized TE_{10} -mode of the rectangular waveguide into a CP TE_{11} -mode in the circular waveguide. Then, we have shown that similar structures can be successfully used to design other waveguide components. In particular, we have presented two different power dividers and an orthomode transducer. The presented full-wave numerical results demonstrate the validity of the proposed approach and support the effectiveness of the proposed designs. The planar and all-metallic nature of the insert where the complementary resonators are drilled on makes the presented approach a low-cost and easily implementable solution for waveguide components finding applications in narrow-band satellite communications system.

Then, we have demonstrated that a proper combination of a metasurface and a resistive sheet allows designing a low-cost and broadband MTM-inspired absorber without a metallic backing. In particular, the use of the proposed metasurface allows reducing weight and the used percentage of metal, in comparison to regular full metal plates. Moreover, consisting only of easily and economically feasible materials, the proposed structure can be an attractive solution to design a low-cost RAS. Simulated and measured results show that the absorption values are higher than 90% in entire the X-band, confirming that a normally incident electromagnetic field is almost completely absorbed by the proposed structure.

Finally, please note that the required resistive sheet has been realized through a novel technique based on the use of graphite powder. The proposed procedure allows realizing resistive sheets exhibiting the desired surface resistance in a wide range of values and may find application also in other technical fields, such as the realization of low-scattering antennas. We have experimentally validated our procedure using both a DC characterization based on the Van der Pauw method and a waveguide setup. The

experimental results are in excellent agreement with the full-wave simulation confirming the effectiveness of the proposed approach.

4.4 References

- [1] R.W. Ziolkowski, A.D. Kipple, Application of double negative materials to increase the power radiated by electrically small antennas, *IEEE Trans. Antennas Propagat.* 52 (2003) 2626-2640.
- [2] A. Alù, F. Bilotti, N. Engheta, L. Vegni, Subwavelength, compact, resonant patch antennas loaded with metamaterials, *IEEE Trans. Antennas Propagat.* 55 (2006) 13-25.
- [3] A. Alù, F. Bilotti, N. Engheta, L. Vegni, Subwavelength planar leaky-wave components with metamaterial bilayers, *IEEE Trans. Antennas Propagat.* 55 (2007) 882-891.
- [4] A. Lai, C. Caloz, T. Itoh, Composite right/left-handed transmission line metamaterials, *IEEE Microw. Mag.* 5 (2004) 34-50.
- [5] G.V. Eleftheriades, Enabling RF/microwave devices using negative-refractive-index transmission-line (NRI-TL) metamaterials, *IEEE Antennas Propag. Mag.* 49 (2004) 34-51.
- [6] F. Falcone, F. Martin, J. Bonache, R. Marqués, T. Lopetegui, M. Sorolla, Left handed coplanar waveguide band pass filters based on bi-layer split ring resonators, *IEEE Microw. Wireless Compon. Lett.* 14 (2004) 10-12.
- [7] F. Falcone, F. Martin, J. Bonache, R. Marqués, M. Sorolla, Coplanar waveguide structures loaded with split ring resonators, *Microw. Opt. Techn. Lett.* 40 (2004) 3-6.
- [8] P. Jin, R.W. Ziolkowski, Multi-frequency, linear and circular polarized, metamaterial-inspired, near-field resonant parasitic antennas, *IEEE Trans. Antennas Propagat.* 59 (2011) 1446-1459.
- [9] M. Barbuto, F. Bilotti, and A. Toscano, Design of a multifunctional SRR-loaded printed monopole antenna, *Int. J. RF Microw. CAE* 22 (2012) 552-557.
- [10] R. Marqués, F. Martin, M. Sorolla, *Metamaterials with negative parameters: theory, design and microwave applications*, Wiley, New York, 2007.
- [11] N. Ortiz, J. D. Baena, M. Beruete, F. Falcone, M.A.G. Laso, T. Lopetegui, R. Marqués, F. Martin, J. Garcia-Garcia, M. Sorolla, Complementary split-ring resonator for compact waveguide filter design, *Microw. Opt. Techn. Lett.* 46 (2005) 88-92.
- [12] L. Di Palma, F. Bilotti, A. Toscano, L. Vegni, Design of a waveguide diplexer based on connected bi-omega particles, *IEEE Microw. Wireless Compon. Lett.* 22 (2012) 126-128.

- [13] D. Ramaccia, L. Di Palma, G. Guarnieri, S. Scafè, A. Toscano, F. Bilotti, Balanced and unbalanced waveguide power splitters based on connected bi-omega particles, *Electron. Lett.* 49 (2013) 1504-1506.
- [14] CST Studio Suite 2013, CST Computer Simulation Technology AG, Available at: www.cst.com.
- [15] E. L. Holzman, A simple circular-to-rectangular waveguide transition, *IEEE Microw. Wireless Compon. Lett.* 15 (2005) 25-26.
- [16] Knott, E.F.: 'Radar Cross Section' (SciTech Publishing, Raleigh, NC, USA, 2004, second edition)
- [17] Bilotti, F., Toscano, A., Alici, K.B., Ozbay, E., Vegni, L.: 'Design of miniaturized narrowband absorber based on resonant-magnetic inclusions', *IEEE Trans. Electromagn. Compatibility.*, 2011, 53, (1), pp. 63–72., doi: 10.1109/TEMPC.2010.2051229
- [18] Landy, N.I., Sajuyigbe, S., Mock, J.J., Smith, D.R., Padilla, W.J.: 'Perfect metamaterial absorber', *Physical Review Lett.*, 2008, 100, pp. 207402-1-4., doi: 10.1103/PhysRevLett.100.207402
- [19] Cheng, Y., Yang, H.: 'Design, simulation and measurement of metamaterial absorber', *J. Appl. Phys.*, 2010, 108, p. 034906. doi: 10.1063/1.3311964
- [20] Barbuto, M., Monti, A., Bilotti, F., Toscano, A.: 'Design of a non-Foster actively loaded SRR and application in metamaterial-inspired components', *IEEE Trans. Ant. Propag.*, 2013, 61, (3), pp. 1219–1227., doi: 10.1109/TAP.2012.2228621
- [21] Barbuto, M., Bilotti, F., and Toscano, A.: "Novel waveguide components based on complementary electrically small resonators," *Photonic Nanostruct.*, 2014, 12, pp. 284-290., doi: 10.1016/j.photonics.2014.03.005
- [22] Monti, A., Soric, J., Alu, A., Bilotti, F., Toscano, A., and Vegni, L.: "Overcoming mutual blockage between neighboring dipole antennas using a low-profile patterned metasurface," *IEEE Ant. Wireless Propag. Lett.*, 2012, 11, pp. 1414-1417., doi: 10.1109/LAWP.2012.2229102.
- [23] Ramaccia, D., Di Palma, L., Ates, D., Ozbay, E., Toscano, A., Bilotti, F.: "Analytical Model of Connected Bi-Omega: Robust Particle for the Selective Power Transmission Through Sub-Wavelength Apertures", *IEEE Trans. Antennas Propag.*, 2013, 62 (4), pp. 2093-2101, doi: 10.1109/TAP.2014.2301445.
- [24] Ramaccia, D., Di Palma, L., Guarnieri, G., Scafè, S., Toscano, A. Bilotti, F.: "Balanced and unbalanced waveguide power splitter based on bi-omega particles", *Electr. Letters*, 2013, 49(24), pp.1504-1506, doi: 10.1049/el.2013.1565.
- [25] Holloway, C.L., Kuester, E.F., and Gordon, J.A., O'Hara, J., Booth, J., Smith, D.R.: 'An Overview of the Theory and Applications of Metasurfaces', *IEEE Ant. Propag. Mag.*, 2012, 54(2), pp.10-35, doi: 10.1109/MAP.2012.6230714.
- [26] Ramaccia, D., Bilotti, F., and Toscano, A.: 'Analytical model of a metasurface consisting of a regular array of sub-wavelength circular holes in a metal sheet', 2011, *PIER M*, 18, pp. 209-219, doi: 10.2528/PIERM11050908.

- [27] Monti, A., Soric, J., Alù, A., Toscano, A., and Bilotti, F.: "Anisotropic mantle cloaks for TM and TE scattering reduction," *IEEE Trans. Ant. Propag.*, 2015, (under review).
- [28] Barbuto, M., Alù, A., Bilotti, F., Toscano, A., and Vegni, L.: 'Characteristic impedance of a microstrip line with a dielectric overlay,' *COMPEL*, 2013, 32(6), pp. 1855-1867, doi: 10.1108/COMPEL-10-2012-0283.
- [29] Knott, E.F.: 'Radar Cross Section' (SciTech Publishing, Raleigh, NC, USA, 2004, second edition).
- [30] Volakis J.L., Alexanian A., and Lin. J. M.: 'Broadband RCS reduction of rectangular patch by using distributed loading', *Electronics Letters*, 1992, 28(25), pp. 2322-2323, doi: 10.1049/el:19921494.
- [31] Morari C., Balan I., Pintea J., Chitanu E., and Iordache I., 'Electrical conductivity and electromagnetic shielding effectiveness of silicone rubber filled with ferrite and graphite powders', *PIER M*, 2011, 21, pp. 93-104., doi:10.2528/PIERM11080406.
- [32] Tamura, H., Nishikawa, T., Kobayashi, T., Nojima, T., 'A dry phantom material composed of ceramic and graphite powder', *IEEE Trans. Electromagn. Compat.*, 1997, 39(2), pp. 132-137, doi: 10.1109/15.584935.
- [33] Deprez, N., and McLachlan D.S., 'The analysis of the electrical conductivity of graphite conductivity of graphite powders during compaction', *J. Phys. D: Appl. Phys.*, 1988, 21(1), pp. 101-107, doi: 10.1088/0022-3727/21/1/015.
- [34] Riddle B., Baker-Jarvis J., and Krupka J., 'Complex permittivity measurements of common plastics over variable temperatures,' *IEEE Trans. Microwave Theory Tech.*, 2003, 51(3), pp. 727-733, doi: 10.1109/TMTT.2003.808730.
- [35] Van der Pauw, L. J., 'A method of measuring specific resistivity and Hall effect of discs of arbitrary shape', *Philips Research Reports*, 1958, 13, pp. 1-9.

Chapter 5

Circular polarized patch antenna generating orbital angular momentum

The concept of OAM is well known at optical frequencies, where it has found application in trapping and manipulating of microscopic particles, imaging and communication systems [1]-[4]. Recently, it has been shown that an electromagnetic (EM) field with a non-zero OAM can be also generated in the microwave range using standard antenna systems [5]. Starting from this first demonstration, several systems generating EM fields with non-zero OAM have been proposed [5]-[9]. Such systems are based on two different approaches. The first one consists of a circular antenna array in which the different elements are fed with signals having the same amplitude and a progressive phase shift, such that the total delay between the first and the last element is an integer multiple l of 2π [5]-[6]. A variant of this approach is presented in [7] and makes use of a time-switched array. The second approach consists of using a reflector with a helical phase profile achieved by mechanically modifying a spiral [8] or parabolic [9] reflector.

However, both these approaches have some inherent drawbacks. In fact, the first approach requires the design and the implementation of a transmission line network to properly feed the array elements. On the other hand, the fabrication of a reflector with a helical phase profile is not easily replicable. Moreover, both solutions require considerable space occupancy, weight, and costs.

In contrast, at optical frequencies there are different techniques used to generate OAMs. As an example, the higher order laser modes of a laser cavity, also known as Laguerre-Gauss (LG) laser modes, have a non-zero OAM and can be either directly generated [10] or obtained by properly combining two Hermite-Gauss (HG) laser modes

[11]. This means that, for instance, a LG^1_0 laser mode can be generated combining two orthogonal HG_{10} and HG_{01} modes with a $\pi/2$ phase delay between them [1].

Inspired by this technique, we may think of properly combine orthogonal higher order modes of resonant antennas to generate OAMs at microwave frequencies.

In this Chapter, in order to obtain an EM field with a non-zero OAM at microwave frequencies, we propose to use a single patch antenna. In particular, we show that the higher order modes of a circularly polarized patch antenna can be used to generate different OAM states. This solution is clearly cheaper, lighter and more compact compared to the ones already proposed [5]-[9]. Moreover, although OAM cannot be used to improve the performances of a communication system except in very particular cases [12], the proposed solution can be useful to experimentally investigate the properties of the OAM or to extend to microwave frequencies imaging and identification techniques based on OAM and developed in the optical regime [13].

The structure of the Chapter is as follows. In Section 1, we report the analytical study of a circular patch antenna and show that an EM field with non-zero OAM can be generated if we make this component working on higher order circularly polarized (CP) modes. In Section 2, we present the design procedure and the results of the full-wave simulations for an elliptical patch antenna generating a helical far-field radiation pattern with circular polarization. In Section 3, we validate these results through the characterization of the radiating and matching properties of a fabricated prototype. Finally, in Section 4, we summarize the obtained results.

5.1 Analytical Study

A patch antenna, in its general form, consists of a metallic patch placed on a grounded dielectric slab [14]. Over the last decades, patch antennas with different geometries have been proposed to satisfy several design constraints (see, for instance, [15]-[18]). Let's consider the circular patch antenna depicted in Fig. 90. In some applications, this type of patch antenna is preferred to the rectangular one due to its greater flexibility in terms of achievable radiation patterns.

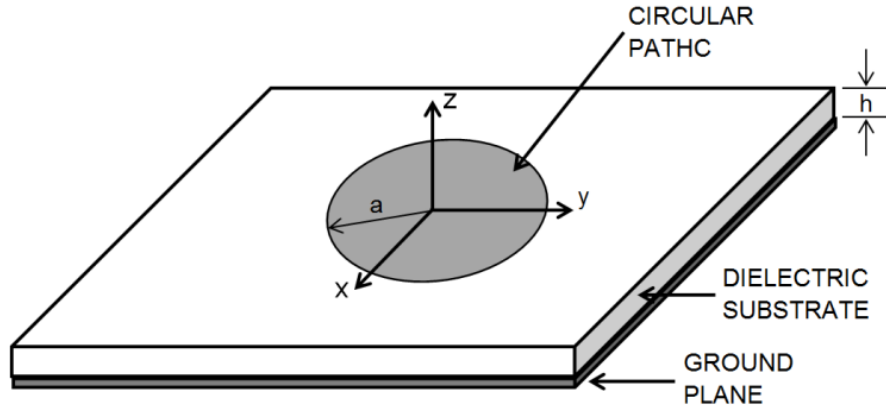


Fig. 90: Geometrical sketch of a circular patch antenna. The main geometrical parameters are the radius of the patch a and the thickness of the dielectric substrate h .

In order to evaluate the radiating performances of a patch antenna, different analysis methods can be used. In our case, we have chosen the cavity model that is a good compromise between accuracy of the obtained results and complexity of the model. This approximate model is based on considering the antenna to be a dielectric loaded resonant cavity.

In the case of a circular patch antenna, the radiated electric field components by a TM_{nm} mode can be derived by using the cavity model in cylindrical coordinates and are expressed as [19]:

$$\begin{aligned} E_{\theta n} &= j^n \frac{V k_0 a}{2} \frac{e^{-jk_0 r}}{r} \cos n\varphi [J_{n+1}(\gamma) - J_{n-1}(\gamma)] \\ E_{\varphi n} &= j^n \frac{V k_0 a}{2} \frac{e^{-jk_0 r}}{r} \cos \theta \sin n\varphi [J_{n+1}(\gamma) + J_{n-1}(\gamma)] \end{aligned} \quad (13)$$

where $V = hE_0 J_n(ka)$ is the edge voltage at $\varphi = 0$, h is the thickness of the dielectric substrate, E_0 is the value of the electric field at the edge of the patch, $\gamma = k_0 a \sin \theta$, a is the radius of the patch, and J_i is the Bessel function of the first kind and order i .

As anticipated in the introduction, we now investigate the use of CP higher order modes of a patch antenna in order to produce an EM field with non-zero OAM. Circular polarization can be obtained by using two coaxial cables with proper angular spacing

such that two orthogonal modes with a proper phase shift are excited. Therefore, the total radiated field by a CP TM_{nm} mode can be considered as the superposition of the individual electric fields produced by the two orthogonal modes and obtained from (13):

$$\begin{aligned} E_{\theta n}^t &= E_{\theta n}^1(\phi, \theta) + jE_{\theta n}^2(\phi + \alpha, \theta) \\ E_{\phi n}^t &= E_{\phi n}^1(\phi, \theta) + jE_{\phi n}^2(\phi + \alpha, \theta) \end{aligned} \quad (14)$$

where superscripts 1 and 2 correspond to the fields generated by the two coaxial cables, respectively, α is the angular spacing of the probes depending on the mode order [20], while the phase shift has been chosen equal to $\pi/2$ in order to obtain a right-handed circular polarized (RHCP) field.

From these expressions, we can derive the x and y components of the total radiated field:

$$\begin{aligned} E_x &= -j^n \frac{e^{-jk_0 r}}{2r} ahk_0 J_n(ak_0 \sqrt{\epsilon_r}) \left[e^{-j(n-1)\phi} J_{n-1}(\gamma) - e^{-j(n+1)\phi} J_{n+1}(\gamma) \right] \text{Cos}[\theta] = \\ &= A e^{-j(n-1)\phi} - B e^{-j(n+1)\phi} \end{aligned} \quad (15)$$

$$\begin{aligned} E_y &= j^{n+1} \frac{e^{-jk_0 r}}{2r} ahk_0 J_n(ak_0 \sqrt{\epsilon_r}) \left[e^{-j(n-1)\phi} J_{n-1}(\gamma) + e^{-j(n+1)\phi} J_{n+1}(\gamma) \right] \text{Cos}[\theta] = \\ &= -j \left[A e^{-j(n-1)\phi} + B e^{-j(n+1)\phi} \right] \end{aligned}$$

where:

$$\begin{aligned} A &= -j^n \frac{e^{-jk_0 r}}{2r} ahk_0 J_n(ak_0 \sqrt{\epsilon_r}) \text{Cos}[\theta] J_{n-1}(\gamma) \\ B &= -j^n \frac{e^{-jk_0 r}}{2r} ahk_0 J_n(ak_0 \sqrt{\epsilon_r}) \text{Cos}[\theta] J_{n+1}(\gamma) \end{aligned} \quad (16)$$

From (15) we note that the x-component (y-component) consists of the difference (the sum) of the same two terms, having phase evolutions of the forms $e^{-j(n-1)\phi}$ and $e^{-j(n+1)\phi}$, respectively.

However, for a patch antenna with typical geometrical and EM parameters, the amplitude of the second term is always significantly smaller than the one of the first term. In fact, the amplitude of the two terms differs only in the order of the Bessel function and, for small values of the argument, the higher the order of the function, the lower its value. This aspect has been also verified through several full-wave simulations, whose results are not reported here for sake of brevity. Moreover, as shown in Fig. 91 for the case of a patch antenna working in the CP TM_{21} mode, increasing the dielectric permittivity of the substrate the first term becomes increasingly dominant. In the case of a circular polarized TM_{nm} mode we can thus consider only the term proportional to $e^{-j(n-1)\varphi}$ that corresponds to an EM field carrying an OAM of order $n-1$.

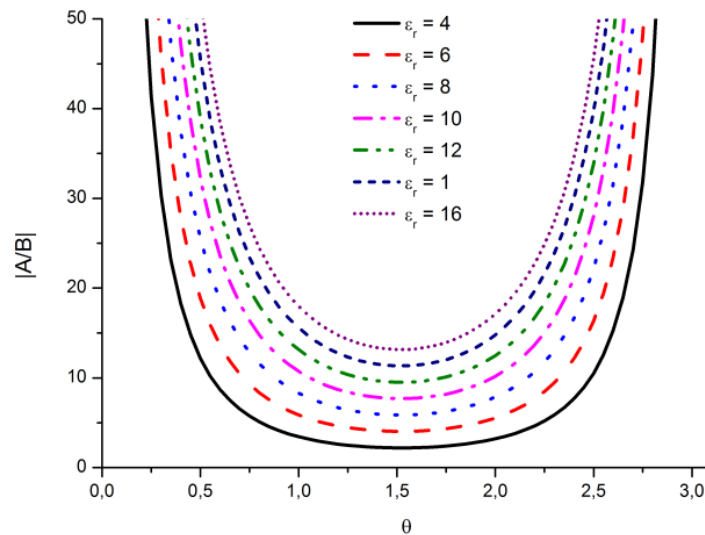


Fig. 91: Ratio between the amplitude of the terms A and B in the case of a circular patch antenna working in a CP TM_{21} mode for different values of substrate permittivity.

Therefore, for the first resonant mode of a circular patch antenna (TM_{11}) the OAM is equal to zero. However, for the higher order modes with $n > 1$, the radiated EM field is characterized by a non-zero OAM. This is confirmed by the phase patterns reported in Fig. 92, where we can observe that the electric fields produced by TM_{21} and TM_{31} modes have the rotating phase front expected by a non-zero OAM [21]. On the contrary, the TM_{11} mode has a phase pattern independent of φ , which corresponds to a zero OAM. Moreover, the conical radiation patterns of a circular patch antenna working at higher order modes [20] are also in agreement with the presence of an EM field with

non-zero OAM, which has, as another peculiar aspect, an amplitude null in the propagation direction.

Finally, note that, reassessing equation (14)-(16) for a $-\pi/2$ phase shift between the two coaxial cables, we obtain a left-handed CP field with a dominant phase term $e^{j(n-1)\phi}$ and, therefore, an OAM state with an opposite sign.

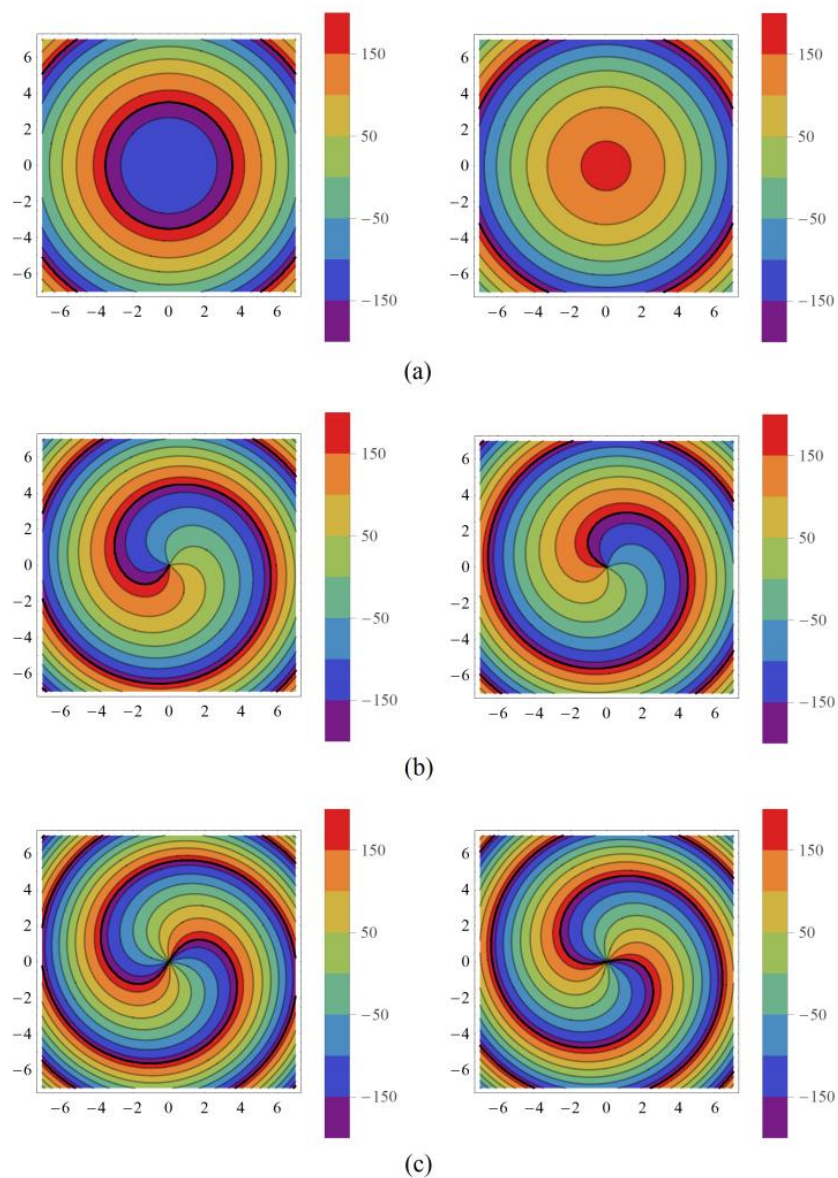


Fig. 92: Phase patterns (in degree) of the x (left) and y (right) component of the radiated electric field in the case of: (a) RHCP TM_{11} mode; (b) RHCP TM_{21} mode; (c) RHCP TM_{31} mode.

5.2 Validation through Full-Wave Numerical Simulations

As analytically shown in the previous Section, the CP TM_{nm} modes of a circular patch antenna radiate an EM field with OAM of order $\pm(n-1)$. Such a structure, even if simpler and more compact than those ones proposed in the literature, can be further simplified. In fact, circular polarization can be obtained also through a single coaxial feed. A possible solution consists of introducing a proper asymmetry in the geometrical structure in such a way that two degenerate modes are excited [22]-[23].

Therefore, in order to obtain a patch antenna with a single feed that generates OAM states, we have transformed the circular patch into an elliptical one, as shown in Fig. 93.

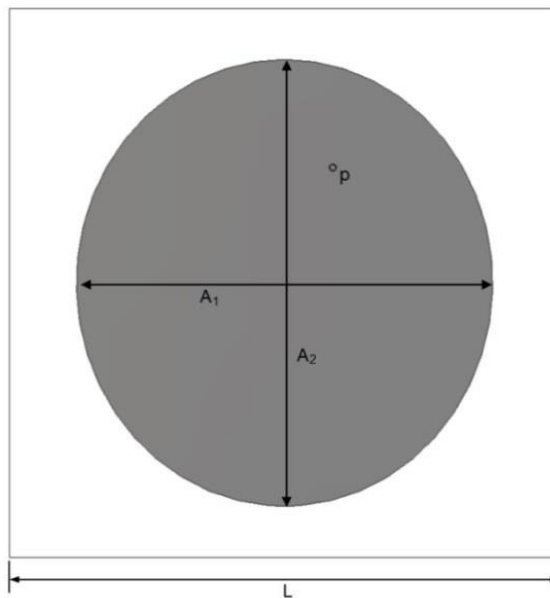


Fig. 93: Top view of the elliptical patch antenna. The inner conductor of the coaxial cable is connected to the point p ($x = 8.75$ mm; $y = 21$ mm). The origin of the reference system is at the shape centre. Antenna dimensions are: $A_1 = 75,2$ mm, $A_2 = 81.6$ mm, and $L = 100$ mm.

The elliptical metallic patch is placed on a square 0.787 mm thick Rogers DuroidTM RT5870 ($\epsilon_r = 2.33$, $\tan\delta = 0.0012$). The dimensions of the two main axes of the elliptical patch have been properly chosen to obtain two almost overlapped resonant frequencies and, therefore, a CP TM_{21} mode around 2.4 GHz. Moreover, the 50 Ω coaxial cable has

been properly positioned to obtain a good impedance matching of the two degenerate modes. The main geometrical dimensions of the structure are reported in Fig 93.

Using the full-wave numerical solver CST Microwave Studio [24], we have simulated the radiating and matching properties of the proposed structure. From Fig. 94 we can see that the proposed antenna is well matched around two slightly different resonant frequencies, as required to generate a circular polarized TM_{21} mode. Furthermore, in order to verify the actual generation of a non-zero OAM, the phase patterns of the x and y components of the radiated electric field are shown in Fig. 95. As readily apparent, these phase patterns have a helical profile with a 2π phase change in one turn, corresponding to a phase term $e^{-j\phi}$. Therefore, the proposed antenna effectively radiates a circular polarized EM field with an OAM of the first order. This result is also confirmed by the simulated phase of radiation patterns, reported in Fig. 96, that show a spiral variation with the azimuthal angle. Finally, please note that the 3-D directivity pattern, reported in Fig. 97, shows an amplitude null in the propagation direction, as expected due to the helical phase profile.

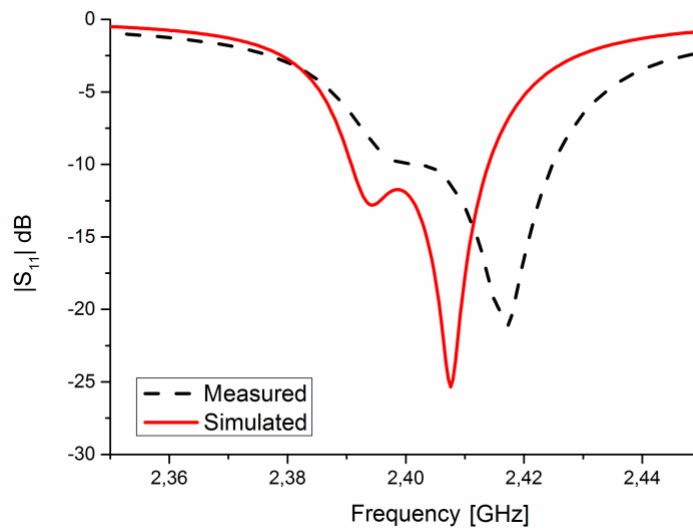


Fig. 94: Simulated (red-solid line) and measured (black-dashed line) reflection coefficient amplitude of the proposed elliptical patch antenna shown in Fig. 93.

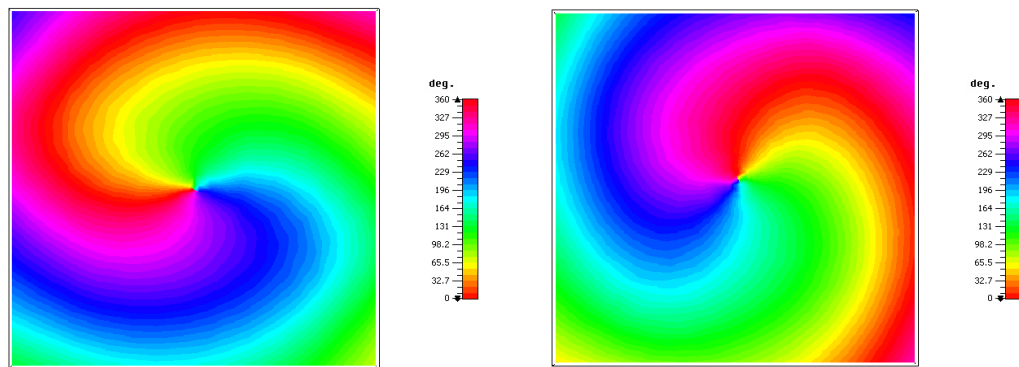


Fig. 95: Phase patterns at 2.4 GHz of the x (left) and y (right) component of the radiated E field by the elliptical patch antenna working in a RHCP TM_{21} mode.

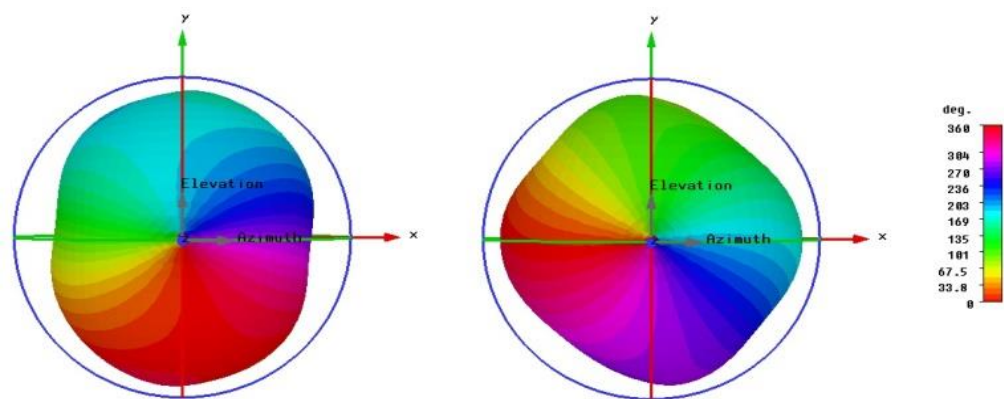


Fig. 96: Simulated Azimuth (left) and Elevation (right) radiation phase patterns at 2.4 GHz of the elliptical patch antenna, shown in Fig. 93, working in a RHCP TM_{21} mode.

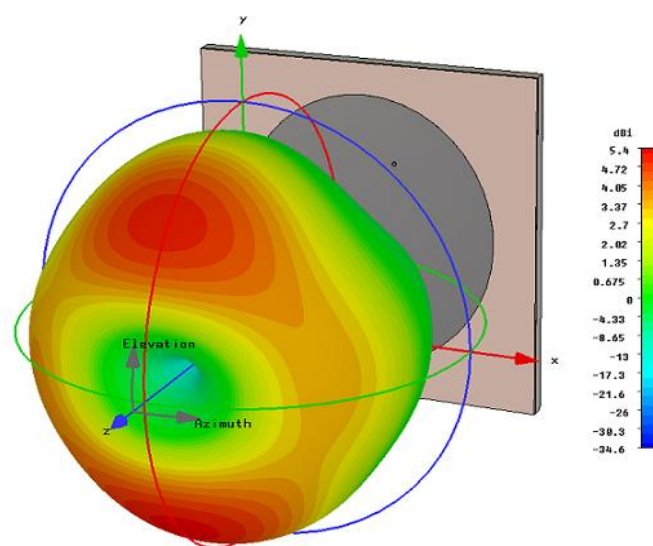


Fig. 97: 3-D directivity pattern at 2.4 GHz of the antenna shown in Fig. 93.

5.3 Experimental Realization and Measurements

The proposed antenna with the dimensions given in Fig. 93 has been manufactured with a LPKF Protomat-S milling machine. An SMA connector with characteristic impedance of 50Ω has been used to feed the prototype antenna (see Fig. 98). Then, the matching and radiating properties have been measured by using a vector network analyzer and a near-field antenna measurement system.

The measured magnitude of the S_{11} parameter, reported in Fig. 94, is in good agreement with the simulated one. In particular, the antenna is well matched around 2.41 GHz and shows two almost overlapped resonant frequencies. The slight shift in frequency between the simulated and measured results, due to manufacturing tolerances, does not affect the antenna operation and the proof of concept we wanted to give. In fact, the far-field phase patterns of the elevation and azimuth components at 2.4 GHz, reported in Fig. 99, show the expected helical profile of the OAM of the first order.

These results, thus, confirm that an elliptical patch antenna, if properly designed, can be used to generate an EM field with non-zero OAM.



Fig. 98: Photograph showing the realized elliptical patch antenna with the dimensions given in Fig. 93.

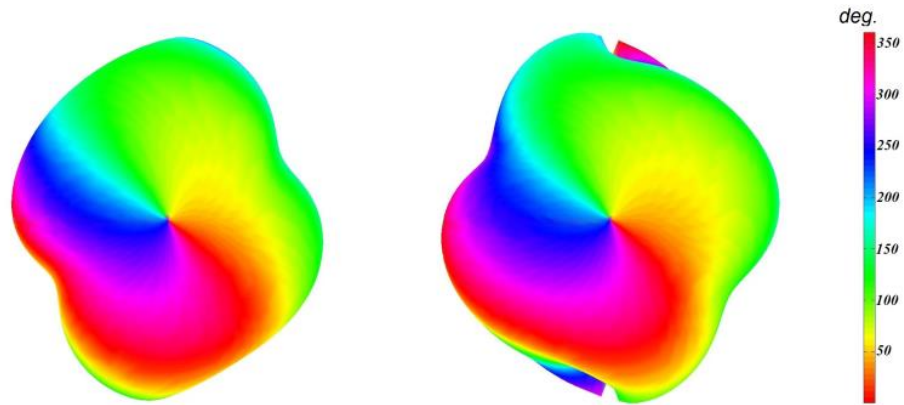


Fig. 99: Measured Azimuth (left) and Elevation (right) radiation phase patterns at 2.4 GHz of the prototype shown in Fig. 98.

5.4 Summary

In this Chapter, we have presented a novel approach to generate an EM field with non-zero OAM at microwave frequencies. At first, we have analytically studied the EM field produced by a circular patch antenna in order to show that a CP TM_{nm} mode generates an OAM of order $\pm(n-1)$. For this purpose, the circular patch antenna can be excited with two properly spaced coaxial cables with the same signal amplitudes but with a $\pm\pi/2$ phase shift.

Then, we have shown that an EM field with non-zero OAM can be also generated with a single coaxial feed by using an elliptical patch antenna. In fact, the geometrical asymmetry of this structure allows generating two orthogonal modes that produce a CP EM field. In particular, we have designed an elliptical patch antenna working in a RHCP TM_{21} mode. By using CST Microwave Studio, we have numerically demonstrated that this structure radiates a RHCP EM field with an OAM of the first order around 2.4 GHz.

Finally, we have realized and tested a prototype of the proposed elliptical patch antenna and the measured results validate the predicted characteristics. The final message is that a standard patch antenna, if properly designed, can be employed to generate OAM states. Compared to the other solutions already proposed in the

literature, based on either antenna arrays or complex reflector antennas, the proposed one is cheaper, lighter, and more compact.

5.5 References

- [1] M. Padgett, and L. Allen, "Light with a twist in its tail," *Contemp. Phys.*, vol. 41, pp. 275-285, 2000.
- [2] J. P. Torres, and L. Torner, *Twisted Photons: Applications of Light with Orbital Angular Momentum*. Wiley-VCH, 2011.
- [3] A. M. Yao and M. J. Padgett, "Orbital angular momentum: origins, behavior and applications," *Adv. Opt. Photon.*, vol. 3, pp. 161–204, 2011.
- [4] Y.S. Jiang, Y.T. He, and F. Li, "Electromagnetic Orbital Angular Momentum in Remote Sensing," *PIERS Proceedings, Moscow, Russia, August 18-21, 2009*.
- [5] B. Thidé, H. Then, J. Sjöholm, K. Palmer, J. Bergman, T.D. Carozzi, Y. N. Istomin, N. H. Ibragimov, and R. Khamitova, "Utilization of photon orbital angular momentum in the low-frequency radio domain," *Phys. Rev. Lett.*, vol. 99, no. 8, pp. 087701-1–087701-4, Aug. 2007.
- [6] S. M. Mohammadi, L. K. S. Daldorff, J. E. S. Bergman, R. L. Karlsson, B. Thide, K. Forozesh, T. D. Carozzi, and B. Isham, "Orbital angular momentum in radio—a system study," *IEEE Trans. Antennas Propag.*, vol. 58, pp. 565–572, 2010.
- [7] A. Tennant, and B. Allen, "Generation of OAM radio waves using circular time-switched array antenna," *Electron. Lett.*, vol. 48, pp. 1365–1366, 2012.
- [8] F. Tamburini, E. Mari, B. Thidé, C. Barbieri, and F. Romanato, "Experimental verification of photon angular momentum and vorticity with radio techniques," *Appl. Phys. Lett.*, vol. 99, pp. 204102-1-204102-3, 2011.
- [9] F. Tamburini, E. Mari, A. Sponselli, F. Romanato, B. Thidé, A. Bianchini, L. Palmieri, and C. G. Someda, "Encoding many channels in the same frequency through radio vorticity: first experimental test," *New J. Phys.*, vol. 14, pp. 033001, 2012.
- [10] M. Harris, C. A. Hill and J. M. Vaughan, "Optical Helices and Spiral Interference Fringes," *Optics Comm.*, vol. 106, pp. 161-166, 1994.
- [11] M.W. Beijersbergen, R.P.C. Coerwinkel, M. Kristensen, and J.P. Woerdman, "Helical-Wavefront Laser Beams Produced with a Spiral Phaseplate," *Optics. Comm.*, vol. 112, pp. 321-327, 1994.
- [12] O. Edfos, and A.J. Johansson, "Is orbital angular momentum (OAM) based radio communication an unexploited area?," *IEEE Trans. Antennas Propag.*, vol. 60, pp. 1126–1131, 2012.
- [13] N. Uribe-Patarroyo, A. Fraine, D. Simon, O. Minaeva and A. Sergienko, "Object Identification Using Correlated Orbital Angular Momentum (OAM) States," in *Frontiers in Optics, Rochester, NY, USA, 2012*.

- [14] D. M. Pozar, "Microstrip antennas," *Proc. IEEE*, vol. 80, pp. 79-91, 1992.
- [15] Y.J. Wang, and C.K. Lee, "Compact and broadband microstrip patch antenna for the 3G IMT-2000 handsets applying styrofoam and shorting-posts," *Progress in Electromagnetics Research*, vol. 47, pp. 75-85, 2004.
- [16] F. Bilotti, and C. Vegni, "Design of polygonal patch antennas for portable devices," *Progress in Electromagnetics Research*, vol. 24, pp. 33-47, 2010.
- [17] M.T. Islam, M.N. Shakib, and N. Misran, "Broadband E-H shaped microstrip patch antenna for wireless systems," *Progress in Electromagnetics Research*, vol. 98, pp. 163-173, 2009.
- [18] M. Barbuto, F. Bilotti, and A. Toscano, "Design of a multifunctional SRR-loaded printed monopole antenna," *Int. J. RF Microw. CAE*, vol. 22, pp. 552-557, 2012.
- [19] A.G. Derneryd, "Analysis of the microstrip disk antenna element," *IEEE Trans. Antennas Propagat.*, vol. 27, pp. 660-664, 1979.
- [20] J. Huang, "Circularly polarized conical patterns from circular microstrip antennas," *IEEE Trans. Antennas Propagat.*, vol. 32, pp. 991-994, 1984.
- [21] J. Courtial, D. A. Robertson, K. Dholakia, L. Allen, and M. J. Padgett, "Rotational frequency shift of a light beam," *Phys. Rev. Lett.*, vol. 81, pp. 4828-4830, 1998.
- [22] Y.T. Lo, and W.F. Richards, "Perturbation approach to design of circularly polarized microstrip antennas," *Electron. Lett.*, vol. 17, pp. 383-385, 1981.
- [23] B. Du, and E. Yung, "A single-feed TM₂₁-mode circular patch antenna with circular polarization," *Microw. Opt. Technol. Lett.*, vol. 33, pp. 154-156, 2002.
- [24] CST Studio Suite 2012, CST Computer Simulation Technology AG, Available at: www.cst.com.

Publications

Journal Publications

1. M. Barbuto, F. Trotta, F. Bilotti, and A. Toscano, "Horn antennas with integrated notch filters," *IEEE Transactions on Antennas and Propagation*, Vol. 63, No. 2, pp. 781-785, 2015.
2. M. Barbuto, F. Trotta, F. Bilotti, and A. Toscano, "Circular polarized patch antenna generating orbital angular momentum," *Progress In Electromagnetics Research*, Vol. 148, 23-30, 2014.
3. M. Barbuto, F. Bilotti, and A. Toscano, "Novel waveguide components based on complementary electrically small resonators," *Photonics and Nanostructures – Fundamentals and Applications*, Vol. 12, No. 4, pp. 284-290, 2014.
4. M. Barbuto, F. Trotta, F. Bilotti, and A. Toscano, "A combined bandpass filter and polarization transformer for horn antennas," *IEEE Antennas and Wireless Propagation Letters*, Vol. 12, pp. 1065-1067, 2013.
5. M. Barbuto, A. Alù, F. Bilotti, A. Toscano, and L. Vegni, "Characteristic impedance of a microstrip line with a dielectric overlay," *COMPEL - The International Journal for Computation and Mathematics in Electrical and Electronic Engineering*, Vol. 32, No. 6, pp. 1855-1867, 2013.
6. M. Barbuto, A. Monti, F. Bilotti, and A. Toscano, "Design of a non-Foster actively loaded SRR and application in metamaterial-inspired components," *IEEE Transactions on Antennas and Propagation*, Vol. 61, No. 3, pp. 1219-1227, 2013.
7. M. Barbuto, F. Bilotti, and A. Toscano, "Design of a multi-functional SRR-loaded printed monopole antenna," *International Journal of RF and Microwave Computer-Aided Engineering*, Vol. 22, No. 4, pp. 552-557, July 2012.

Conference Papers

1. M. Barbuto, F. Bilotti, and A. Toscano, "Power-Selectivity Horn Filtenna Loaded with a Nonlinear SRR," *Metamaterials '2015: The Ninth International Congress on Advanced Electromagnetic Materials in Microwaves and Optics*, 7 - 12 September, 2015, Oxford, UK.
2. D. Ramaccia, A. Verrengia, F. Bilotti, A. Toscano, A. Monti, M. Barbuto, F. Trotta, D. Muha, and S. Hrabar, "Experimental verification of broadband antennas loaded with metamaterials," *Proc. of the 2015 IEEE International Symposium on Antennas and Propagation and USNC/URSI National Radio Science Meeting*, Vancouver, BC, Canada, 19-25 July, 2015.
3. D. Ramaccia, F. Bilotti, A. Toscano, and M. Barbuto, "Complete transmission through short waveguide bends using connected bi-omega particles," *Proc. of the 2015 IEEE International Symposium on Antennas and Propagation and USNC/URSI National Radio Science Meeting*, Vancouver, BC, Canada, 19-25 July, 2015.
4. D. Ramaccia, F. Bilotti, A. Toscano, M. Barbuto, D.L. Sounas, and A. Alù, "Reciprocal and non-reciprocal signal manipulation through horn antennas loaded with metamaterial-inspired particles," *Proc. of the 2015 IEEE International Symposium on Antennas and Propagation and USNC/URSI National Radio Science Meeting*, Vancouver, BC, Canada, 19-25 July, 2015.
5. A. Monti, M. Barbuto, D. Ramaccia, F. Bilotti, and A. Toscano, "Broadband enhanced transmission through a single aperture based on actively loaded SRR," *ICNAAM 2014: 12th International Conference of Numerical Analysis and Applied Mathematics*, 21-27 September 2014, Rhodes, Greece.
6. M. Barbuto, A. Monti, D. Ramaccia, F. Bilotti, and A. Toscano, "Design and realization of MTM-inspired absorbers using graphite resistive sheets," *ICNAAM 2014: 12th International Conference of Numerical Analysis and Applied Mathematics*, 21-27 September 2014, Rhodes, Greece.
7. M. Barbuto, F. Bilotti, A. Monti, D. Ramaccia, and A. Toscano, "Use of metamaterials to improve electrical and radiating performances of horn antennas," *XX Riunione Nazionale di Elettromagnetismo Applicato*, CD Digest, pp. XX-XX, Padova, 15-18 Settembre 2014.

8. M. Barbuto, F. Bilotti, and A. Toscano, "SRR-based notch filter for horn antennas," *Metamaterials '2014: The Eighth International Congress on Advanced Electromagnetic Materials in Microwaves and Optics*, 25 - 28 August, 2014, Copenhagen, Denmark.
9. F. Fortuna, G. Bella, M. Barbuto, R. Conti, R. Cozzolino, S. Di Francesco, A. Donno, V. Duraccio, O. Giannini, V. Montesarchio, A. Monti, L. Tribioli, and F. Trovalusci, "Virtual Academic Teaching for Next Generation Engineers," *ASME 2014: 12th Biennial Conference on Engineering Systems Design and Analysis*, Copenhagen, Denmark, July 25–27, 2014.
10. D. Ramaccia, M. Barbuto, A. Monti, F. Bilotti, and A. Toscano, "Horn nano-antenna: efficient wideband radiator at near-infrared and optical frequencies," *Plasmonica 2014: workshop nazionale di plasmonica e applicazioni*, Roma, 30 giugno – 2 luglio, 2014.
11. A. Monti, M. Barbuto, D. Ramaccia, A. Toscano, and F. Bilotti, "Use of plasmonic nanoparticles to achieve mantle cloaking at optical frequencies," *Plasmonica 2014: workshop nazionale di plasmonica e applicazioni*, Roma, 30 giugno – 2 luglio, 2014.
12. M. Barbuto, D. Ramaccia, F. Trotta, A. Toscano, and F. Bilotti, "Conical horn antennas with enhanced functionalities through the use of metamaterial concepts," *Proc. of the 2014 European Conference on Antennas and Propagation (EuCAP 2014)*, The Hague, The Netherlands, 6-11 April 2014, (invited paper).
13. M. Barbuto, F. Bilotti, and A. Toscano, "Design of a circular polarized horn antenna using complementary electrically small resonators," *Metamaterials '2013: The Seventh International Congress on Advanced Electromagnetic Materials in Microwaves and Optics*, 16 - 21 September, 2013, Bordeaux, France.
14. M. Barbuto, A. Toscano, and F. Bilotti, "Single patch antenna generating electromagnetic field with orbital angular momentum," *Proc. of the 2013 IEEE International Symposium on Antennas and Propagation and USNC/URSI National Radio Science Meeting*, Orlando, FL, USA, 7-13 July, 2013.
15. F. Bilotti, M. Barbuto, L. Di Palma, D. Ramaccia, A. Toscano, and L. Vegni, "Linear and circular polarized electrically small antennas based on the employment of metamaterial-inspired sub-wavelength resonators," *Proc. of the*

- 2013 European Conference on Antennas and Propagation (EuCAP 2013), pp. 3010-3011, Gothenburg, Sweden, 8-14 April 2013 (invited paper).
16. M. Barbuto, and A. Toscano, "Linear-to-circular polarization transformer based on the employment of electrically small antennas," *Metamaterials '2012: The Sixth International Congress on Advanced Electromagnetic Materials in Microwaves and Optics*, 17 - 22 September, 2012, St. Petersburg, Russia.
 17. M. Barbuto, A. Monti, D. Ramaccia, F. Bilotti, A. Toscano, and L. Vegni, "Metamaterial activities at microwave and optical frequencies at "Roma Tre" University," *XIX Riunione Nazionale di Elettromagnetismo Applicato*, CD Digest, pp. 657-660, Roma, 10-14 Settembre 2012.
 18. M. Barbuto, A. Monti, F. Bilotti, and A. Toscano, "Design of a non-Foster actively loaded metamaterial-inspired antenna," *Proc. of the 2012 IEEE International Symposium on Antennas and Propagation and USNC/URSI National Radio Science Meeting*, Chicago, IL, USA, 8-14 July, 2012.
 19. M. Barbuto, F. Bilotti, and A. Toscano, "Linear-to-circular polarization transformer using electrically small antennas," *Proc. of the 2012 IEEE International Symposium on Antennas and Propagation and USNC/URSI National Radio Science Meeting*, Chicago, IL, USA, 8-14 July, 2012.
 20. D. Ramaccia, A. Monti, M. Barbuto, F. Bilotti, and A. Toscano, "Realizzazione e caratterizzazione di fogli resistivi a base di grafite," *Convegno su Campi elettromagnetici e innovazione tecnologica in ambito Difesa, Industria e Ricerca*, C.I.S.A.M., Pisa, Italia, 30-31 Maggio 2012.
 21. M. Barbuto, A. Monti, F. Bilotti, and A. Toscano, "Employment of non-Foster active loads to improve the operation bandwidth of SRR loaded monopole antennas," *2012 IEEE International Workshop on Antenna Technology: Small Antennas and Unconventional Applications*, 5 - 7 March, 2012, Tucson, Arizona, USA.
 22. M. Barbuto, A. Monti, F. Bilotti, and A. Toscano, "Some applications of MTMs based on non-Foster active loads," *Proceedings of the Fifth International Congress on Advanced Electromagnetic Materials in Microwaves and Optics – Metamaterials 2011*, Barcelona, Spain, 10 – 15 October, 2011.

Biographical Note

April 26, 1986	Born, Rome, Italy
October 08, 2008	B.S. Electronic Engineering
October 25, 2010	M.S. ICT Engineering
September, 2011	Aptitude to the profession of Engineer
January 2011 – December 2014	PhD Student in Applied Electromagnetics



Mirko Barbuto (S'12) was born in Rome, Italy, on April 26, 1986. He received both the B.S. degree and M.S. degree (*summa cum laude*) in electronic and ICT engineering from “Roma Tre” University, Rome, Italy, in 2008 and 2010 respectively. In 2011, he started his PhD research program at the Department of Applied Electronics of “Roma Tre” University under supervision of Prof.

Alessandro Toscano. Since September 2013 he is an Assistant Professor (3-year position) at “Niccolò Cusano” University, Rome, Italy. His current research interests include metamaterial applications to microwave components and radiating elements, broadband metamaterials based on non-Foster circuits, miniaturized and multifunctional antennas, radiating elements generating EM field with orbital angular momentum and power-depending MTM-inspired devices. He served as a staff or committee member for several national and international scientific conferences and doctoral schools and as a Technical Reviewer of the major international journals related to electromagnetic field theory and metamaterials such as *IEEE Transaction on Antennas and Propagations*, *IEEE Antennas and Wireless Propagation Letters* and *Journal of Applied Physics*.

Dr. Barbuto is currently member of the Italian Society on Electromagnetics (SIEM), of the National Inter-University Consortium for Telecommunications (CNIT) of the Virtual Institute for Artificial Electromagnetic Materials and Metamaterials (Metamorphose VI AISBL), and of the Institute of Electrical and Electronics Engineers (IEEE). Currently, he is the author of about 30 papers in international journals and conference proceedings.